From Stress Corrosion to Catastrophic Fracture Mechanisms in Molecular Dynamics Models of Brittle Materials

Peralta, Giovanni

Awarding institution:
King's College London

FROM STRESS CORROSION TO CATASTROPHIC FRACTURE MECHANISMS IN MOLECULAR DYNAMICS MODELS OF BRITTLE MATERIALS

Giovanni Peralta

Department of Physics

King's College London

A thesis submitted for the degree of

DOCTOR OF PHILOSOPHY

January 2014

To my mother and my father

Acknowledgements

I would like to thank my supervisor Prof. Alessandro De Vita for providing me with the opportunity to work in the "Fracture Team", for teaching me to challenge the research experience with courage, awareness and hard work. I have been privileged to work with Dr James Kermode, who has been an amazing guide, dispensing priceless knowledge, enthusiasm for research and constant encouragement during the whole process of my PhD. I am also thankful to Dr Silvia Cereda, for having followed my first steps of this research work, to Dr. Alessio Comisso for the precious IT assistance and to my second supervisor Prof. Lev Kantorovich for being an inspirational teacher. I acknowledge the financial support received by the European Commission under the EU-FP7-NMP grant 229205 ADGLASS.

I have been fortunate to meet very special people at the Physics Department of King's College London, with whom I shared the passion for physics as well as unforgettable moments. I thank all my colleagues and friends happy to share lunch time and coffee breaks seasoned with bizarre discussions about the meaning of life. I am particularly thankful to Julia Kilpatrick and Paul Le Long for being amazing guides of the Physics Department, Nicholas Houston for patiently proof reading this thesis and my pub companion Spyros for the phylosophical beer sessions at "The Lamb".

My life experience in London would not have been so special if I had not lived at Goodenough College. I would like to thank all the amazing people I had the fortune to meet there, especially those that constantly encouraged and supported me in many ways: I remember particularly Amaka, Nedu, Fernando, Cecilia, Esteban, Katharina, John, Roberto, Raquel, Fr. Brian, Jennie, Arnaud, Patricia, Ghazal, Bonnie, Akbar.

Finally, I would like to thank my families (the Sardinian and the Polish one) for their support, Prof. Vincenzo Fiorentini for encouraging me to start a PhD abroad, and Martyna, who changed my life with unconditional love.

Abstract

Fracture propagation in brittle materials has been studied using hybrid molecular dynamics simulations, allowing the use of quantum calculations wherever and whenever needed by the problem under investigation. Several timescales of the fracture process have been taken into consideration, going from the lowest possible velocity for a crack growing in subcritical loading conditions, to the highest velocity computed for very cold cracks. The study has been carried out in two prototypical models of brittle fracture: silicon and amorphous silica. Aiming to interpret the lowest crack velocity ever measured by experiments on silicon at room conditions, we used quantum-accurate computer simulations to show that immediate dissociation of oxygen molecules, and consequent oxidation of the highly stressed silicon crack tips, may be the cause of the observed slow crack growth. This theoretical prediction, supported by experimental evidence, clarifies long-standing discrepancies concerning the role of oxygen as a stress corrosion agent in silicon. Turning the attention to fast crack behaviour, a crossover between activated and catastrophic branches of crack velocities as a function of temperature has been detected in a hybrid classical molecular dynamics model of silicon. Cold cracks travel faster for high loading energies, while this trend is reversed in the region of energies where activated processes become dominant. Finally, the study of catastrophic fracture in amorphous silica has been initiated, testing for the first time our hybrid approach to non crystalline structures.

Preface

This thesis describes work carried out between March 2010 and January 2014 at the Physics Department of King's College London, under the supervision of Prof. Alessandro De Vita, Dr James Kermode and Prof. Lev Kantorovich. During the course of my PhD I have contributed to the following publications:

- Anna Gleizer, Giovanni Peralta, James R Kermode, Alessandro De Vita and Dov Sherman. Dissociative chemisorption of O_2 induces stress corrosion cracking in silicon crystals. Published on Physical Review Letters. Presented in Chapter 3.
- James R Kermode, Giovanni Peralta, Zhenwei Li and Alessandro De Vita. Multiscale modelling of materials chemomechanics: brittle fracture of oxides and semiconductors. Published on Procedia Materials Science. Presented in Chapter 2.
- Giovanni Peralta, James R Kermode, Silvia Cereda, Zhenwei Li, Albert Bartók, Gabor Csányi, Alessandro De Vita. Inversion in crack speed as a function of temperature during crossover from activated to catastrophic fracture. In preparation. Presented in Chapter 4.
- Giovanni Peralta, James R Kermode, Silvia Cereda and Alessandro De Vita. Molecular dynamics investigation of brittle fracture mechanisms in amorphous silica. In preparation. Presented in Chapter 5.

Materials from these papers appear in this dissertation. This dissertation is my own work and it presents results achieved in strict collaboration with Cambridge University and the Technion Institute, Haifa. It has not been submitted in whole or in part for any degree or diploma at this or any other university.

Giovanni Peralta

Contents

List of Figures

Nomenclature

Roman Symbols

$\hat{C}$	Tensor of the elastic constants
G	Energy release rate
$\hat{J} = \{J_{ij}, i, j = 1, 2, 3\}$	Jacobian matrix of the displacement field
K	Stress intensity factor
K_c	Fracture toughness
B	Bulk modulus
E	Young's modulus
$\hat{T}$	Stress tensor
$\vec{u}(\vec{x})$	Vectorial displacement field

Greek Symbols

$\Delta = G/G_c$	Loading in reduced units
β	Viscous damping coefficient for the Langevin equation
ΔE	Energy difference
Δt	Bond breaking time interval
Δx	Bond breaking average advancement
$\hat{\epsilon}$	Strain tensor
Γ	Fracture energy

γ Relaxed surface energy

λ First Lamé coefficient

μ Shear modulus

ν Poisson's ratio

σ Hydrostatic pressure, load, applied stress

Acronyms

BKS Beest Kramer Santen

DFT Density Functional Theory

FIRE Fast Inertial Relaxation Engine

GAP Gaussian Approximation Potential

GGA Generalized Gradient Approximation

LDA Local Density Approximation

NPT Number, Pressure, Temperature

NVE Number, Volume, Energy

NVT Number, Volume, Temperature

LEFM Linear Elastic Fracture Mechanics

MD Molecular Dynamics

LJ Lennard-Jones

LOTF Learn On The Fly

PES Potential Energy Surface

QM/MM Quantum Mechanics/Molecular Mechanics

SCC Stress Corrosion Cracking

SW Stillinger-Weber

TS Tangney-Scandolo

Chapter 1

Introduction

The human endeavour to transform nature has characterised the history of mankind from many perspectives. The action of shaping and transforming objects, aiming to improve their living condition, represents a peculiarity of human evolution. In this process, making and breaking are two sides of the same coin. Every technological advance relies upon both making something from raw materials, and preserving them against failure. For this reason the act of making would be meaningless without a clear knowledge of how things break.

Despite the relevance of the problem, a theoretical understanding of material failure mechanisms was started only around hundred years ago. Since then, the unavoidable presence of defects and micro cracks within the material body was identified as the main cause of a material's weakness to external loads. However, the broad range and diverse features in which solid bodies could fail were totally unpredictable and yet unexplained. Fracture mechanics originated in this scenario, aiming to solve the origin of material failure and to theoretically predict fracture mechanisms.

In empirical terms, fracture represents the irreversible failure of a material into several pieces. The physical causes that lead a material to experience this dramatic phenomenon can be seen from different perspectives. At the macroscopic level, a basic study of the elasticity of the material gives a satisfactory description of the fracture process as the result of a local stress singularity in the proximity of the crack tip. Looking at the atomic scale, fracture can be seen as a succession of bond breaking events. The coupling between the nanoscopic origin and the macroscopic response of fracture is the key which opens the gate of a multi-scale approach to studying the mechanical behaviour of materials.

Starting from these considerations, research carried out in this PhD project has

focused on modelling brittle fracture in crystalline silicon and amorphous silica. Silicon (Si), extracted from silicates (silica, or silicon dioxide, both in crystalline and amorphous forms) is the second most abundant element on Earth after oxygen. Amorphous silica (a-SiO_2) is the disordered structure of crystalline silica (SiO_2): it is the main constituent of the most common type of glass.

Fracture problems in silicon and silicates have a huge technological and scientific relevance, spanning over a range of human activities including mining (rock crushing and grinding), civil engineering (fracture of structural glasses), biomedicine (prosthetic implants), and semiconductor technology. The challenges offered by the exponential increase of high-tech materials has required a continuous improvement of theoretical methods able to predict fracture mechanisms down to the atomic scale. This need has been addressed recently by the increasing power of supercomputers, with the advent of computer modelling of matter at the atomic level.

This thesis represents an attempt to describe the chronology of a model crack by means of molecular dynamics simulations in two prototypical systems of brittle fracture: Si and a-SiO_2. In this journey, several phases of the crack life have been taken into consideration, spanning from the lowest crack speed measurable at initiation to a catastrophic fracture dynamics. To investigate these diverse features of brittle fracture, a hybrid approach mixing classical and quantum mechanics has been applied only wherever and whenever needed by the problem under consideration.

In Chapter 2 we review the fundamental notions of fracture mechanics, starting from a brief historical background of previous studies, and then focusing on the fundamental physics of elasticity applied to fracture problems. The passage between the continuum and discrete views of matter is analysed, introducing the reader to atomistic fracture studies. Then, we introduce the computational methods used to study fracture: molecular dynamics, quantum mechanics and the hybrid technique used to match these differing approaches. Finally, we explore selected examples of experimental techniques used to study fracture problems at the nanoscale, highlighting the link with computational simulations.

Inspired by recent experimental observations, suggesting the occurrence of stress corrosion cracking in silicon for the first time, we present in Chapter 3 results of a multi-scale hybrid simulation of this experimental setting. A theoretical background on previous stress corrosion studies in glass and silicon introduces our research towards a nanoscale analysis. By means of computer simulations at the quantum mechanical level, we aim to offer a clear picture of chemical reactions that may occur at the silicon crack tip when exposed to an air environment. The experiments performed by

our collaborators are also reported, concluding with a discussion and analysis of both experimental and theoretical investigations.

From subcritical crack growth, typical of stress corrosion conditions, we turn our attention to super-fast cracks that cleave atomic bonds at a significant fraction of the speed of sound. Chapter 4 presents a computational analysis of fracture speed in silicon as a function of environment temperature and applied load. Our research, building on previous fracture studies on silicon, aims to investigate crack dynamics by means of a hybrid molecular dynamics simulation. The hybrid approach used in this case consists of mixing two classical interatomic potentials: one, based on DFT data, for describing a few atoms around the crack tip; the other one, less general but computationally more efficient, to describe the long-range stress field.

The motivation of improving atomic-scale knowledge of structural glassy materials, aiming to enhance resistance to fracture, led us to start a theoretical investigation of catastrophic crack propagation in amorphous silica systems. Chapter 5 reports our contribution to the ADGLASS[1] (Adhesion and cohesion at interfaces in high performance glassy systems), a large research project merging academy and industry and funded by the European Union. Our research focused on modelling catastrophic fracture propagation in amorphous silica.

[1] www.adglass.eu

Chapter 2

Fracture at the atomic level: from theory to experiment

2.1 Introduction

Fracture problems have been studied for decades by the engineering community. From a macroscopic point of view, fracture can be interpreted as the structural failure of a material into two or more pieces. Understanding and analysing crack behaviour in solid state systems has been largely performed within the fracture mechanics framework, an important branch of science based on a continuum view of matter. However, the biggest technological leaps are possible if we possess the fundamental knowledge which lies behind empirical observations and macroscopic models. At the fundamental level, fracture is the irreversible process of breaking atomic bonds, due to a local concentration of mechanical stress in a specific region of the material. Despite the effort to look at the fracture problem with an atomic lens, this microscopic definition intrinsically embodies several length scales, from the macroscopic concept of mechanical stress to the microscopic event of breaking an atomic bond.

A crack, or fracture, is a spatial discontinuity in the material's bulk appearing as a void region bounded by newly created surfaces. The existence of this region within the material locally modifies its mechanical properties. If a remote stress is applied to the material, all atomic bonds strain accordingly. However, the presence of a crack plays the crucial role of stress concentrator, enhancing dramatically the strain of the atomic bonds located near the crack tip. This may lead the fracture to advance, releasing the elastic energy with the formation of two new surfaces.

We introduce the basic concepts of Fracture Mechanics in Sec. 2.2, firstly giving

a historical background on fracture studies and explaining the industrial relevance of studying fracture. Then, we review the basic framework of the classical theory of elasticity, looking at the physics of elastic bodies and the definition of the main physical quantities of stress, strain, elastic constants and energy release rate. The first analytical atomistic studies of fracture, precursors of early computer simulations at the atomic level, are outlined in Sec. 2.3. The computational techniques used to approach fracture problems at the atomic scale are presented in Sec. 2.4, giving a detailed description of the classical interatomic potentials and of the Density Functional Theory (DFT) computational engines. Quantum Mechanics Molecular Mechanics (QM/MM) embedding schemes are treated in Sec. 2.5, narrowing the view to the "Learn On The Fly" (LOTF) technique used in this work. Finally, we conclude the theoretical background on fracture in Sec. 2.6 by reviewing selected experimental techniques linked with computer simulations at the nanoscale.

2.2 Fracture Mechanics

Historically, the presence of a surface crack was commonly known to be very helpful in breaking materials. Splitting wood, breaking rocks, cleaving gems are just a few examples of applications of this empirical knowledge. Depending on the way samples break and on the features of the newly created surfaces after the crack propagation, materials can be classified in two distinct categories: brittle and ductile. Brittle materials break suddenly when pulled apart in the perpendicular direction of a preexistent crack, leaving flat surfaces behind the crack path. On the other hand, ductile materials offer greater resistance to fracture propagation, experiencing irreversible plastic deformation of the material's bulk before the failure.

For centuries there has not been an apparent need to master this subject from a theoretical point of view. The industrial revolution represented in this sense a crucial gateway towards a thorough analysis of the mechanical properties of materials, particularly in predicting unprecedented catastrophic failures such as railway accidents, bridges failure and tank explosions (see Ref. [1] for an exhaustive commentary on the historical origin of fracture mechanics). At the beginning of 20th century, the engineering community started a pioneering study on the theoretical causes of brittle fracture. Inglis first in 1913, and then Griffith in 1921, opened the way to a methodological approach which will be, in the years to come, the basis of a new branch of science: fracture mechanics.

Twenty years after Griffith's analysis of brittle fracture, no significant progress was

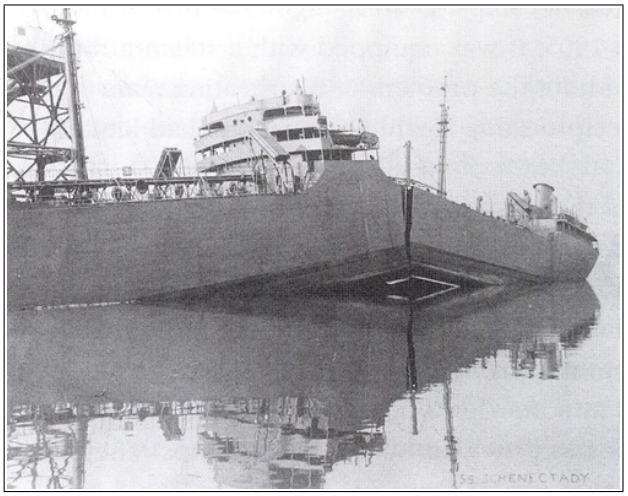

Figure 2.1: Photograph of a Liberty ship that failed at pier in 1943. Reproduced from Ref. [2].

recorded on this matter. The harshness of two world wars presented other urgent priorities that partially set aside an academic approach to fracture. In this scenario, several structural failures were recorded in a series of systematic accidents involving ships and airplanes during the Second World War. An interesting case of study was represented by the construction of a several thousand "Liberty" ships in United States as a response to the Japanese threat in the Pacific Ocean. A significant proportion of these ships experienced catastrophic brittle fracture, breaking in half without warning (see Fig. 2.1).

Subsequent research conducted on these cases identified notch brittleness, resulting from a brittle-ductile transition, as one of the major causes of these calamities. The large scale of these occurrences drove the scientific community to deepen research into the fundamental causes of brittle fracture. In 1950s, Irwin resumed Griffith's work and linked the theoretical prediction of fracture based on the linear elasticity framework with practical quantities measurable in fracture tests. Since then, fracture mechanics has been a solid guide in approaching fracture problems, becoming a recognised branch of science.

A complete overview of fracture mechanics can be found in Ref. [3, 4]. Before retracing the main steps of the pioneers of this science, we step back shortly to the fundamental principles of elasticity theory on which fracture mechanics is based.

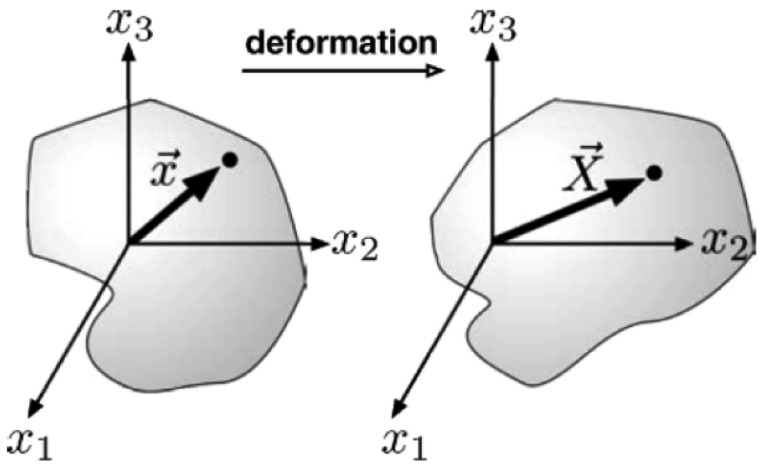

Figure 2.2: Schematic representation of deformation in a solid body. Reproduced from Ref. [5].

2.2.1 Elasticity theory

The main feature characterising the theory of elasticity is the approximation of continuum media, where the real atomic structure is substituted by a continuum distribution of mass. This macroscopic approach can be considered accurate on length scales much greater than the interatomic distance. After introducing the fundamental concepts of strain and stress, this section will focus on the properties of linear elastic materials, in particular isostropic media as they are the most common and easily studied.

2.2.1.1 The concept of strain

The deformation of a rigid body can be seen as a consequence of the applied forces on it, and in linear elasticity theory they are described by the concepts of strain and stress. A solid body is said to exhibit a deformation when it experiences a relative displacement of some points in the body. Obviously, a solid body does not exhibit strain if it experiences only a rigid motion(all its constitutive points are simply translated in space) or a pure rotation (all its constitutive point are rotated but not changed in shape and size).

Let $\vec{x}$ be the position vector of a volume element within a body in its undeformed configuration, and let $\vec{X}$ be the position vector of the same volume element in the respective deformed configuration (see Fig. 2.2). The concept of deformation can be

defined by the following equation:

$$\vec{X} = \vec{x} + \vec{u}(\vec{x}) \tag{2.1}$$

where $\vec{u}(\vec{x})$ represents a vectorial displacement field. All the information relative to the deformation is therefore enclosed in the function $\vec{u}(\vec{x})$.

By calculating the displacement gradient we obtain a mapping of the variation of the displacement field:

$$J_{ij} = \frac{\partial u_i}{\partial x_j} \tag{2.2}$$

with $\hat{J} = \{J_{ij}, i, j = 1, 2, 3\}$ representing the Jacobian matrix of the displacement field.

Linear elasticity is based on the approximation of small deformations. This fundamental assumption can be formalised by imposing as definition of small deformation the following relation:

$$Tr(\hat{J}\hat{J}^T) \ll 1 \tag{2.3}$$

namely a deformation is regarded as small provided that the trace of the product $\hat{J}\hat{J}^T$ is negligible.

The Jacobian matrix of the displacement field can be written as the sum of a symmetric and skew-symmetric components as follows:

$$J_{ij} = \frac{1}{2}\Big(\frac{\partial u_i}{\partial x_j} + \frac{\partial u_j}{\partial x_i}\Big) + \frac{1}{2}\Big(\frac{\partial u_i}{\partial x_j} - \frac{\partial u_j}{\partial x_i}\Big) \tag{2.4}$$

We define accordingly the infinitesimal strain tensor as

$$\epsilon_{ij} = \frac{1}{2}\Big(\frac{\partial u_i}{\partial x_j} + \frac{\partial u_j}{\partial x_i}\Big) \tag{2.5}$$

and the local rotation tensor as

$$\frac{1}{2}\Big(\frac{\partial u_i}{\partial x_j} - \frac{\partial u_j}{\partial x_i}\Big) \tag{2.6}$$

The strain is defined by the tensor $\hat{\epsilon} = \{\epsilon_{ij}, i, j = 1, 2, 3\}$ function of the position of a volume element of the rigid body. All the information about the deformation driving the body from the reference to the deformed configuration is contained on the strain tensor.

2.2.1.2 The concept of stress

A solid body reacts to a deformation by developing internal forces and moments which balance the effect of the external loads. Let consider the situation in which a solid body is subjected to external forces. The system of forces acting on it can be composed of two main types: body forces and surface forces.

On the one hand, body forces depend uniquely by external fields acting on the body (for example the gravitational field) and can be summarised by the relation:

$$d\vec{F}_V = \vec{b}(x)dV \tag{2.7}$$

where $d\vec{F}_V$ represents the elementary total force applied to the volume element dV characterised by a volume force density of $\vec{b}(x)$.

On the other hand, surface forces deal with the interaction between neighbouring internal portions of deformable bodies (for example contact pressure or traction) and are formalised by the relation:

$$d\vec{F}_S = \vec{f}dS \tag{2.8}$$

where $d\vec{F}_S$ describes the elementary total force applied to the area element dS with a surface force density of $\vec{f}$. By universal convention, once defined the normal unit vector $\vec{n}$ to the surface element dS, the sign of the surface force is negative if opposite to $\vec{n}$ (case of compression forces), positive if on the same direction to $\vec{n}$ (case of tensile or traction forces).

The Cauchy theorem demonstrates analytically the existence of a unique 3×3 tensor such that:

$$\vec{f} = \hat{T}\vec{n} \tag{2.9}$$

where $\hat{T} = (\vec{f}_1, \vec{f}_2, \vec{f}_3)$, $\{\vec{f}_i, i = 1, 2, 3\}$ being the set of surface forces along the three cartesian axes. The demonstration of this fundamental theorem (see Appendix C of Ref. [6]) considers a generic point P within a material body surrounded by an infinitesimal tetrahedron reproduced in Fig. 2.3.

The Cauchy tetrahedron is defined by the three planes parallel to the three coordinate planes passing through the point P and a fourth plane with a normal unit vector $\vec{n}$ at a distance dh from P. The four tetrahedral faces are characterised by the elementary areas dA_1, dA_2, dA_3, dA_n with relative normal unit vectors $-\vec{e_1}$, $-\vec{e_2}$, $-\vec{e_3}$, $-\vec{n}$. Let f_1, f_2, f_3, f_n be the surface forces acting on each face of the tetrahedron and let $\vec{b}$ the internal body force.

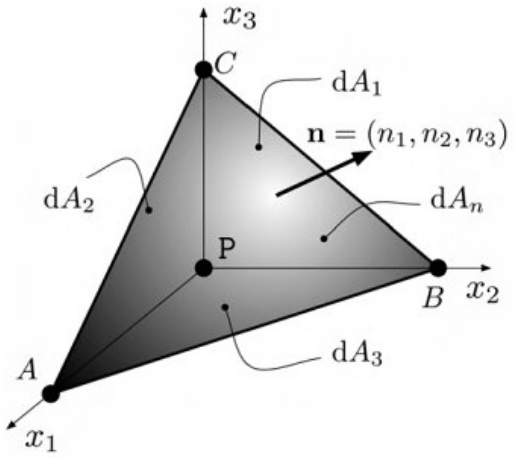

Figure 2.3: The Cauchy tetrahedron. Reproduced from Ref. [6].

The second law of dynamics states that:

$$\vec{f}dA_n - \vec{f}_1 dA_1 - \vec{f}_2 dA_2 - \vec{f}_3 dA_3 + \vec{b}dV = \rho\vec{a}dV \tag{2.10}$$

where $\vec{a}$ is the acceleration of the tetrahedron with mass ρdV. Since $dA_i = n_i dA_n$, $\forall i = 1, 2, 3$, from Eq. 2.10 follows:

$$\vec{f} - \vec{f}_1 n_1 - \vec{f}_2 n_2 - \vec{f}_3 n_3 + \frac{1}{3}\vec{b}dh = \frac{1}{3}\rho\vec{a}dh \tag{2.11}$$

having divided all terms by dA_n and by considering that $dV = \frac{1}{3}\rho dA_n dh$. In the limit $dh \to 0$ from Eq. 2.11 we obtain:

$$\vec{f} = \vec{f}_1 n_1 + \vec{f}_2 n_2 + \vec{f}_3 n_3 \tag{2.12}$$

which exactly demonstrates what stated by the Cauchy theorem in Eq. 2.9.

All the internal reactions to the deformation caused by surface and body forces are grouped in a physical quantity called stress represented by the tensor $\hat{T}$. The Cauchy theorem demonstrates that any surface vector $\vec{f}$ applied on a generic plane passing through a point P is exactly determined by the three force vectors acting on three mutually orthogonal planes. In terms of components we can write

$$f_i = T_{ij} n_j \tag{2.13}$$

In other words: it exists a tensor $\hat{T}$ such that

$$\vec{f} = \hat{T}\vec{n} \tag{2.14}$$

where $\hat{T} = (\vec{f_1}, \vec{f_3}, \vec{f_3},)$.

The Cauchy theorem allows to express the total surface force in Eq. 2.8 as

$$d\vec{F_S} = \hat{T}\vec{n}dS \tag{2.15}$$

namely in terms of components

$$dF_{S,i} = T_{ij}n_j dS \rightarrow \frac{dF_{S,i}}{dS} = T_{ij}n_j \tag{2.16}$$

The physical meaning of the tensor $\hat{T}$ can be better understood introducing a simple example. Let $\hat{T}$ be a diagonal tensor such that

$$T_{ij} = \sigma\delta_{ij} \tag{2.17}$$

From Eq. 2.16 we have

$$\frac{dF_{S,i}}{dS} = \sigma n_j \tag{2.18}$$

where σ describes the hydrostatic pressure applied on the solid body (negative in compression and positive in traction), often called load or applied stress. Therefore the stress tensor $\hat{T}$ can be thought as a vectorial pressure, with measurement unit Pa (typical values of stress in solid mechanics range from MPa to GPa).

2.2.1.3 The constitutive equation

In a solid body the relation between the applied deformation (strain) and the resultant internal force (stress) is described by the so called *constitutive equation*:

$$T_{ij} = f(\epsilon_{ij}) \tag{2.19}$$

Such equation, assumed *a priori* of the mechanical problem of interest, says that in every point of the solid body it exists a relation which biunivocally associates the stress tensor with the strain tensor. In linear elasticity theory the constitutive equation is linear under certain limits of strain and stress; moreover, the assumption of small deformations (see Sec. 2.2.1.1) must be always satisfied. Most materials subjected to small deformations are well described by a linear constitutive equation.

The generality of the constitutive equation needs to be projected into a specific mechanical problem by means of further simplifying hypotheses. In the common case where the response of the system is linear elastic, the associated constitutive equation becomes:

$$T_{ij} = C_{ijkh}\epsilon_{kh} \tag{2.20}$$

where C_{ijkh} are appropriate constants. Equation 2.20 is a generalisation of the famous Hooke's Law ($F = kx$) and has general validity, including every crystal symmetry.

The tensor $\hat{C}$ in Eq. 2.20 has 81 independent components and is known as the tensor of the elastic constants. By restricting our attention on a continuous medium, homogeneous (the mechanical behaviour of the body is equivalent in every point) and isotropic (the mechanical behaviour of the solid body is independent of the specific direction), Eq. 2.20 can be significantly simplified. This type of medium has a relevant importance both at theoretical and practical level. For such a medium the tensor $\hat{C}$ is defined by only 2 independent components, called *Lamé coefficients*: μ (*shear modulus*) and λ (*first Lamé coefficient*). Alternatively can be used the *Young modulus* E and the *Poisson's ratio* ν, or μ and the *bulk modulus* B. For a detailed derivation of the relations connecting the elastic moduli mentioned in this section we refer to Chapter 2 of Ref. [6]. In the next subsection the problem of boundary condition will be introduced as it is fundamental in fracture applications.

2.2.1.4 Boundary conditions

Most problems of the elasticity theory can be treated by means of appropriate boundary conditions which significantly simplify the mathematical formalism by projecting the problem into two dimensions. By making particular assumptions on the stress or on the strain, two particular boundary conditions deserve to be mentioned as they are widely used in fracture problems: *plane strain* and *plane stress*.

The condition of plane strain is satisfied when the displacement field $\vec{u}$ is strictly bi-dimensional, namely: $u_1 = u_1(x_1, x_2)$, $u_2 = u_2(x_1, x_2)$ and $u_3(x_1, x_2, x_3) = 0$. In plane strain conditions the strain tensor satisfy always the relations: $\epsilon_{33} = 0$, $\epsilon_{13} = 0$ and

$$\epsilon_{23} = 0$$

. In practical applications the plane strain conditions occur in the case of structures having one dimension much bigger than the other two. A typical example is represented by a cylinder with the height much bigger than the diameter of its base, with the load applied in the orthogonal direction to the axis of the cylinder. In fracture mechanics

problem this geometry is generally represented by thick plates, with length (x direction) much bigger than height (y direction) and depth (z direction).

The condition of plain stress is satisfied when $\hat{T}\vec{n} = 0$ in each point for a given fixed unit vector $\vec{n}$. By taking $\vec{n}$ parallel to x_3 direction, the plane stress condition yields $T_{33} = 0$, $T_{13} = 0$ and $T_{23} = 0$. In practical applications the plane stress conditions occur in the case of structures like a thin plate with one dimension much smaller than the other two. The load in this case is uniformly applied in the parallel direction of the thin plate, namely is uniform throughout its thickness. In fracture mechanics problems this geometry is generally represented by thin plates, with length (x_1 direction) and height (x_2 direction) much bigger than its depth (x_3 direction). In plane stress conditions the constitutive equation can be written in the compact form:

$$\begin{pmatrix} T_{xx} \\ T_{yy} \\ T_{xy} \end{pmatrix} = \frac{E}{1-\nu^2} \begin{pmatrix} 1 & \nu & 0 \\ \nu & 1 & 0 \\ 0 & 0 & 1-\nu \end{pmatrix} \begin{pmatrix} \epsilon_{xx} \\ \epsilon_{yy} \\ \epsilon_{xy} \end{pmatrix} \tag{2.21}$$

A thin plate containing a crack along the x_1 direction with plane stress boundary condition has been used in all my fracture simulations model and it will be described in detail in Sec. 2.6.2.

To conclude, elasticity theory describes the mechanics of materials in the continuum approximation. The knowledge of the material response to applied forces is enclosed into the elastic constants, or into the elastic moduli for specific loading geometries. An exhaustive derivation of the equations reported in this section can be found in Ref. [6] and in Ref. [5]. The following section will focus on a material containing a crack on the assumption of validity of elasticity theory.

2.2.2 Linear Elastic Fracture Mechanics

The study of fracture behaviour in a material where stress varies linearly with strain is called *Linear Elastic Fracture Mechanics* (LEFM), namely fracture mechanics within the linear elasticity framework. This branch of science saw its first pioneers within the engineering community of the post industrial revolution era. Since that time it was clear, through empirical observation, that materials under stress react by straining and eventually failing for a critical value of the applied load. According to the ways in which the failure process occurs, materials were divided in two main categories: brittle and ductile.

A schematic diagram showing stress-strain curves for brittle and ductile materials is

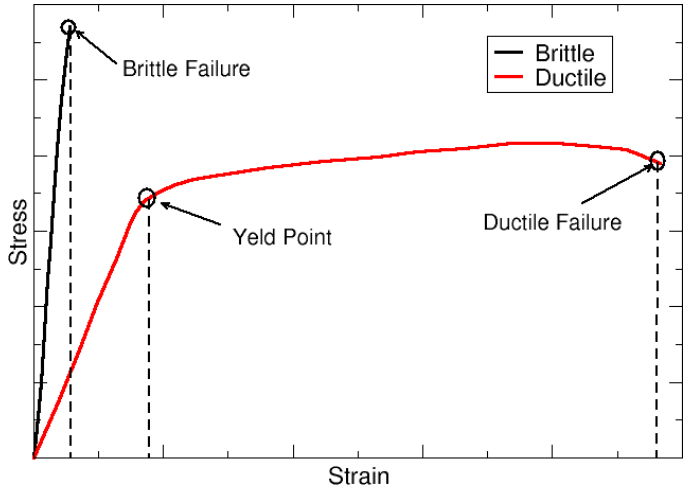

Figure 2.4: Schematic stress-strain curves for brittle (black line) and ductile (red line) materials.

reported in Fig. 2.4. Brittle materials strain linearly with increasing stress until failure, whilst plastic materials experience a significant plastic deformation followed eventually by a failure for higher values of strain. The brittle failure occurs in the elastic regime of the stress-strain curve for a certain value of the applied load. On the contrary, ductile fracture takes place only after an irreversible deformation of the material structure. For these reasons, when fractured, ductile materials present several asperities on the surfaces opened by the crack, whilst brittle materials can be severed along a crystal plane, leaving a flat and smooth surface without any sign of deformation. Ceramics like glass and semiconductors like silicon, are model examples of brittle materials, whilst metals are ductile.

Despite the successful design of engineering structures based on this empirical knowledge, many aspects of the fracture mechanism were obscure. Why the critical applied stress could significantly vary within the same material? What are the causes that lead a material to experience failure in so many diversified ways? At the beginning of the 20th century the engineering community started a theoretical investigation on the causes of unexpected and catastrophic failures in an attempt to answer these questions. We will retrace this journey in the following sections, from the first theories based on empirical observations to the latest hybrid models combining classical and quantum mechanics.

2.2.2.1 Stress concentration

In a famous paper published by Inglis [7] in 1913 for the Institution of Naval Architects, the author clearly explains the concept of stress concentration:

> The destructive influence of a crack is a matter of common knowledge, and is particularly pronounced in the case of brittle non-ductile materials. This influence is turned to useful account in the process of glass cutting. A fine scratch made on the surface produces such a local weakness to tension that a fracture along the line of the scratch can be brought about by applied forces which produce in the rest of the plate quite insignificant stresses.

Thus, despite a lack of theoretical investigation into the fundamental causes of fracture propagation, a century ago the engineering community was wholly aware of the detrimental effects caused by cracks, flaws or any kind of imperfection within the material's body.

The idea of "critical applied stress" was a common practice in engineering design. This concept was based on the assumption that a solid should break at a specific stress level. However, this empirical knowledge was not sufficient to predict, and therefore avoid, catastrophic and unexpected failures, which several times caused the loss of human life. Moreover, there was no theory capable of explaining why brittle materials like glass break suddenly for relatively low loading conditions with respect to ductile materials like metals. A systematic study onto this problem was urgently needed, and Inglis was the first to approach the problem from a mathematical point of view.

Within the approximation of linear elasticity theory, in his paper to the Institution of Naval Architects in London he demonstrated theoretically two important results outlined below:

- the stress at the end of the crack varies with its curvature and size;
- the stress is proportional to the square root of the length of the crack and inversely proportional to its radius of curvature.

Taking the particular case of a plate containing an elliptical hole of length $2l$ and thickness $2b$, subjected to a remote uniaxial load σ along the y direction (as shown in Fig. 2.5), Inglis postulated the existence of a stress enhancement T_{yy}^{tip} at the crack tip described by the equation:

$$T_{yy}^{tip} = \sigma \left(1 + \frac{2l}{b}\right) = \sigma \left(1 + 2\sqrt{\frac{l}{\rho}}\right), \tag{2.22}$$

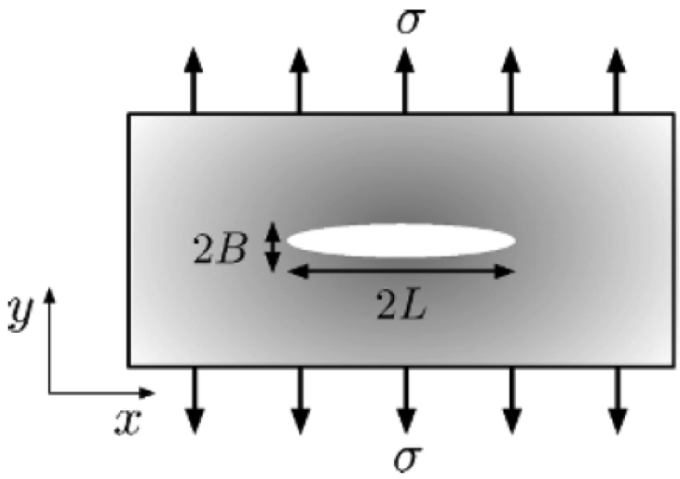

Figure 2.5: Schematic diagram of plate containing an elliptical hole subjected to the applied uniform load σ along the y direction. Reproduced from Ref. [5].

where $\rho = b^2/l$ is the radius of curvature at the crack tip. T_{yy} accounts for the stress field caused by the strain of the structure resulting from a uniform external load σ along the y direction.

In the ideal case of a perfect brittle crystalline material with no flaws or voids, the stress field would be uniform within the material's volume. The presence of a crack introduces a stress enhancement in the proximity of the crack tip which explains why a material can fail for an applied stress σ that is much lower than the theoretical failure stress σ_f. According to Eq. 2.22, the morphology of the crack (and not its absolute dimension) controls the magnitude of the stress enhancement term, leading to the paradox that a material containing a slit crack with $\rho \to 0$ should fail for an infinitesimally small load. Even removing this singularity, which arises from neglecting the atomic structure of materials, experimental results were in clear disagreement with Inglis theoretical findings, which highly overestimated the weakening of materials. [8]

Focusing on the role of the local stress at the singularity of the crack tip within continuum elasticity theory gave an important qualitative explanation of the effect of stress concentration. However, it was not still satisfactory from a quantitative point of view. A consistent theoretical model capable of predicting the start of material failures was needed.

2.2.2.2 Griffith energy criterion

Only eight years later, Griffith attacked this problem from a new standpoint based on the concept of the conservation of the energy. Working at the Royal Aircraft Establishment on the effect of surface treatment on the strength of metallic machines, he pointed out at the discrepancies between the well established hypothesis of "maximum applied stress" and the results of alternating stress tests. The analysis and conclusions drawn from this study were published in 1921 in the paper *The phenomena of rupture and flow in solids* [8], where the author introduced a new theoretical criterion of rupture with these words:

> According to the well-known "theorem of minimum energy", the equilibrium state of an elastic solid body, deformed by specified surface forces, is such that the potential energy of the whole system is a minimum. The new criterion of rupture is obtained by adding to this theorem the statement that the equilibrium position, if equilibrium is possible, must be one in which rupture of the solid has occurred, if the system can pass from the unbroken to the broken condition by a process involving a continuous decrease in potential energy. In order, however, to apply this extended theorem to the problem of finding the breaking loads of real solids, it is necessary to take into account of the increase in potential energy which occurs in the formation of new surfaces in the interior of such solids.

The simple and powerful concept communicated by the Griffith's criterion consists of describing the advance of the crack in energetic terms. The presence of the crack within a strained body introduces, as a matter of fact, a local region of stress release. Therefore, its advance consists on one hand of a decrease of the elastic energy stored and on another hand of the work spent to open two newly created surfaces. The total energy U of a solid containing a crack under constant applied stress σ_A is represented by the balance equation:

$$U = U_E + U_S, \tag{2.23}$$

where U_E is the elastic energy stored in the solid under strain and U_S the free energy necessary to open the new crack surfaces. As the crack of length $2l$ extends of an infinitesimal distance dl, the bonds within a strip of width dl relax, decreasing the elastic energy accordingly:

$$\frac{\mathrm{d}U_E}{\mathrm{d}l} < 0. \tag{2.24}$$

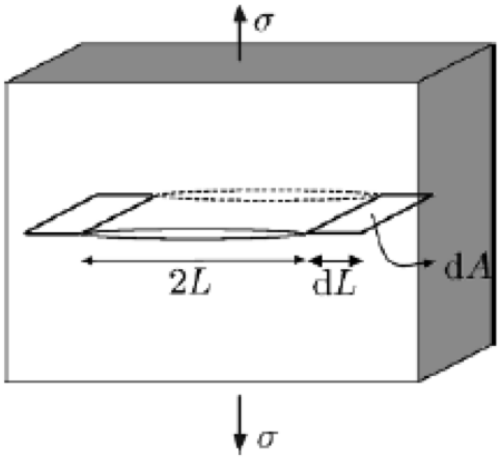

Figure 2.6: The slit crack model used by Griffith to calculate the critical conditions for elementary crack advancement. The elementary area $\mathrm{d}A$ is obtained by multiplying the advancement $\mathrm{d}l$ of the crack by the thickness of the plate Z. Reproduced from Ref. [5].

On the other hand, an increase of the surface energy during crack extension accounts for the work needed to break molecular bonds and open two newly created surfaces behind the crack:

$$\frac{\mathrm{d}U_S}{\mathrm{d}l} > 0. \tag{2.25}$$

The equilibrium requirement for a stationary crack on the verge of advancing is then described by the Griffith energy-balance criterion:

$$\frac{\mathrm{d}U}{\mathrm{d}l} = 0. \tag{2.26}$$

The solution of this equation is a stationary point, namely a maximum for the function expressed by Eq. 2.23.

Integrating the elementary energy contributes $\mathrm{d}U_E$ and $\mathrm{d}U_S$ for the elementary crack advancement $\mathrm{d}l$, we can obtain the critical conditions at which the crack advancement occurs. Griffith used the stress analysis conducted by Inglis to calculate the strain energy:

$$U_E = -\frac{\pi Z l^2 \sigma^2}{E}, \tag{2.27}$$

where Z measures the thickness of the plate along the z direction, σ is the applied stress and E' is the effective Young's modulus.

The surface energy is obtained considering the energy needed to break molecular bonds during crack advancement. This energy is a characteristic parameter of the material and is expressed in terms of the surface energy density γ, namely the energy per unit surface opened by the crack. Thus we obtain:

$$U_S = (2A \times \gamma) \times 2, \tag{2.28}$$

where $2A$ refers to the area of two newly opened surfaces, while the factor of 2 outside the brackets accounts for the double ended crack.

By substituting Eqs. 2.27 and 2.28 in Eq. 2.23 and solving Eq. 2.26 we obtain the necessary critical conditions for a stationary crack to advance:

$$4lZ\gamma - \frac{\pi Z l^2 \sigma_c^2}{E'} = 0;$$

$$\sigma_c = \sqrt{\frac{2\gamma E'}{\pi l_c}}, \tag{2.29}$$

$$l_c = \frac{2\gamma E'}{\pi \sigma^2}, \tag{2.30}$$

where σ_c and l_c represent respectively the critical applied stress and the critical crack length. Griffith verified this theoretical analysis by measuring the normal component of the applied stress to glass fracture specimens, finding a remarkable agreement. [8] An important step achieved by Griffith was proving that the critical conditions for crack advancement are crack-size dependent (see Eq. 2.30). Moreover, its criterion, based on the conservation of the energy, predicts the minimum stress that should be applied to a brittle material in order to allow a pre-existent over-critical crack to propagate at certain velocity within the body (see Eq. 2.29). An exhaustive review of the Griffith criterion can be found on the first chapter of "Fracture of Brittle Solids" in Ref. [3].

2.2.2.3 Irwin stress field

Starting from the Griffith milestone principle, Irwin developed the body of fracture mechanics, aiming to introduce functional quantities characterising the driving force for fracture.[9] The calculation of the stress field near the crack tip was one of these important quantities never investigated before. Moreover, a physical quantity linking the mechanical energy released by crack advancement and the surface energy was needed for practical purposes.

Turning the attention to the mapping problem of the stress field, three principal modes of fracturing a material can be defined. Mode I, known as the tensile mode,

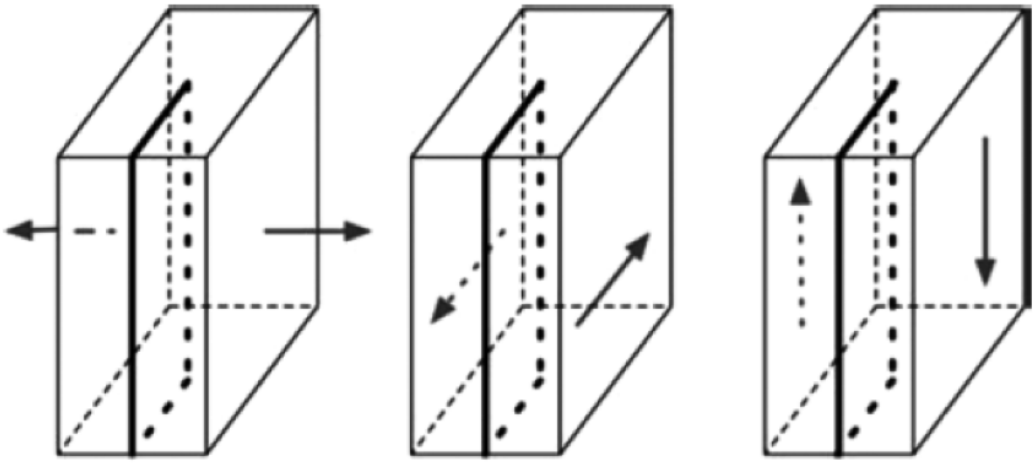

Figure 2.7: The crack opening modes. From the left to the right: tensile (I), sliding (II), tearing (III). Reproduced from Ref. [5].

consists of opening a crack by applying a negative pressure on the normal direction to the crack plane (on the left in Fig. 2.7). Mode II, or the sliding mode, is obtained by sliding the two crack surfaces in opposite directions across the direction of crack propagation (on the centre in Fig. 2.7). Mode III, or the tearing mode, is attained by pulling apart the crack surfaces along the crack front (on the right in Fig. 2.7).

According to the constitutive equation of elasticity theory, Irwin calculated the resulting stress field near the tip (see Fig. 2.8) using polar coordinates for an infinitesimally narrow slit crack for the three main geometries:

$$T_{ij} = \frac{K_I}{\sqrt{2\pi r}} f_{ij}^{I}(\theta) + \frac{K_{II}}{\sqrt{2\pi r}} f_{ij}^{II}(\theta) + \frac{K_{III}}{\sqrt{2\pi r}} f_{ij}^{III}(\theta), \tag{2.31}$$

where the functions $f_{ij}(\theta)$ contain all the angular dependence of the field, K^I, K^{II} and K^{III} are the stress intensity factors for the respective opening modes, r the distance from the crack tip and θ the angle formed by r and the crack direction. The most relevant mode of the three, both in theory (as we have seen in the Inglis and Griffith approach) and in many experimental applications, is the tensile mode, so from now on we will refer to K_I as K. The Irwin near-tip solution for $\theta = 0$ is described by the limit equation:

$$K = \lim_{r \to 0} \left(\sqrt{2\pi r} T_{yy}(r, \theta = 0) \right) \tag{2.32}$$

Neglecting the singularity of the stress at $r = 0$ introduced by requiring the crack slit

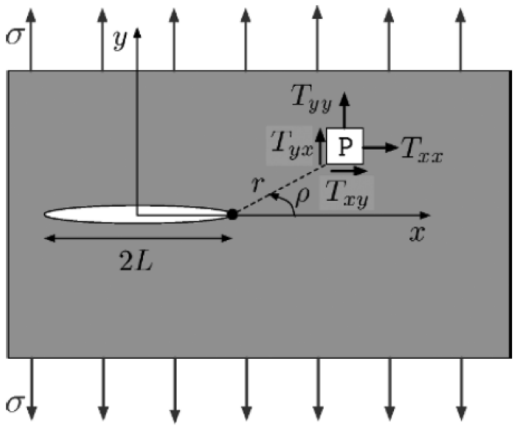

Figure 2.8: Tensile components of the stress tensor in the zone near the crack tip. Reproduced from Ref. [5].

to be perfectly sharp, a significant result achieved by the Irwin near-tip solutions is that the crack opening displacement, namely the crack profile, is parabolic.

The stress intensity factor depends only on the applied loading and specimen geometry, consequently determining the intensity of the local field. For this reason K can be considered a powerful fracture parameter. In fact, the fracture toughness of a material, commonly denoted by K_c, represents the stress intensity factor at which a crack is observed to propagate in a laboratory sample. For a detailed derivation of the Irwin solutions see Chapter 2 of Ref. [3].

Irwin's work pointed out also the necessity of defining a quantity able to link in practical problems the mechanical energy released by the advancing crack with the surface energy spent to break the atomic bonds. Following Griffith's model he thus defined the mechanical energy release rate (called G in honour of Griffith who pioneered the concept) as the energy released by the crack per unit area of crack surface created:

$$G = -\frac{\mathrm{d}U}{\mathrm{d}A}. \tag{2.33}$$

For the special case of a crack where the length l is sufficient to define the crack area (a geometry commonly used in most of computational models) the above equation can be rewritten in terms of the unit crack length and the unit crack front:

$$G = -\frac{\mathrm{d}U}{\mathrm{d}l}. \tag{2.34}$$

This definition is independent of the loading geometry.

The definition of the energy release rate G introduces the possibility to make energy balance arguments directly comparable with experimental quantities like the surface energy density γ. However, we should stress the equivalent importance of K and G as fracture parameters. If we integrate the strain energy density over the interfacial crack area subsequent to an infinitesimal crack advancement dl we obtain:

$$G = \frac{K^2}{E'}. \tag{2.35}$$

See Ref. [3] for a detailed derivation of the result.

Finally, the Griffith criterion (Eq. 2.26) can be generalised, balancing the energy release rate at the crack tip with the cost of opening two new fracture surfaces:

$$G_c = 2\gamma \tag{2.36}$$

where γ is the surface energy density and G_c is the critical energy release rate. Equation 2.36 governs the condition of crack initiation for an ideal brittle elastic material, the surface energy γ being the only mechanism of resistance to fracture propagation. By considering the case when other energy dissipation mechanisms cannot be neglected, Eq. 2.36 assumes the form:

$$G_c = \Gamma, \tag{2.37}$$

where the fracture energy Γ is nothing but a generalisation of the surface energy ($\Gamma_0 = 2\gamma$ for an ideal brittle static crack at critical loading conditions).

2.2.2.4 Crack dynamics

Following the Griffith energy balance criterion in Eq. 2.37, the necessary condition for crack propagation becomes:

$$G > \Gamma. \tag{2.38}$$

What happens in this branch of fracture energies where the crack can in principle propagate at finite speed?

The first general approach to the dynamic fracture problem was proposed by Mott [10] in 1948. The natural extension of the Griffith energy balance to the case of a running crack finds its expression in the formulation of a dynamic theory of fracture [4]. The

equation governing the crack dynamics takes the form:

$$G(v) = \Gamma(v) \tag{2.39}$$

where v represents the crack speed.

By knowing the fracture energy $\Gamma(v)$ and the energy release rate $G(v)$, the crack speed can be predicted. Whilst $\Gamma(v)$ can be either measured or calculated, $G(v)$ has been analytically calculated only in two particularly simple cases: a medium containing a semi-infinite crack in an infinite plate subjected to any tensile loading [4]; a medium containing a semi-infinite crack within an infinitely long strip subjected to constant tensile loading [11].

It is useful expressing the equation of motion of fracture dynamics referring to simple geometries. For a semi-infinite crack in an infinite half plane, LEFM predicts the universal equation of motion, known also as "Freund equation" [4]:

$$v = c_R \left(1 - \frac{\Gamma(v)}{G}\right), \tag{2.40}$$

where c_R is the speed of surface waves in the medium, namely the Rayleigh wave speed, $\Gamma(v)$ is the velocity dependent fracture energy, approximately equal to 2γ at low speeds, and G is the static strain energy release rate, i.e. the flow of elastic energy to the crack tip.

The main prediction made by Eq. 2.40 is an asymptotic behaviour of the crack speed as the crack lengthens, with c_R being the limiting speed (see Sec. 4.2.1 for a thorough analysis of the Freund equation of motion). On the contrary, experiments report measures of limiting speeds in typical brittle materials like polymers and silicon between 20 and 80 % of this value [12, 13, 14, 15, 16]. These discrepancies between theory and experiments have their roots in the unsolved question of fracture mechanics: What really happens at the crack tip? An answer to this question can be only found in the fundamental passage from a continuum view of the elastic medium to the real discrete nature of matter.

2.3 From continuum to discrete

Fracture mechanics can be considered a theoretical background of fundamental importance in approaching fracture problems. By following the historical process of this branch of material science in Sec. 2.2, we also introduced the fundamental principles

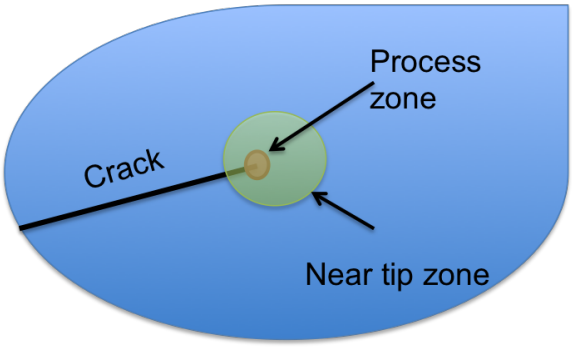

Figure 2.9: Schematic picture of fracture mechanics. The presence of the crack within a material body introduces three spatial regions: the process zone (red), the near tip region (green) and the outer elastic region (blue).

governing the formation and the propagation of a crack within an elastic body. A clear picture describing the structure of fracture mechanics has been proposed by Irwin and Orowan (see a related review article in Ref. [15] p. 10). They proposed the existence of three regions within a medium containing a crack: the process zone, the near crack tip region and the outer elastic region (highlighted respectively by red, green and blue in Fig. 2.9).

The process zone, or cohesive zone, is the region of the material immediately surrounding the crack tip. In this region the crack advancement consists in breaking atomic bonds one after one another, transcending completely the realm of fracture mechanics. The only assumption made by LEFM is strictly empirical, describing the fracture dynamics through the general concept of the fracture energy Γ. Outside of the cohesive zone is the so called near-tip zone, where the response of the material to applied forces is incorporated by the stress intensity factor K. If L is the size of the material where macroscopic forces are applied, the near-tip zone scales as $\sqrt{L}$. Finally, far from the crack tip is the linear elastic region, where the simple assumptions of linear elasticity apply.

In spite of the broad range of correct predictions yielded by LEFM, many features of the fracture dynamics can not be explained. Amongst several discrepancies between theory and experiments, we remind two extreme cases of the fracture dynamics: the crack initiation and the maximum attainable crack speed. From one hand, at initiation, no crack is observed propagating when pulled apart with a loading scarcely higher than G_c, but always for values significantly higher than this critical predicted value. From the other hand, as we have pointed out in Sec. 2.2.2.4, pulling a material with very

high loading, the measured speed of the crack is always a fraction of the predicted theoretical value c_R.

It must be recognised that there is a fundamental breakthrough in the passage from macroscopic to nanoscopic, as highlighted in the schematic picture in Fig. 2.9. Mapping the problem in an atomistic resolved lattice removes the mathematical singularity at the crack tip shown by analytical approaches. It is then in the process zone, namely the crack tip itself, where the first nanoscopic models attempted a description of the elementary step for crack advancement: the bond breaking event.

In the early 1970's, Thomson et al. [17] studied theoretically the lattice structure of cracks by modelling two semi-infinite chains of atoms bonded horizontally by bendable springs and vertically by stretchable springs. Their analysis showed the existence of a stress stability range for the crack around the Griffith point σ_c over which the crack is stable or lattice trapped, namely not prone to advance or retract. In the 1980's, Slepyan used two-dimensional lattice models to study dynamics crack instabilities, finding out that fracture propagation involves the emission of high-frequency waves. [18] In the 1990's, Marder [19] investigated the steady states of a crack moving in a triangular lattice, highlighting the existence of a critical velocity beyond which the crack deviates from a straight path by undergoing oscillations observed in experiments [12, 13] (see Sec. 4.2.1 for a detailed description of this phenomenon).

These pioneering atomistic models highlighted for the first time the necessity of going beyond the continuum approximation, anticipating the future advent of molecular dynamics studies. Before going into the details of the modern computational methods used to study fracture at the atomic scale, a relevant fracture geometry, particularly useful for computational purposes, is described in the next subsection (Sec. 2.3.1).

2.3.1 The thin strip geometry

Since the Griffith pioneering work, the fracture problem has been modelled in a particular useful geometry, both from theoretical and experimental point of view. The thin strip geometry is the particular configuration where the crack field is constrained within a thin strip of height h along the direction orthogonal to the crack plane, clamped on the top and the bottom by fixed displacement boundary conditions. This special arrangement is particularly useful to study the crack dynamics under the condition of constant energy release rate.

By fixing the top and bottom boundaries where the load is applied precludes the exchange of mechanical energy between the elastic body and its surroundings. This

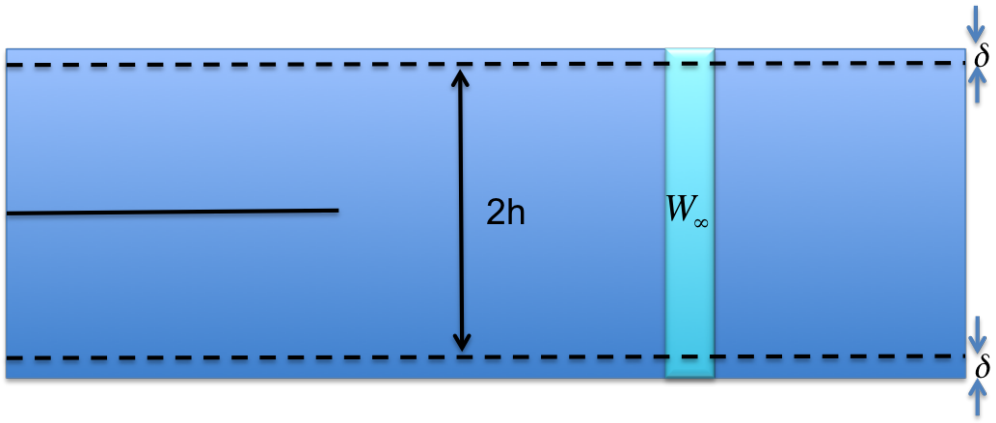

Figure 2.10: The thin strip geometry. The top and bottom boundaries of the strip are fixed and displaced vertically by an amount δ. The light blue stripe represents a material region with elastic energy density equal to W_∞ (see text for explanation).

permit us to state that the only global energy variation during crack advance is the elastic energy, provided that the deformation due to crack progress is at equilibrium. This elastic energy change due to crack growth is exactly the energy release rate, expressed by the following equation:

$$G = \frac{1}{2}\frac{E}{1-\nu^2} \cdot \epsilon^2 \cdot h \tag{2.41}$$

where E is the Young's Modulus, ν the Poisson's ratio, ϵ the applied strain and h the height of the slab.

In this loading configuration, the horizontal edges of the strip are supplied with a uniform normal displacement δ, so the applied strain is $\epsilon_0 = \delta/h$. The uniaxial tension felt by the slab far ahead of the crack is the stress $\sigma_0 = E'\epsilon_0$, where $E' = E/1-\nu^2$ is the effective Young modulus and ν the Poisson ratio. Therefore the elastic energy per unit length and per unit thickness far ahead of the crack tip ($x \to \infty$) is

$$W_\infty = \frac{1}{2}E'\epsilon_0^2 \cdot 2h = \frac{\delta^2 E'}{h} \tag{2.42}$$

where $2h$ is the height of the slab.

Far behind the tip the energy density is zero because of the presence of the crack. This discontinuity is explained by thinking that the energy supplied to the crack tip is

equal to W_∞, so the energy release rate is simply

$$G = W_\infty = \frac{\delta^2 E'}{h} \tag{2.43}$$

In summary, the simple parameter represented by the spatial displacements δ of the boundaries allows to make straightforward experimental measures of the energy release rate, directly comparable with analogous theoretical estimates. This geometry is definitely the most used in practical fracture problems, and therefore also in the majority of computational studies. The necessity of studying fracture at the nanoscale level introduces the concept of computational atomistic studies of fracture.

2.4 Modelling fracture at the atomic scale

Since their advent computers have provided new ways to investigate the laws of nature. The equations that describe the laws of nature are usually not exactly solvable via analytical approaches. Theory provides an approximate description of physical systems, and even using approximations, the aim of reproducing exactly the model becomes increasingly difficult as the number of objects involved in the problem increases. In this scenario, the availability of the powerful tool represented by computers bridges this gap, allowing many different analyses to be carried out for the first time.

The use of computer simulations lies in the middle, ground between theory and experiment. On the one hand, we can compare the results of real experiments with the calculations of a model system, and if the two disagree we can improve the model; on the other hand, comparing the result of a simulation with the predictions of the theory for the same model allows us to see if the theory is working well. Moreover, we can predict properties of materials that have not yet been created, or even better, explore from scratch totally unknown environments. From classical molecular dynamics to quantum mechanics methods, we will review their fundamental principles, finally exploring a way of combining them together in order to interpret fracture at the atomic level.

2.4.1 Classical Molecular Dynamics

Molecular dynamics (MD) is a computational simulation technique that follows the time evolution of an ensemble of interacting atoms by integrating their equations of motion:

$$\vec{F_i} = m_i \vec{a_i} \tag{2.44}$$

for each atom i in a system of N atoms, where m_i is the atom mass, $\vec{a_i} = d^2\vec{r_i}/dt^2$ its acceleration, and $\vec{F_i}$ the force acting upon it due to the interaction with other atoms. Forces are generally derived from potential energy functions $V(\mathbf{r_1}, ..., \mathbf{r_n})$ which strictly depend from the positions of the atoms and wholly characterise the materials properties (see Ref. [20] for a general introduction to MD).

Integrating equation 2.44 in order to follow the trajectory of the interacting particles is the main task of a MD program. Time integration algorithms are based on *finite difference methods*, where time is discretised on a finite grid, the time step Δt being the distance between consecutive points on the grid. Knowing positions $r(t)$ and their time derivatives $\dot{r}$ at a time t, the integration scheme gives the same quantities at a later time $t+\Delta t$. The Velocity-Verlet algorithm [21, 22] is widely used in MD programs since it provides a good compromise between efficiency and accuracy:

$$r(t + \Delta t) = r(t) + \dot{r}\Delta t + \frac{1}{2}\frac{F(t)}{m}\Delta t^2 + O(\Delta t^4), \tag{2.45}$$

$$\dot{r}(t + \Delta t) = \dot{r}(t) + \frac{1}{2}\Big[\frac{F(t)}{m} + \frac{F(t) + \Delta t}{m}\Big]\Delta t + O(\Delta t^4), \tag{2.46}$$

with m representing the particle mass and $F(t)$ the force acting on it at the time t.

MD simulations using the Velocity-Verlet algorithm conserve the total energy generating the micro-canonical ensemble NVE, where number of particles N, volume V and total energy E are constant. However, in order to match experimental conditions more closely, it is often convenient to perform simulations in other ensembles, keeping constant the temperature of the system instead of the energy (NVT), or the pressure instead of the volume (NPT). Andersen introduced this possibility for the first time in the context of constant pressure MD simulations, reformulating the Lagrange equations of motion of the system. [23] It is particularly useful to work with the so called canonical ensemble NVT, with constant temperature achieved via a thermostat which adds or removes heat from the system. The Langevin thermostat [24] is an approach that samples the canonical ensemble correctly, adding to the equations of motion a dissipative term representing viscous damping due to fictitious heat bath particles and a random force to represent the effect of collisions with those particles:

$$F_i = -\nabla_i V - \beta\dot{r_i} + \xi_i. \tag{2.47}$$

In Eq. 2.47 V represents the potential energy function of the system, β is the damping coefficient and ξ_i are the random forces drawn from a gaussian distribution with zero

mean and unit variance scaled according to the Stokes-Einstein fluctuation-dissipation relation for the diffusion coefficient, i.e. by a factor

$$\sqrt{\frac{2mk_BT\beta}{\Delta t}}, \tag{2.48}$$

where m is the particle mass, T the simulation temperature and Δt the molecular dynamics time-step.

The computer calculates a trajectory in a 6N-dimensional phase space (3N positions and 3N momenta). However, such a trajectory is not usually particularly relevant by itself because it cannot be compared directly with experimental data. For this reason MD can be viewed as a statistical mechanics method, where physical quantities are represented by averages over configurations distributed according to a certain statistical ensemble. As a typical experiment measures an average property, averaged over a large number of particles and over the time of the measurement, MD aims to compute averages of different physical properties and therefore to compare them with experimental results.

To conclude, molecular dynamics studies the interactions of atoms with each other. These interactions are described by forces, usually obtained as the gradient of a potential energy function, depending on the positions of the particles. Therefore selecting an appropriate potential becomes of crucial importance in order to achieve a good description of the system.

2.4.1.1 Interatomic potentials

The potential energy function $V(\mathbf{r_1}, ..., \mathbf{r_n})$ for a specific material plays a key role in molecular dynamics as forces are derived from it. The main effort is understanding how such a function of the coordinates can be close to the behaviour of a real material. Usually, a classical interatomic potential is initially derived by choosing an appropriate functional form according to the complexity of the system. Then, the parameters of this functional are fitted to reproduce relevant physical properties (elastic constants, Young's and bulk modulus, cohesive energy are typical properties relevant to fracture studies), where the fit target can either be experimental measures or ab-initio calculations. In the last case, the interatomic potential is an approximation to the underlying quantum mechanics.

In classical MD, atoms are considered point-like particle interacting via a potential energy function decomposable into a sum of one-body, two-body or many-body

contributions

$$V(\{\mathbf{r_i}\}) = \sum_i V_1(\mathbf{r_i}) + \sum_{i<j} V_2(\mathbf{r_i}, \mathbf{r_j}) + \sum_{i<j<k} V_3(\mathbf{r_i}, \mathbf{r_j}, \mathbf{r_k}) + ... + V_N(\mathbf{r_i}, ..., \mathbf{r_n}), \quad (2.49)$$

where the conditional sums avoid double-counting. The one-body term V_1 represents an additive energy term acting on any atom, therefore can only be an external force applied to the whole system (if the system is considered isolated this term is absent). The two-body term V_2 describes the elementary interaction between any couple of atoms, and is usually a function of the bond length $r_{ij} = |\mathbf{r}_j - \mathbf{r}_i|$. Finally, the three-body term V_3 accounts for the interaction between any three atoms of the system, and is a function of the bond lengths r_{ij} and r_{ik} and the angle θ_{ijk} between the bonds ij and ik. Typical interatomic potentials for MD studies contain two- and three-body terms and can be written in the parametric form

$$V(\{\mathbf{r_i}\}) = \sum_{i<j} V_2(r_{ij}) + \sum_{i<j<k} V_3(r_{ij}, r_{ik}, \theta_{ijk}). \quad (2.50)$$

A fundamental aspect of modelling material properties with MM approach is the tradeoff between two aspects intrinsically in contrast: reproducibility and accuracy. From one hand, the functional form should be able to capture the general mechanisms of bonding of the material under investigation. On the other hand, the fitting process narrows the general functional to the specific material under investigation, often to a specific phase of the material, making sure that the relevant properties are reproduced with an accuracy comparable to the experiment or to quantum mechanical estimates. Therefore, an interatomic potential may be very accurate in faithfully reproducing physical properties of a specific material within the extent of the specific properties that have been used in the fitting process. Bearing in mind this important limit, the MM approach still represent a fundamental tool in modelling solid state systems. An example of interatomic potential, used in this work to describe brittle fracture, will be described in the following section.

2.4.1.2 The Stillinger-Weber potential

The Stillinger-Weber (SW) potential [25] was one of the first attempts at modelling semiconductors with an interatomic potential. Starting from the knowledge that simple pair potentials were not able to describe semiconductor structures, the authors proposed a model potential-energy function comprising both two- and three-atom contributions

to describe interactions in solid and liquid forms of Si. Diamond structure of Si crystals consists of atoms held in place by strong and directional bonds, so a good description of it must take into account not only the energetic term dependent from the bond distance (two body term) but also one part related to the bond angles (three-body term).

The SW potential is the sum of two- and three-body potentials:

$$V_{SW} = \sum_{i<j} v_2(r_{ij}) + \sum_{i<j<k} v_3(\mathbf{r_i}, \mathbf{r_j}, \mathbf{r_k}), \tag{2.51}$$

where

$$v_2(r_{ij}) = \frac{\epsilon f_2(r_{ij})}{\sigma}, \tag{2.52}$$

$$v_3(\mathbf{r}_i, \mathbf{r}_j, \mathbf{r}_k) = \epsilon f_3 \left(\frac{\mathbf{r}_i}{\sigma}, \frac{\mathbf{r}_j}{\sigma}, \frac{\mathbf{r}_k}{\sigma} \right), \tag{2.53}$$

with ϵ representing the well depth energy chosen to give f_2 depth -1, and σ the value of r_{ij} at which $v_2(r_{ij}) = 0$ to make $f_2'(r_{min}/\sigma)$ vanish. If f_2 is a function only of the scalar distance r_{ij}, f_3 has full translational and rotational symmetry. The reduced pair potential f_2 was selected to have the form

$$f_2(r_{ij}) = A(Br^{-p} - r^{-q})e^{[(r-a)^{-1}]} \tag{2.54}$$

where the parameters are positive and with a representing the cutoff distance at which the f_2 goes to zero without discontinuities in any r derivatives.

The reduced three-body potential has the form

$$f_3 \left(\frac{\mathbf{r}_i}{\sigma}, \frac{\mathbf{r}_j}{\sigma}, \frac{\mathbf{r}_k}{\sigma} \right) = h(r_{ij}, r_{ik}, \theta_{jik}) + h(r_{ji}, r_{jk}, \theta_{ijk}) + h(r_{ki}, r_{kj}, \theta_{ikj}), \tag{2.55}$$

where θ_{jik} is the angle between r_{ij} and r_{ik} subtended at vertex i, etc. The function h belongs to a two-parameter family ($\lambda, \gamma > 0$):

$$h(r_{ij}, r_{ik}, \theta_{jik}) = \lambda e^{[\gamma(r_{ij}-a)^{-1}]+\gamma(r_{ik}-a)^{-1}]\times(\cos\theta_{jik}+\frac{1}{3})^2} \tag{2.56}$$

provided that both r_{ij} and r_{ik} are less than the cutoff radius a, otherwise h vanishes identically. The trigonometric part of the expression clearly discriminates in favour of tetrahedral bond angle $\theta_t = 109.47°$ among triplets of bonded atoms. In order to describe accurately interactions in solid and liquids forms of Si, the most satisfactory parameter set is reported in Table 2.1.

The SW model has been largely used to study silicon properties even if it shows deficiencies when it comes study the brittle cleavage of silicon. [26] It has been shown

Table 2.1: Parameter set of SW potential [25].

A	B	p	q	a	λ	γ
7.049556277	0.6022245584	4	0	1.80	21.0	1.20

that the inability to reproduce the brittle behaviour in covalent materials depends on the short range character of the potential. [27] However, this potential represents a good candidate to use in a brittle fracture multi-scale hybrid scheme: it is easily implemented, computationally convenient and it reproduces fairly well crucial properties of silicon as the surface energy density and the elastic constants (see Ref. [25]). The critical zone of the fracture, where atomic scale phenomena are responsible of the brittleness, is the task of quantum potentials.

2.4.2 Quantum Mechanics

Real materials are made by atoms. In principle, the only theory able to describe atoms is quantum mechanics. A system of interacting atoms is described by the Hamiltonian

$$\begin{aligned}\hat{H} \;=\; & \sum_I \frac{P_I^2}{2M_I} + \sum_i \frac{p_i^2}{2m} + \frac{e^2}{2}\sum_I \sum_{J\neq I} \frac{Z_I Z_J}{|\mathbf{R}_I - \mathbf{R}_J|} + \\ & + \frac{e^2}{2}\sum_i \sum_{j\neq i} \frac{1}{|\mathbf{r}_i - \mathbf{r}_j|} - e^2 \sum_I \sum_i \frac{Z_I}{|\mathbf{R}_I - \mathbf{r}_i|},\end{aligned} \tag{2.57}$$

where $\mathbf{R} = \{\mathbf{R}_I\}$ is a set of nuclear coordinates, $\mathbf{r} = \{\mathbf{r}_i\}$ is a set of electronic coordinates, Z_I and M_I are respectively the nuclear charges and masses, m is the electronic mass. After solving the Schrödinger equation for the total wave function $\Psi(\mathbf{R}, \mathbf{r})$, everything is known about the system.

Considering that nuclei are much heavier and consequently much slower than electrons, we can regard the nuclei as stationary as far as the electronic part is concerned (Born-Oppeneimer approximation) [28]. This means that we can factorise the total wave-function as

$$\Psi(\mathbf{R}, \mathbf{r}) = \sum_n \Theta_n(\mathbf{R})\Phi_n(\mathbf{R}, \mathbf{r}) \tag{2.58}$$

where $\Theta_n(\mathbf{R})$ describes the nuclei and $\Phi_n(\mathbf{R}, \mathbf{r})$ the electrons (depending parametrically on the coordinates of the nuclei). With this assumption, the original problem is solved

in terms of two separate Schrödinger equations:

$$H_{el}\Phi(\mathbf{R}_I, \mathbf{r}_i) = V(\mathbf{R}_i)\Phi(\mathbf{R}_I, \mathbf{r}_i) \tag{2.59}$$

where

$$H_{el} = \sum_i \frac{p_i^2}{2m} + \frac{e^2}{2}\sum_i \sum_{j\neq i} \frac{1}{|\mathbf{r}_i - \mathbf{r}_j|} - e^2 \sum_I \sum_i \frac{Z_I}{|\mathbf{R}_I - \mathbf{r}_i|} \tag{2.60}$$

and

$$\Big[\sum_I \frac{P_I^2}{2M_I} + V(\mathbf{R}_i)\Big]\Theta(\mathbf{R}_I) = E\Theta(\mathbf{R}_I). \tag{2.61}$$

Equation 2.59 is for the electronic problem, under the assumption that the nuclei are fixed (a popular method to solve this equation will be introduced in Sec. 2.4.2.1). The eigenvalue of the electronic energy $V(\mathbf{R}_i)$ will depend parametrically on the coordinates of the nuclei; this quantity is called the *interatomic potential*. Once found, this quantity enters equation 2.61, which will give the motion of the nuclei.

In the field of molecular dynamics it is customary to replace this Schrödinger equation with a Newtonian equation, modelling the motion of the nuclei classically:

$$H = T(\{p_i\}) + V(\{r_i\}), \tag{2.62}$$

where $T = \sum_i p^2/2m_i$ is the kinetic energy of a system of N particles and V its potential energy. Nevertheless, solving equation 2.59 to find the electronic energy $V(\mathbf{R}_i)$ constitutes a formidable task. Depending on the way we achieve this, different molecular dynamics approaches are available, each of which confers advantages and disadvantages.

A full quantum treatment of the electronic energy characterises the so called *first-principles molecular dynamics* [29], where, adopting approximations, we really solve the electronic Schrödinger equation. Whilst this is feasible, it requires huge computational resources and poses severe limits on the maximum size of the system and on the simulation time. On the other hand, by completely removing the electronic degrees of freedom, we define the traditional approach of molecular dynamics, with which we simulate the motion of a system of classical particles using Newton's Laws of Motion. In this case we select functional forms of $V(\mathbf{R}_i)$ which mimic the behaviour of the true potential in realistic ways for specific materials. This approach is particularly useful to study complex systems of millions of atoms, and for simulation times ranging from a few picoseconds to hundreds of nanoseconds.

In-between these approaches there exists a new class of hybrid schemes which link

quantum mechanical and classical modelling. The deep insight of this method is that one can span large scale simulations using a classical model to describe with reasonable accuracy the topology of bonding, and a quantum mechanical model in one specific zone of the system in which solving the Schrödinger equation for the electrons becomes decisive. In general, quantum approaches applied to solid systems assume valid, since the beginning, the Born-Oppeneimer approximation: hence the label "ab initio" given to these methods.

2.4.2.1 Density Functional Theory

Density Functional Theory (DFT) is an ab initio quantum mechanical method used to describe the electronic structure of solid state physical systems. In 1964, Hohenberg and Kohn stated two fundamental theorems in an attempt to simplify the solution of the many-body electronic problem expressed via the Schrödinger equation 2.59. [30] The first theorem proves that the ground state energy E of an electron gas in an external potential V_{ext} is a unique and universal functional of the electron density $n(\mathbf{r})$:

$$E[n(\mathbf{r})] = F[n(\mathbf{r})] + \int V_{ext}(\mathbf{r})n(\mathbf{r})d^3\mathbf{r}, \tag{2.63}$$

where $F[n(\mathbf{r})]$ is the density functional including the electron-electron interaction and the kinetic interaction of the electronic Hamiltonian in Eq. 2.60. The second theorem demonstrates that the universal energy functional is minimised through the variational principle by the ground state electron density $n_0(\mathbf{r})$. Thus the minimum of the total energy yields $n(\mathbf{r})$: from this ground state electron density all other observables can be obtained.

In summary, the knowledge of N wave-functions with $3N$ spatial coordinates representing the electrons is reduced to the equivalent problem of calculating an electron density $n(\mathbf{r})$ with 3 spatial coordinates. However, the many-body problem included in the universal density functional $F[n(\mathbf{r})]$ still represents a formidable computational task.

Kohn and Sham in 1965 simplified this problem by considering an auxiliary system of non interacting electrons in an external effective potential that simulate the effect of many-body interaction: [31]

$$E_{KS}[n(\mathbf{r})] = T[n(\mathbf{r})] + V_{KS}[n(\mathbf{r})], \tag{2.64}$$

where E_{KS} represents the universal energy functional, T is the kinetic energy operator

and V_{KS} is the effective potential in which the non interacting electrons are moving.

The main assumption of Kohn-Sham approach is that the charge density n of the real interacting system equals the one of the non interacting reference system n_r:

$$n(\mathbf{r}) = n_r(\mathbf{r}) = \sum_{i=1}^{N} |\phi_i|^2 \tag{2.65}$$

where $|\phi_i >$ are the non interacting single particle wave functions, known as Kohn-Sham orbitals. Therefore, the electron density of the original interacting system can be obtained by solving the Kohn-Sham equations of the auxiliary non interacting system:

$$[T + V_{KS}]|\phi >= \epsilon_i|\phi > . \tag{2.66}$$

The effective potential V_{KS} contains all the information related to the many-body interacting system, by explicating the electron-electron interaction term into pieces of decreasing importance from the energetic point of view:

$$V_{KS} = \frac{1}{2}\iint \frac{n_r(\mathbf{r})n_r(\mathbf{r}')}{|\mathbf{r} - \mathbf{r}'|}\mathrm{d}\mathbf{r}\mathrm{d}\mathbf{r}' + V_{XC}[n_r(\mathbf{r})]. \tag{2.67}$$

The first term, known also as Hartree term, is the classical electrostatic energy and accounts for the largest contribution of the electron-electron interaction. The exchange term (accounting for the short range repulsion of two electrons with parallel spin occupying the same position) and the correlation term (describing the more general correlation between the position of electrons due to their long range Coulomb repulsion) are fused together in V_{XC}.

Within the DFT framework, this quantity can only be approximated, either as a local functional of the density in the Local Density Approximation (LDA), or of the density and its gradient in the Generalised Gradient Approximation (GGA). Plane waves are generally chosen as the basis set for the Kohn-Sham wavefunctions in Eq. 2.66 in order to describe periodic systems:

$$\phi_{i,\mathbf{k}}(\mathbf{r}) = e^{i\mathbf{k}\cdot\mathbf{r}}u_i(\mathbf{r}), \tag{2.68}$$

with u_i representing the periodic Bloch function. A further approximation to the all-electron potential in Eq. 2.66 is possible by considering only the valence electron wavefunctions via a substitution of the combined effect of the nucleus and the core electrons with a pseudopotential, which can be norm-conserving [32] or ultrasoft [33].

Finally, the self-consistent (iterative) solution of the Kohn-Sham equations in Eq. 2.66 yields the ground state electron density $n(\mathbf{r})$ and consequently the ground state total energy E_{KS}. From the ground state energy, all the forces can be calculated, and therefore used to carry out molecular dynamics or geometry optimisation using the ab initio method. According to the Hellmann-Feynman theorem [34], the force on the Ith nucleus at position $\mathbf{R}_I$ is given by:

$$\mathbf{F}_I = \frac{\partial E_{KS}}{\partial \mathbf{R}_I}. \tag{2.69}$$

The knowledge of the quantum forces acting on specific atoms of the cohesive zone can reproduce with impressive accuracy all the mechanisms which escape from the realm of classical physics. In the next section we will review a technique which combine classical and quantum forces to create a multi-scale hybrid model of the fracture: the "Learn on The Fly" technique.

2.5 The "Learn on The Fly" technique

2.5.1 Multi-scale modelling

Fracture is a strongly coupled multi-scale problem. Straining a perfectly elastic material, without defects or polar charges, determines a long range elastic interaction wholly predictable by means of Elasticity Theory (see Sec. 2.2.1). However, straining the same material, elastic, but with an atomically sharp crack within its body, modifies dramatically its elastic properties (see Sec. 2.2.2). The stress field behaves elastically in the universal elastic region far from the tip, whilst increases in the near tip region as predicted by LEFM (see Fig. 2.9). At the crack tip, the elementary crack advancement is described by a bond breaking event, which involves a significant change of the electronic structure of the broken bonds and their neighbourhood. Thus, bond breaking, or chemical reactions occurring at the crack tip, can be only interpreted correctly by Quantum Mechanics.

On the basis of these facts, understanding brittle fracture at the atomic level requires a virtuous matching of the classical and quantum mechanical descriptions of matter. In particular, we will focus on hybrid techniques that combine two atomistic treatments: one using MM interatomic potentials (see Sec. 2.4.1.1) and one by means of quantum mechanical methods (see Sec. 2.4.2.1), known indeed as QM/MM (Quantum Mechanical/Molecular Mechanical) approaches. Two broad categories of QM/MM hybrid schemes can be defined: energy mixing and force mixing. On the one hand, the

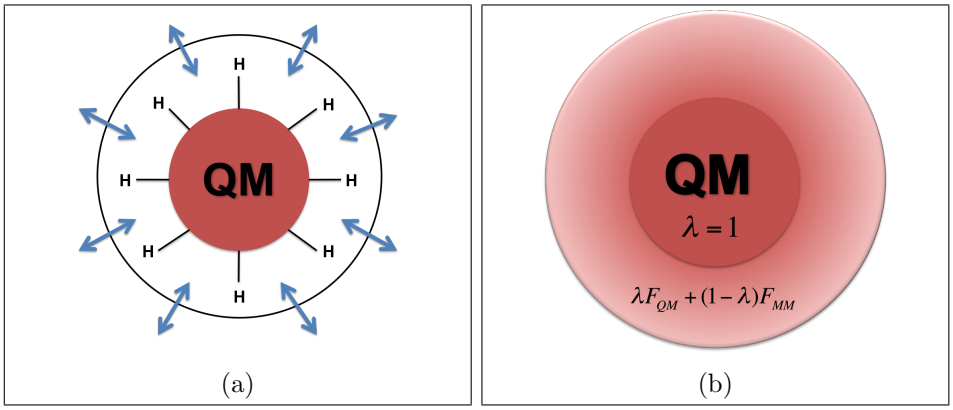

Figure 2.11: Hybrid modelling coupling methods: (a) The energy mixing method; (b) The smooth force mixing method. Red and white fields denote respectively the QM and MM regions.

energy mixing methods are based on a unique Hamiltonian where the QM and MM energies are computed separately in their respective region and then combined together, conserving the total energy. On the other hand, force mixing methods are centred on the forces rather than on the energies: QM forces are computed in the QM region, MM forces in the MM region, and then an interpolation between the two is performed in a transition buffer region. A schematic diagram of these two broad categories is shown in Fig. 2.11.

The energy mixing method (Fig. 2.11a on the left) identifies the QM active region (red sphere) and the MM region (white field), where the respective energies are separately calculated. The QM boundary is passivated with some atom (hydrogen passivation is quite common) or by means of pseudo-orbitals (via modified pseudo-potentials which simulates a frozen orbital). The double arrows symbolise the QM/MM coupling, which produces a corrective interaction energy term in the computation of the total energy.

The smooth force mixing method (Fig. 2.11b on the right) augments the QM active region (red sphere) with a buffer region (annular region with radial red gradient) where a weighted sum of QM and MM forces are used. The weight λ is represented by a gradient colour, linearly interpolating the forces from 1 (red) to 0 (white). The main advantage of this scheme is the fact that there is no need to passivate the QM region. Since forces are calculated on each atom, there is no interaction term as in energy mixing methods. However, since forces no longer come from a single Hamiltonian, neither energy nor momentum are conserved. In the next section we will show how

LOTF deals with this problem.

The earliest QM/MM study was performed in 1976 by Warshel and Levitt [1] to model enzymic reactions. [35] The authors understood the importance of studying the system enzyme-substrate as a whole, by splitting the problem in three contributes: quantum, classical and the interaction between them. The atoms directly involved in the lysozyme reaction are treated at the quantum level, whilst the potential energy surface of the substrate and the solvent is well described by empirical potential functions. The coupling between the quantum and the classical potential was described by a microscopic model in order to correct the inductive effect of bare Coulomb classical charges on the QM atoms at the active site. Moreover, the QM atoms at the boundary were passivated with a single hybrid orbital, describing classically the covalent bond with MM atoms instead. This brilliant pioneering work contains all the main ingredients of modern QM/MM techniques, and since then hybrid simulations flourished in the biochemistry community.

The earliest hybrid simulation applied to solid state systems was performed in 1993 by Spence et al. [36] to study lattice trapping and surface reconstruction on silicon. In this case the authors used a force-mixing embedding scheme to describe the coupling between QM and MM forces. On the contrary, energy-mixing methods were used by Ogata in Ref. [37] to study the environmental effects of H_2O on fracture initiation in silicon. It is clear that the choice of the specific hybrid method strictly depends on the particular mechanisms under investigation. Nevertheless, the class of force mixing methods are the most used for multi-scale studies on solid state systems. A good review on hybrid atomistic simulation for solid state systems can be found in Ref. [38].

The hybrid method used in this work, which belongs to the class of force mixing schemes, is called the "Learn On The Fly" (LOTF) technique. The philosophy behind this approach was firstly introduced in 1998 by De Vita and Car [39], and then developed as a hybrid QM/MM method in 2004. [40] Further developments of the LOTF algorithm were embedded in LIBATOMS [41, 42, 43], a molecular dynamics library written in Fortran 95+ and recently expanded with a powerful Python interface [44]. The main breakthrough behind this method is the effectiveness in combining QM and MM forces both in space and time, requiring a quantum accuracy only wherever and whenever needed by the problem under investigation. In the next subsections, the main ingredients of the LOTF method will be presented, particularly stressing its application to the fracture problem.

[1] Warshel, Levitt and Karplus were recently awarded of the 2013 Nobel Prize in Chemistry for their contribute towards multi-scale modelling of complex chemical systems.

2.5.2 Coupling QM and MM

The hybrid technique aims to reproduce observables with the same accuracy of quantum mechanics, still holding a competitive computational cost. The challenge is hard, considering that almost all the computational cost depends on the number of atoms selected to be studied at the quantum level. In fracture problems, the atoms located at the crack tip (namely the process zone defined in Fig. 2.9, Sec. 2.3), where bond breaking or chemical processes drive the crack dynamics, are naturally selected as "QM active". Moreover, atoms nearby the process zone are also treated at the QM level by forming a buffer region, which is the one that constitutes the real boundary with the MM region.

This fictitious interaction at the boundary has no particular consequences on the active site, provided that the strong locality holds:

$$\frac{\partial^n}{\partial \mathbf{x}_j^n}\frac{\partial E}{\partial \mathbf{x}_i} \rightarrow 0 \ |\mathbf{x}_i - \mathbf{x}_j| \ \rightarrow \infty \ \forall \ \mathrm{n}, \ i \neq j \tag{2.70}$$

where E is the total energy, x_i and x_j are atomic positions of atoms i and j. The strong locality guarantees that trajectories calculated at the active site (centre of QM region) are not affected by classical trajectories in the MM region. The total number of QM atoms (active and buffer) is the first, and most important control parameter, with respect to which all macroscopic observables should be converged. This number can be practically determined by using topological criteria, for example by tuning parameters as the radius of a sphere centred on the active region.

Once the QM/MM boundary is defined, another problem one has to deal with is how to update the QM selection algorithm if atoms fluctuate across this boundary. Excepted the singular situation in which the QM region can be kept fixed (typical in static calculation where the crack dynamics is not important), fracture studies need to track the movement of the crack front during the simulation. In this common general case, atoms fluctuations may lead to sudden changes of the number of atoms selected to be treated at the QM level. To mitigate this problem, the proximity analysis must be performed on time-averaged positions of the atoms rather than on their instantaneous positions:

$$\bar{\mathbf{x}}(t) = \left(1 - e^{-\frac{\Delta t}{\tau}}\right) \sum_{n=0}^{\infty} e^{-\frac{n\Delta t}{\tau}} \mathbf{x}(t - n\Delta t) \tag{2.71}$$

where Δt is the time step of the simulation and $\bar{\mathbf{x}}$ the averaged position which filter out the real positions $\mathbf{x}$ with a timescale shorter than τ.

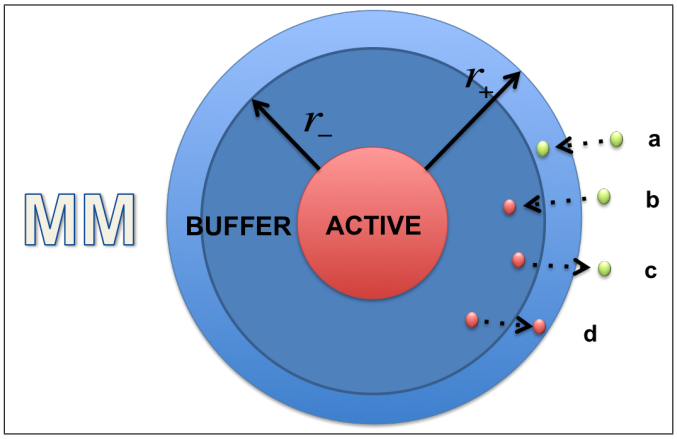

Figure 2.12: The hysteretic QM selection algorithm is schematically shown for four cases, with QM and MM atoms coloured respectively in red and green. a) MM atom entering external ring stays MM; b) MM atom entering internal ring becomes QM; QM atom exiting external ring becomes MM; QM atom exiting internal ring and entering external ring stays QM.

This fluctuation problem can be attacked also by choosing a QM selection algorithm based on bond-hopping, where the boundary is not longer determined by a simple Euclidean distance but rather by a covalently bonded unit. Moreover, the selection and deselection process of an atom as QM active can be strengthened by adding a more stringent condition at the boundary. This is the principle of the hysteretic QM selection algorithm, implemented by Kermode in Ref. [42] and schematically shown in Fig. 2.12.

The QM buffer surrounding the QM active region (coloured in red) is divided in two layers, with annular radius r_- and $r_+ - r_-$ for the internal (dark blue) and external (light blue) layers respectively. The "hysteresis" in the QM selection process consists in requiring more restrictive conditions according to the previous history of the atoms. For example, a QM atom to be deselected must be further than r_+ from the active region, whilst an MM atom is required to be within a distance of r_- to be selected to QM treatment. Therefore, changes in the QM set occur only for permanent topological changes in the atomic configuration.

Amongst all methods to treat the QM/MM boundary within a force mixing scheme, LOTF adopts the finite buffer method firstly introduced by Bernstein [45] and successfully applied to silicon fracture [46]. In this method, the QM forces calculated on the buffer atoms are not linearly interpolated with MM forces (on the same fashion

of smooth force mixing described in Fig. 2.11). On the contrary, all QM forces are calculated by using a Green's-function-based total-energy method [45], which does not require the artificial termination of dangling bonds. Moreover, the QM buffer forces are not included in the dynamics, but substituted with MM forces instead.

Based upon the technicalities we have reviewed in this section, LOTF introduces a new idea of dealing with the boundary problem. This idea is based on "learning" first, then "adjusting" on the fly, updating in time the new environment explored by a moving crack front.

2.5.3 Learning from the atoms: the LOTF adjustable model

Following the idea of a finite buffer scheme outlined in Bernstein's method, LOTF scheme approaches multi-scale modelling in three steps:

1. Step 1: Computing. Calculation of forces on each atom within a finite buffer scheme (see Fig. 2.13).

2. Step 2: Fitting. Feed a universal Hamiltonian with the correct forces (calculated in step 1) and optimise its parameters.

3. Step 3: Adjusting on the fly. Carry out molecular dynamics simulation with the LOTF forces produced by the universal Hamiltonian by using a predictor-corrector scheme.

Step 1: Computing

Firstly, the region of atoms around the active site is augmented by a double-layered buffer (allowing a hysteric QM selection in time described in Fig. 2.12). This QM cluster is then terminated with hydrogen atoms to passivate missing covalent bonds at the QM/MM boundary (light blue/white). In a first stage, using this finite buffer scheme, QM forces are calculated in the QM cluster and MM forces in the MM region. In a second stage, MM forces are separately calculated on the whole system, regardless of any QM region. Finally, the two stages above are combined by keeping only the QM forces (from the first stage) on the active region and MM forces (from the second stage) anywhere else.

Summarising, at step 1, the LOTF finite buffer scheme yields a complete set of forces ($QM \cup MM$) on all atoms of the system with a desirable accuracy. These forces are ready to be used in the following step.

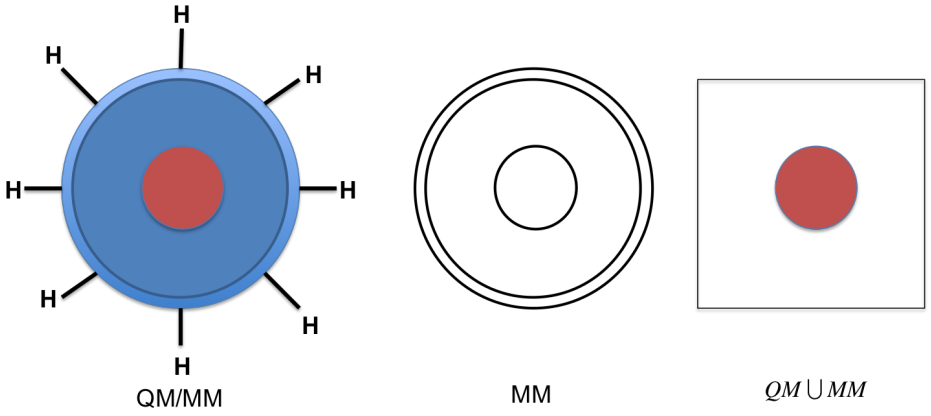

Figure 2.13: Calculation of forces within the LOTF finite buffer scheme. On the left: QM forces are calculated on the QM cluster, composed by the active QM region (red) and a double-layered (to allow hysteric selection) QM buffer (dark and light blue), whilst MM forces are computed on the MM region (white field). On the centre: calculation of MM forces on the whole system. On the right: the final set of accurate forces (QM on the red active region, MM anywhere else in the white field).

Step 2: Fitting

Instead of mixing in space two different Hamiltonians produced from the set of forces in step 1, the same set is used to feed, in time, a universal classical Hamiltonian describing the whole system. The universal Hamiltonian should be simple and flexible, in the sense that its parameters can vary in space (each atom may be characterised by different parameters) and in time (the parameters can be updated during the simulation accordingly).

The universal LOTF Hamiltonian consists of an "adjustable model" in addition to the classical model. The simplest version of the adjustable potential assumes the form of a set of linear springs:

$$V_{ADJ}(\alpha, \mathbf{R}) = \sum_{bonds} \alpha_{ij} r_{ij} \tag{2.72}$$

where the system is described by a set of two body springs linear in the interatomic distance r_{ij}.

The motivation to use this functional form is twofold. Firstly, bond lengths represent coordinates that move more slowly than the atomic coordinates themselves. Secondly, the linearity of the potential gives rise to a linear relation in the forces as

well:

$$\mathbf{F}_{ADJ} = C\alpha, \tag{2.73}$$

where C is a matrix of size $N_{param} \times 3N_{fit}$ that only depends on the atomic positions.

The singular value decomposition (SVD) of the matrix C can be used to find the least squares solution for the parameters α:

$$\min|\mathbf{F}_{target} - C\alpha|^2, \tag{2.74}$$

where F_{target} is the target force differences at which F_{ADJ} should tend.

Summarising, the main task accomplished by the adjustable model is tuning the spring constants α to reproduce correct forces on all the atoms and therefore minimising the functional:

$$\mathcal{F} = \sum_{allatoms} |(\mathbf{F}_{QM} - \mathbf{F}_{CL}) - \mathbf{F}_{ADJ}|^2, \tag{2.75}$$

where $\mathbf{F}_{QM}$ is the quantum mechanical force on an atom, $\mathbf{F}_{CL}$ the classical force and $\mathbf{F}_{ADJ}$ the force from the simple adjustable model. When a good fit can be obtained, the result of the optimisation is that:

$$\mathbf{F}_{QM-MM} \simeq \mathbf{F}_{MM} + \mathbf{F}_{ADJ}, \tag{2.76}$$

where $\mathbf{F}_{QM-MM}$ is the set of accurate forces calculated at Step 1.

The universal LOTF Hamiltonian is then expressed by:

$$V_{LOTF}(\mathbf{R}, \alpha) = V_{MM}(\mathbf{R}) + V_{ADJ}(\mathbf{R}, \alpha) \tag{2.77}$$

and its gradient produces the LOTF forces

$$\mathbf{F}_{LOTF}(\mathbf{R}, \alpha) = -\nabla V_{LOTF} = \mathbf{F}_{MM} + \mathbf{F}_{ADJ} \tag{2.78}$$

with which molecular dynamics is carried out.

Forces in Eq. 2.78 derive from a single total energy function in Eq. 2.77 (derived in turn from the teaching process of the original forces calculated in step 1). This fact removes the mechanical inconsistencies at the QM/MM boundary that rise from using typical force-mixing methods.

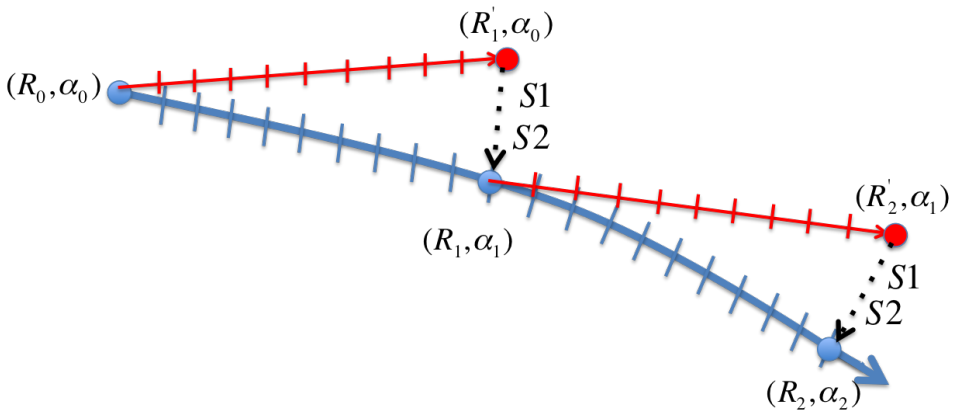

Figure 2.14: The predictor-corrector scheme. The thick blue line indicate the MD trajectory. Starting from the initial set $(\mathbf{R}_0, \alpha_0)$, the thin red line explores the phase space for N extrapolation steps, where MD is carried out keeping α_0 constant until the virtual point in phase space $(\mathbf{R}_1^{'}, \alpha_0)$. At this point, S1 (Step 1) and S2 (Step 2) are performed in sequence to give the new set of parameters $(\mathbf{R}_1, \alpha_1)$. The thick blue line represents the true MD trajectory, carried out by interpolating between α_0 and α_1.

Step 3: Adjusting on the fly

Molecular dynamics can be carried out using forces in Eq. 2.78. If the deviation of QM and MM potential energy surfaces is not too large, teaching (step 2) and learning (step 1) processes do not have to be carried out at every time step. The same set of LOTF parameters can be used for few MD steps, and only then it can be updated by performing in sequence learning and teaching processes. This procedure is schematically presented in Fig. 2.14.

At the beginning, once the QM region is defined, step 1 and step 2 are performed in sequence to give rise to the initial set of LOTF parameters $(\mathbf{R}_0, \alpha_0)$. Then, a primary LOTF MD is carried out for N extrapolation steps keeping the adjustable potential parameters α_0 constant. This trajectory ends in a point of the phase space indicated by $(\mathbf{R}_1^{'}, \alpha_0)$, where $\mathbf{R}_1^{'}$ points out a set of virtual atomic positions. At this point, new forces are calculated (Step 1) and a new set of LOTF parameters is obtained (Step 2), identifying a new point in phase space $(\mathbf{R}_1, \alpha_1)$. Now, the true LOTF MD is carried out for the same number of steps N, interpolating the adjustable potential between α_0 and α_1.

The LOTF predictor-corrector scheme is iteratively repeated for the whole simulation. Following this procedure, the active region is constantly mapped in space and

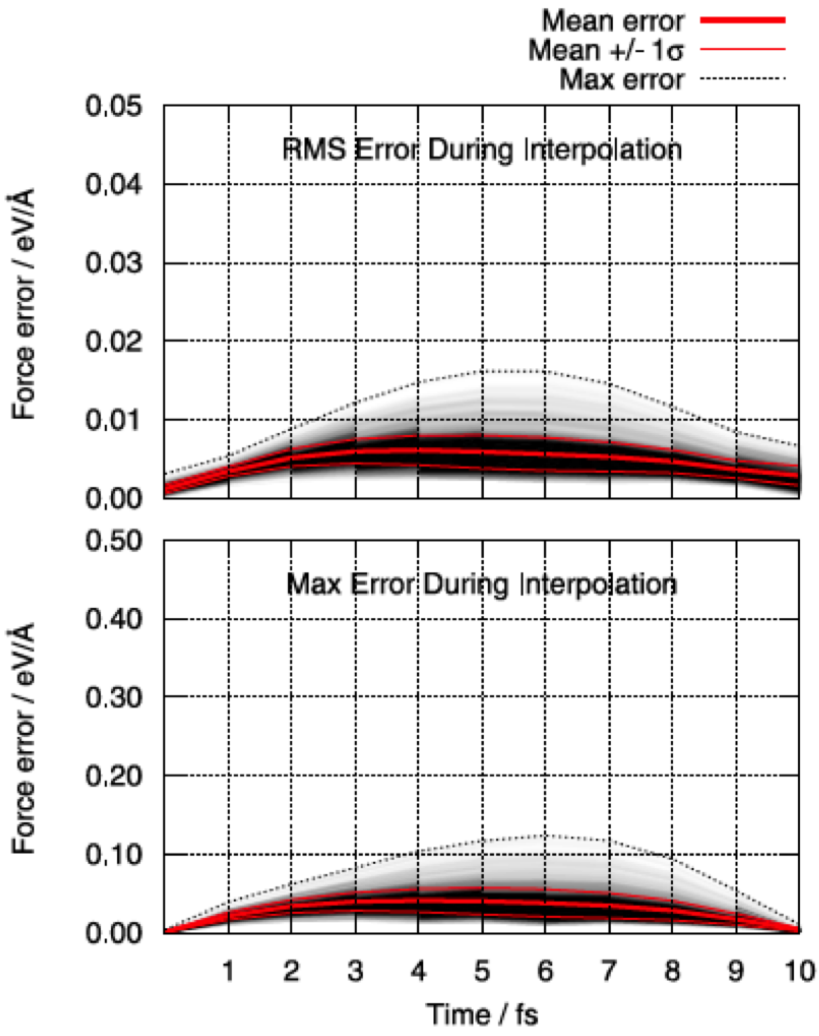

Figure 2.15: LOTF force errors. Force errors during a single LOTF cycle, averaged over many trajectories. Reproduced from Ref. [38].

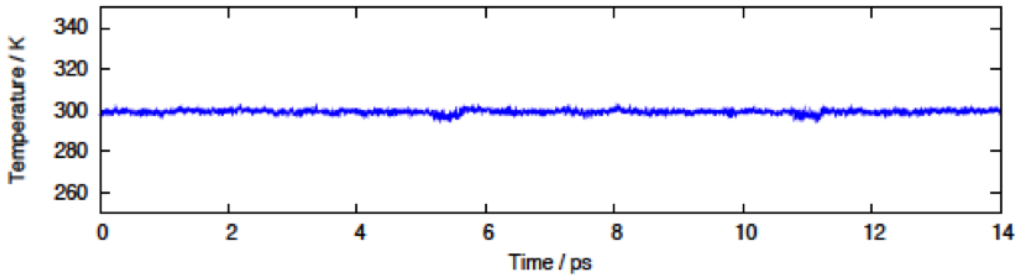

Figure 2.16: Temperature evolution during a LOTF hybrid simulation of silicon fracture. A week Langevin thermostat is used to adsorb the energy drift caused by the time-independent Hamiltonian. Reproduced from Ref. [42].

time at the QM accuracy, yet reducing by N times the computational cost. Prior applying the LOTF scheme, accurate force error tests must be done in order to define the maximum number of extrapolation-interpolation steps, (N):

$$F_{error} = F_{QM-MM} - F_{LOTF}, \tag{2.79}$$

where the computation of the two set of forces, F_{QM-MM} and F_{LOTF}, is carried out at every time step.

The choice of the parameter N relies on how closely the LOTF potential, and by extension the adjustable model, is able to capture the physics of the whole system by fixing its parameters. If the processes happening at the active site are completely beyond the capacity of the MM model, then the LOTF forces with fixed parameters may deviate substantially from the set F_{QM-MM} calculated at step 1. Therefore, in this case, the adjustable parameters α need to be calculated at every time step of the MD simulation. In Fig. 2.15 are reported LOTF force errors for a test system of 64 atoms silicon bulk at a temperature of 2000 K with a QM region of 5 atoms at the centre of the bulk.

Another important preliminary test of QM/MM force-mixing hybrid schemes deals with the conservation of the energy. Since LOTF scheme is force based, with a defined Hamiltonian which varies in space and time, the energy is not conserved. Thermostats can be used to correct the energy drift by adding extra heat to the system. Within the LOTF scheme, Langevin thermostat [24] is used for this purpose.

Once the system is thermostatted, a sensitive quantity capable to detect possible anomalies of the model is the temperature deviation computed in the QM region from

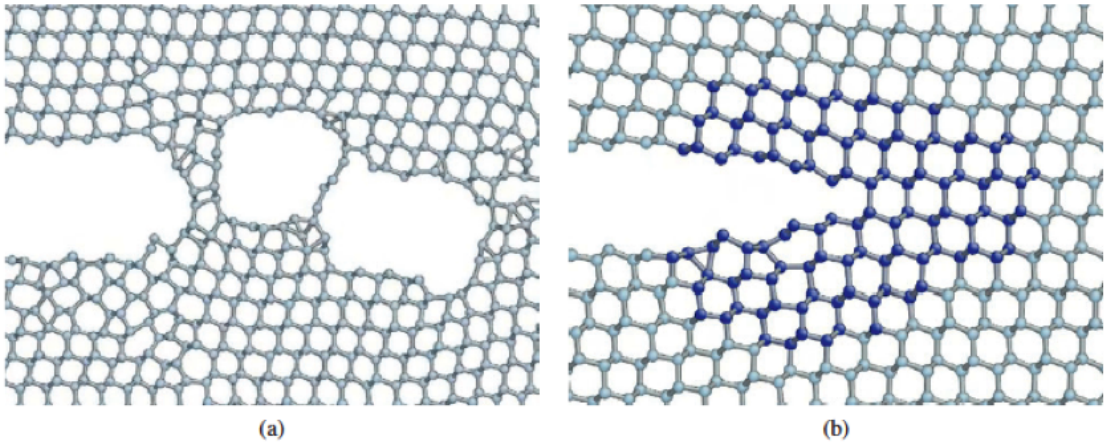

Figure 2.17: Snapshots from MD simulations of fracture in silicon on the (111) cleavage plane, with (a) the SW classical interatomic potential and (b) the LOTF scheme, with dark blue atoms treated at the QM level (DFT) and grey atoms with the same classical potential as in panel (a). The classical simulation is unphysically ductile, while the LOTF simulation recovers the brittle material response, as well as correctly capturing chemical details such as the Pandey 2×1 reconstruction on the (111) surface. Reproduced from Ref. [47].

the target thermostat temperature. In Fig. 2.16 we report the temperature evolution during a LOTF hybrid simulation of silicon fracture. We see that by using a weak Langevin thermostat the temperature is constant during the whole simulation. The NVT ensemble obtained approaches the micro-canonical ensemble for very large systems. Other accurate tests on the LOTF temperature deviation and comparison with other force-mixing schemes can be found in Ref. [38].

To date, the LOTF scheme has been successfully applied to several aspects of brittle fracture in silicon, ranging from stress corrosion mechanisms induced by hydrogen [48] and oxygen [47] to scattering of crack initiated by impurity atoms [49], by a screw dislocation [50], by surface reconstruction processes [51, 52]. All the results presented in these works have been confirmed through experimental observations of fracture at the atomic scale. A description of experimental techniques used to observe fracture features at the nanoscale will be presented in the next section.

2.6 Fracture experiments

The challenges offered by the fracture problem to the scientific community are numerous. One of them, however, has obtained a particular light in recent years. The challenge of merging in a virtuous synergy the "hardware" of the experiment with the "software" of the simulation. This metaphor has become an unavoidable practice in most of the scientific studies, especially when the discrete nature of the matter can not be neglected.

Understanding fracture at the atomic scale, and therefore aiming to predict fracture mechanisms through computer simulations, requires a clear picture of real fracture experiments. A typical fracture experiment focuses on measuring observables like crack speed, energy release rate and stress field. At the nanoscale level, qualitative features of the newly opened crack surfaces can be observed.

The aim of this section is to follow the main steps of a typical fracture experiment, from the creation of the seed crack, to loading techniques and crack speed measurements. Experimental methods used to map fracture surfaces at the nanoscale level will be described. Finally, all the ingredients learnt in Chapter 2 will be summarised by typical procedures followed in fracture simulations (Sec. 2.6.2), completing the perfect triangle Theory-Experiment-Simulation.

2.6.1 Observing a real crack

Crack speed as a function of the energy release rate is one of the crucial characteristics in fracture dynamics. A broad range of experimental techniques are therefore based on devices able to control with high accuracy the load applied to the system and the crack length as a function of time. A crucial point of these techniques is also the ability of reproducing experiments directly comparable with theoretical models. A good example of the former was attempted by Hauch and Marder in 1999, where a tensile fracture experiment in silicon was directly compared with a MD simulation. [16] In this outstanding work, the authors illustrate details of the experimental technique used in relation to the thin strip geometry (see Sec. 2.3.1), typical configuration adopted in computational models. In this section, the main steps of this experimental technique will be summarised.

Before any fracture experiment, a crack seed must be inserted in the material body. A thermal shock technique is usually used to achieve this task: the sample is initially notched with a diamond disk, then heated into boiling water and further cooled down into ice. During this process, oxidation, hydrogenation or hydroxylation are likely to

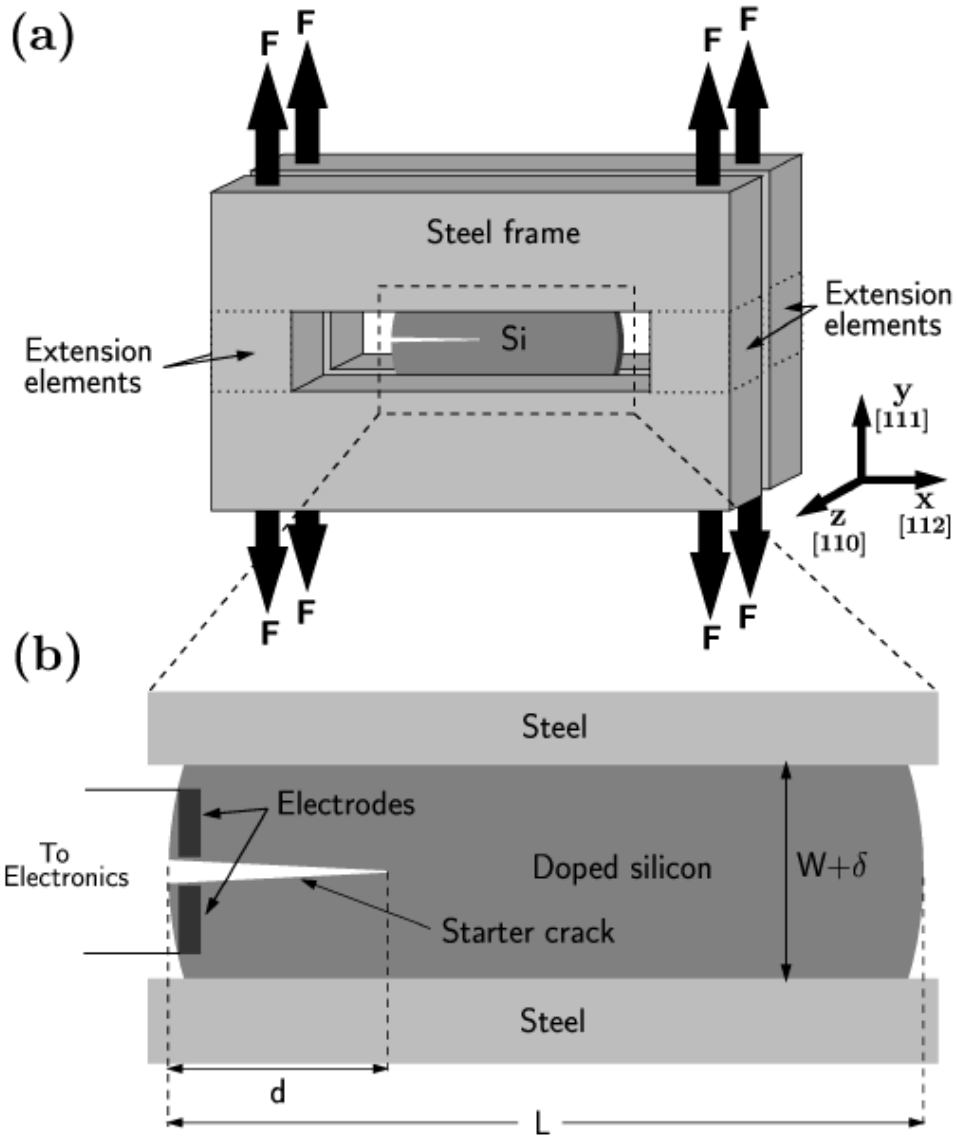

Figure 2.18: Rigid jaw loading configuration. a) Silicon sample embedded in a steel frame where tensile forces are uniformly applied; extension elements strain accordingly, providing a high-precision control of the constant load applied to the sample. b) A thin film of aluminium is deposited on the silicon sample and electrodes placed on the opposite sides of the crack are connected to a Wheatstone bridge; this electric configuration controls the crack length as a function of the resistance of the thin film by following a potential drop method. Reproduced from Ref. [16].

occur inside the notch. The thermal stresses created by this temperature difference locally open up the crack surfaces: the crack advances to the desired length and its tip becomes sharper. The sharpness of the crack tip guarantees a significant stress concentration, and therefore a sensitive control of crack initiation.

The sample with the crack seed is then glued directly to a high-precision loading configuration. In Fig. 2.18 we report a rigid jaw loading configuration used in Ref. [16] to perform constant fracture energy experiments. This loading configuration consists of a steel frame where the fracture sample is placed within its inside hole. The steel jaws are loaded with constant forces that uniformly distribute across the steel frame, causing a small displacement of the extension elements. This enforces in turn a small displacement of the silicon sample glued to the inside edges of the hole.

To track in time the crack advancement, several techniques have been generally used, ranging from high-speed photography to acoustic modulation of the crack tip and potential drop techniques (see Ref. [53] for a review of the subject). The potential drop technique is a popular and efficient method which measures the crack length through changes in the resistance determined by the crack propagation across the conductive specimen. If the specimen is not conductive, a thin film of a conductive element is deposited on the surfaces of the sample across the crack path. [54] When the crack advances, it ruptures also the thin film conductor deposited on it: the variation of its resistance is measured by the potential drop at the electrodes placed on the opposite sides of the fracture line (see Fig. 2.18 b).

Direct observations of surfaces opened by a running crack are generally chosen according to the space scale of interest. Optical microscopes can be used for a preliminary investigation of fracture features, whilst a detailed atomistic investigation can be achieved via Scanning Electron Microscope (SEM) or Atomic Force Microscopy (AFM) devices.

SEM devices focus an electron beam on the fractured surface in high vacuum. Electrons of the beam interact with the atoms at the surface, signals of the interaction are detected and then combined in time with the position of the beam, yielding a 2D high resolution image up to the nanometer scale.

AFM devices consist of a cantilever with a probe, namely a sharp tip (generally silicon or silicon carbide) with radius of curvature of the order of the nanometer. The probe scans the surface, and when brought into the proximity of atoms interacts with them, causing the deflection of the cantilever. The deflection can be measured by piezo-electric devices and is converted into a 3D mapping of the surface, significantly improving the quality respect to SEM devices. Moreover, AFM technique can be used

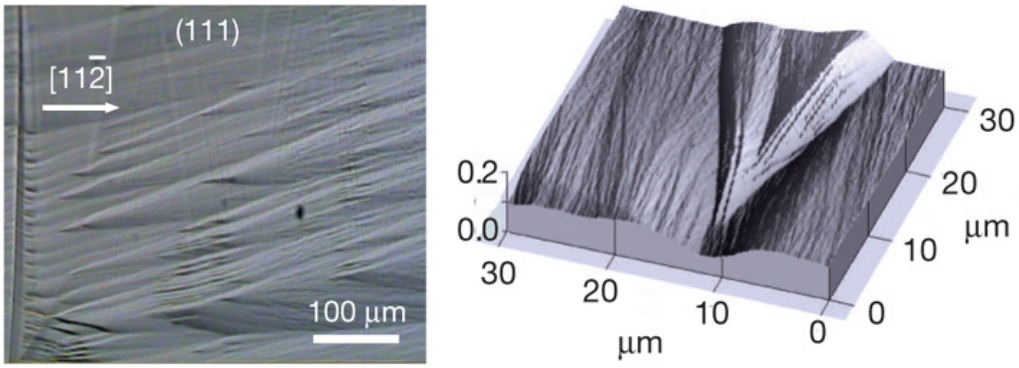

(a) (b)

Figure 2.19: Silicon micrographs. (a) Optical micrograph of the (111) crack system showing the faintly visible Wallner lines; (b) AFM image of a single ridge. Reproduced from Ref. [51].

in a variety of ambient conditions, and does not need ultra-vacuum as in the case of SEM.

An example of direct observations of fracture surfaces in silicon is reported in Fig. 2.19, highlighting the difference between optical and AFM micrographs.

2.6.2 Simulating the experiment

The biggest challenge of computational studies is meeting the thin boundary between the experimental reality and the theoretical model. Nowadays, the increasing power of supercomputers is driving this challenge closer to this target. Although space and time scales of a real fracture experiment are still not achievable by the most expensive computer simulations, there is still room to overcome this natural limit by selecting appropriate boundary conditions of the fracture problem.

The thin strip geometry introduced in Sec. 2.3.1 represents one of this ideal cases: based on this geometry is also the displacement loading scheme shown in Fig. 2.20 and used in this work. This configuration aims to mimic a typical tensile fracture experiments (see Fig. 2.18). Firstly, the crack seed is identified in a thin strip by cutting a series of atomic bonds along a desired crystal plane. Then, an initial loading, correspondent to the desired initial value of energy release rate G_i, is applied by displacing the the fixed top and bottom rows of atoms, allowing the system to relax. Periodic boundary conditions are applied to the the crack front direction, with vacuum surrounding the in-plane edges to allow the loading of the system in the tensile geometry.

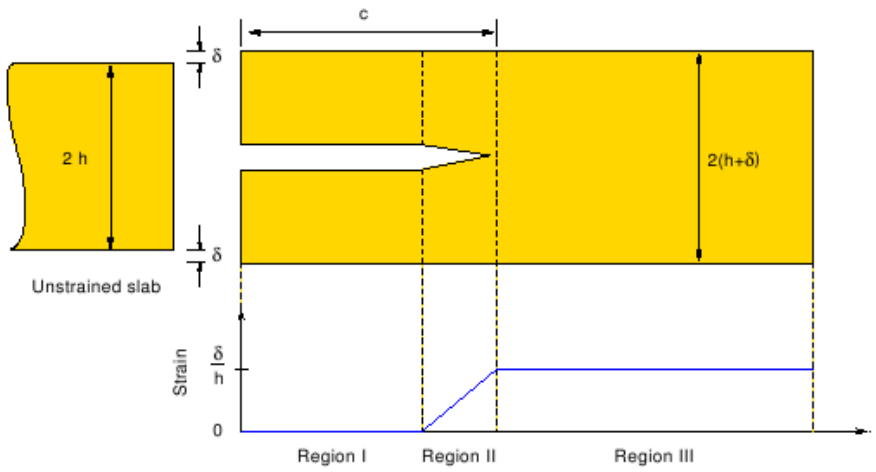

Figure 2.20: Displacement loading scheme. An initial load is applied to an unstrained slab. The atoms in region I are vertically shifted by the displacement δ. In region III the strain is constant and equal to the far field value of δ/h. Across region II the strain increases linearly. Reproduced from Ref. [42].

The crack created in this fashion automatically identifies three regions within the material slab:

1. region I, the crack seed. The atoms along the selected cut bonds result vertically shifted by the displacement δ; the resulting strain in this region is zero.

2. region II, the sharp crack tip. The strain increases smoothly from the strainless situation of region I to the finite value strain of region III.

3. region III, the strained region. The atoms are strained according to the specific loading applied.

Before starting the MD simulation, the initial seed crack needs to be relaxed by performing a geometry optimisation. Classical geometry optimisation generally uses the conjugate gradient algorithm, providing a good approximation of the most accurate QM/MM relaxed geometry. The LOTF hybrid scheme adopts an optimisation algorithm called FIRE (Fast Inertial Relaxation Engine) [55] based on damped MD, by adding a fictitious frictional force to drive the system to the minimum energy. Anytime the loading is smoothly increased, the above structural relaxation is performed accordingly.

Finally, the MD simulation can be performed at the appropriate time step and desired constant temperature by switching on the Langevin thermostat (see Sec. 2.4.1).

The advancement of the crack tip is detected by changes of atom coordination within the process zone, which usually includes few hundred of atoms. Each change of atom coordination corresponds then to a bond breaking event, which in turn implies an advancement of the crack front proportional to the lattice constant of the specific material.

An alternative way to check the crack tip advancement is fitting the time-averaged atomistic stress field to the Irwin near-field solution for a sharp crack (Eq. 2.31 in Sec. 2.2.2.3). The atomistic stress field is calculated for each atom from its deformation relative to the perfect crystal (see details of the method in Ref. [43]). Instead of defining a local stress (for example by means of the virial theorem), the local strain on each atom is considered by comparing the atom's position on the strained crack system to that it would have in the unstrained bulk crystal. By knowing the strain $\hat{\epsilon}$ and the elastic constant matrix $\hat{C}$ of the material under investigation, the atomistic stress $\hat{\sigma}$ can be then computed by using the general equation **??** of linear elasticity theory (see Sec. 2.2.1). An exponential moving average of the obtained stress field is performed in order to mitigate fluctuations due to the random thermal motion of atoms. Finally, to detect the position of the crack during the MD simulation, the atomistic stress field is then fitted to the Irwin near-field solution where the crack tip is a mathematically exact point. The fitting is performed in an annular region extending from 5 Å to 100 Å from the geometrical tip, allowing the position of the centre of the stress field to vary to minimise the difference between atomistic and continuum stress fields.

2.7 Summary

The relevance of the fracture problem has been highlighted in all its aspects, ranging from the basic elements of fracture mechanics (Sec. 2.2) to the most technological experimental and computational techniques nowadays available (Sec. 2.6). In between, theoretical models based on MD simulations have been introduced (Sec. 2.4), and a multi-scale approach has been finally proposed (Sec. 2.5) as an effective tool, able to fully embody relevant atomistic features of fracture mechanisms. In the next chapters, results using these computational tools will be presented, converging, whenever possible, to the evidence of experimental observations.

Chapter 3

Stress corrosion mechanism in silicon by oxygen dissociation

3.1 Introduction

The presence of a topological defect within a material body enhances the stress in its neighbourhood. In Chapter 2 I highlighted the tools necessary to study this phenomenon, focusing on the formation and the dynamic of a crack driven by the applied load. However, most of these defects may appear at the surface of the material: this implies the unavoidable interaction with chemical agents present in the environment. An important aspect of the fracture problem is therefore understanding the effects triggered by chemical reactions occurring in proximity of a crack.

All fracture mechanisms occurring below the critical energy release rate G_c are considered within the realm of static fatigue processes. Stress-corrosion mechanisms play a fundamental role in static fatigue, triggering the genesis of a Griffith critical crack. Small flaws within the material body are stress concentrators, which in turn accelerate the environmental chemical attack.

The theory concerning stress corrosion mechanisms in brittle materials is presented in Sec. 3.2, revising the principal results achieved on the subject. Aiming to interpret recent experiments (Sec. 3.4), I turn to QM/MM simulations (Sec. 3.3) to study the effect of stress corrosion of silicon via the dissociation of oxygen molecules at the crack tip. Finally, in Sec. 3.5 and 3.6, I propose an interpretation of our computational predictions on the light of experimental observations.

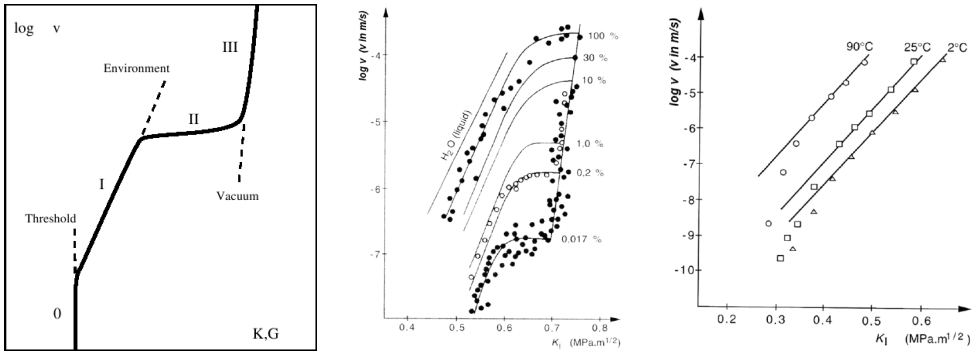

(a) (b) (c)

Figure 3.1: Crack velocity propagation in the stress corrosion regime. (a) General diagram velocity versus loading [56]; (b) Effect of humidity on the crack propagation in soda-lime glass [58]; (c) Effect of temperature in soda-lime glass [59].

3.2 Theoretical background on stress corrosion

When a brittle material is subjected to applied loading for a sufficiently long time, it breaks for a stress lower than the critical stress measured in typical short-time tests. This material weakening caused by long-term stress exposure is called static fatigue. Static fatigue can be regarded as the combination of a primary phase of stress-enhanced corrosion of subcritical flaws with a secondary phase where a stationary crack growth is driven by stress corrosion mechanisms at the crack tip. [56]

The first work dedicated to static fatigue problem in glass was published by Orowan in 1944 [57]. By measuring the surface energy of mica in vacuum and air, Orowan found a ratio of $\sigma_c^{vacuum}/\sigma_c^{air} = 3.5$ between the respective tensile strengths. Since then, it was clear that static fatigue processes were regulated by the finite rate of diffusion of environmental agents into a pre-existent surface crack.

Twenty years later, Wiederhorn produced a clearer picture of stress corrosion mechanisms in glass, by looking particularly at the effect of water and temperature. In Fig. 3.1 is reported velocity versus loading characteristics in the stress corrosion regime. The stress corrosion regime is represented by region I (Fig. 3.1a on the left), where the crack velocity is a strongly increasing function of the energy release rate G or the stress intensity factor K. In this regime, the crack velocity increases linearly for increasing humidity (Fig. 3.1b) [58], and for increasing temperature (Fig. 3.1c) [59].

The dependencies of the crack velocity in the stress-corrosion regime are described

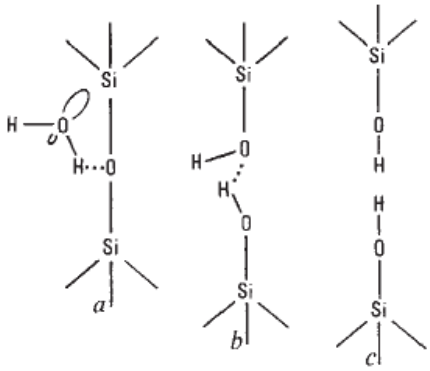

Figure 3.2: Model of reaction between water and a strained Si-O-Si bond at the crack tip. From the left to the right, reaction steps involve: a) adsorption of water to Si-O bond; b) concerted reaction involving simultaneous proton and electron transfer; c) formation of surface hydroxyls. Reproduced from Ref. [60].

by the Wiederhorn equation:

$$v^I = v_0 e^{\alpha K} = A \left(\frac{p_{H_2O}}{p_0} \right)^m e^{\frac{\Delta E_a - bK}{RT}} \tag{3.1}$$

where p_0 is the total atmospheric pressure, p_{H_2O} is the partial pressure of the vapour phase in the atmosphere and R is the gas constant; A, m, ΔE_a and b are adjustable parameters that take into account the dependence of the glass composition; K is the stress intensity factor K_I in the tensile direction.

In 1982 Michalske and Friman extended stress corrosion experiments to several non aqueous environments, proposing a qualitative chemical model for the interaction of the environment with strained bonds at the crack tip. [60] The model consists in a three-steps process reported in Fig. 3.2. Firstly, a water dimer H_20 attaches the Si-O-Si bonds attracted by the high reactivity of the hydrogen with the oxygen at the bridge (O_{br}) together with the oxygen atom of the water with a silicon atom. Then, the concerted reaction between these two couples (proton transfer to the O_{br} from H and electron transfer from O_w to Si) yields two new bonds and breaks the original bridging bonds Si-O. Finally, the rupture of the hydrogen bond between O_w and the transferred hydrogen determines the new fracture surfaces terminated by the Si-O-H group.

The first implication transpiring from this model is that chemical environments similar to water, namely possessing proton donor site at one end of the molecule and lone pair orbitals at the other, are prone to enhance stress corrosion in silica glass. Ex-

periments using gaseous ammonia NH_3 and other structures similar to water confirmed the above thesis.

The model of stress corrosion in glass via water can be obviously extended to other materials and other environmental agents, provided that a certain chemical activity exists between the atomic sites at the stressed bond and the chemical agent. On the one hand, the concerted action of stress and chemistry has been found irrelevant in covalent materials like silicon which do not contain polar bonds. According to Cook [61], silicon specimens loaded in reactive environments like air or water do not exhibit crack extension via stress corrosion.

On the other hand, subcritical crack growth has been detected in silicon as a consequence of static fatigue after cyclic loading. [62] In 2004, the environmental effects of H_2O molecules on Si (110) crack surfaces were investigated by a QM/MM study [37], showing that the water molecule dissociates into H and OH to adhere to the crack surfaces, sometimes oxidising the crack surfaces, and in one case determining a bond breaking of a Si-Si bond. However, adding further water molecules, there was no evidence of crack advancement via a stress-corrosion mechanism induced by water supply at the crack tip.

Silicon can also be cleaved by targeted stress corrosion reactions with implanted hydrogen, as shown in Ref. [48]. In this last work, the effect of hydrogen implanted platelets in silicon has been modelled using a QM/MM approach with LOTF technique. This model showed that the smooth cleavage surfaces observed in the experiments are yielded via a stress corrosion mechanism driven by the formation and following dissociation of H_2 molecule at the stressed crack tip, determining the irreversible bond breaking process.

Experimental evidence of stress corrosion mechanisms can be proved by detecting crack advancement at subcritical values of the applied load. For this purpose, a clear definition of the fracture energy is necessary. Over the past three decades, the debate on the exact values of the fracture energy Γ_0 has not achieved yet a satisfactory convergence towards a unique value. Similar to what has previously been found for Si grain boundaries [63], the scatter of measurements of this observable is still very large, with $3.0 < \Gamma_0^{110} < 5.4$ J/m^2 for the (110) plane [64, 65, 66, 67, 68] and $2.5 < \Gamma_0^{111} < 5.0$ J/m^2 for the (111) plane. Experimental measurements of the relaxed surface energy γ also show a large variation, with $2.8 < \gamma_{expt}^{110} < 3.8$ J/m^2 and $2.3 < \gamma_{expt}^{111} < 5.0$ J/m^2. [69, 70, 71]

From the theoretical level, calculations of relaxed surface energies using density functional theory (DFT) are in reasonable agreement with the direct measurements,

yielding $3.40 < 2\gamma^{110}_{DFT} < 4.08$ J/m^2 and $2.72 < 2\gamma^{111}_{DFT} < 3.97$ J/m^2. [72, 73, 74] The spread of the above DFT calculations depends on the surface reconstruction assumed and the approximation used for the exchange-correlation functional.

In summary, if stress corrosion mechanisms in glass are profoundly documented in literature, only few works have shown a significant role of stress corrosion in silicon. The lack of experimental evidence of environmental effects on silicon have raised a general agreement about the little susceptibility of strongly covalent materials to stress corrosion. However, stress corrosion can never be excluded a priori, for the only reason that the two main ingredients triggering this phenomenon are always present in fracture studies: a highly stressed bond a the crack tip and the surrounding environment.

3.3 Results of QM/MM simulations

Aiming to explain recent measurement of fracture energy reported in a personal communication (see Sec. 3.4), I turned to hybrid simulations to model the interaction of air environment with the silicon crack tip. Air is mainly composed by nitrogen molecules N_2 (∼78%) and oxygen molecules O_2 (∼21%) plus a small amount of other gases (∼1%). Oxygen is a highly reactive element: its electronic configuration [He]$2s^2 2p^4$ yields a high electronegativity, namely a property which strongly favours the acceptance of electrons from donor elements.

What really happens at the crack tip when an oxygen molecule arrives in its proximity? How the oxygen molecule does react with the highly stressed silicon bond? There is nothing better than a computer simulation to visualise how atoms behave in such a model situation. The simulation should be able to describe at the quantum level the likely chemical reaction between the oxygen molecule and silicon atoms at the crack tip, leaving to classical MD potentials the responsibility to model the long range stress field.

In principle, the problem should be modelled considering several aspects of the environmental attack, starting from the mass fluid flow at the crack mouth, to activated diffusion and adsorptive reaction of chemical agent at the crack tip (see Chapter 5 of Ref. [3] for a detailed description of stress corrosion mechanisms in brittle materials). For the sake of simplicity, I focused only on the last part of the problem, modelling the case of an oxygen molecule that comes to be in front of the crack tip. Using the multi-scale modelling tools described in Sec. 2.5, I described the crack tip chemistry by selecting around 200 atoms to be treated at the quantum mechanical level.

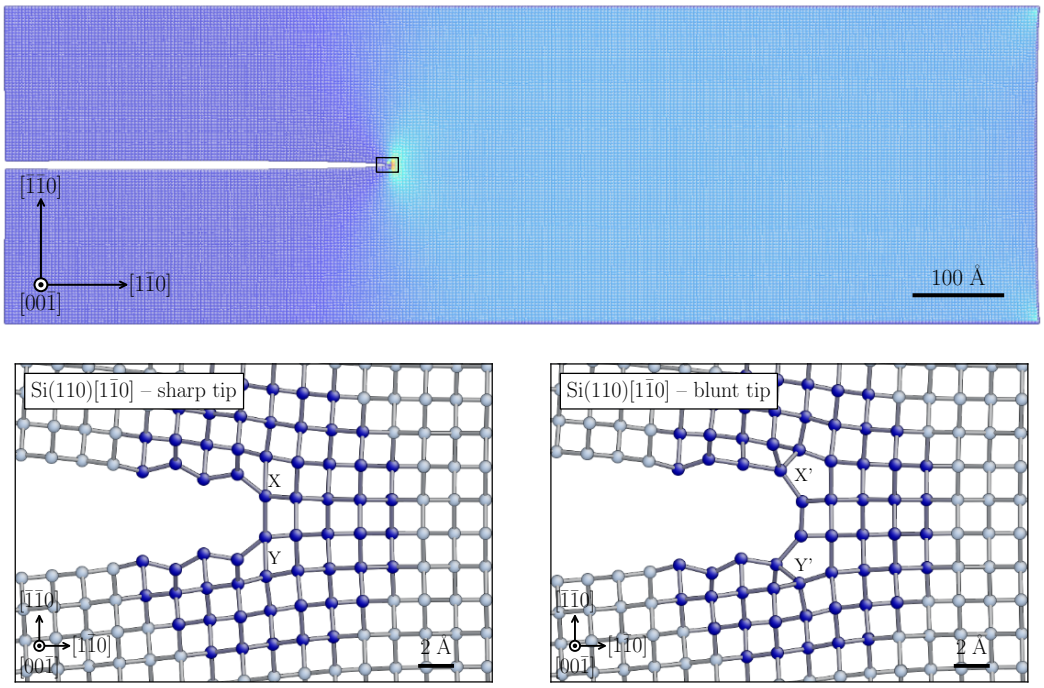

Figure 3.3: Model system of stress corrosion cracking in Si (110)[1$\bar{1}$0] cleavage plane. Atoms are coloured by principal stress, with red corresponding to high tensile stress and dark blue to zero. See text for a complete explanation. [76]

3.3.1 Silicon (110)

The first crack system taken into consideration was the Si (110) cleavage plane in the [1$\bar{1}$0] propagation direction. This cleavage plane offers a greater resistance to crack advancement respect to the Si (111) (see literature review reported in Sec. 3.2). Moreover, propagation along the [1$\bar{1}$0] direction results in nearly perfect flat surfaces. [72]

The simulation methodology is composed by several steps. Firstly, the crack system is prepared in the thin strip geometry described in Section 2.3.1, periodic in the crack front direction and with vacuum surrounding the in-plane edges. A subcritical tensile load equivalent to an energy release rate of $G = 2.7$ J/m^2 was applied, with the top and bottom edges of the model specimen rigidly clamped. [75] The model system has dimensions $1200 \times 400 \times 5.43$ Å^3 and contains 129,794 atoms (Fig. 3.3). This large system is needed to adequately capture the effects of long-range elastic relaxation. [51].

I performed hybrid QM/MM simulations using the Learn on the Fly (LOTF) scheme for a crack, first for the (110)[1$\bar{1}$0] cleavage system. To describe crack tip chemistry

correctly, around 200 atoms near the crack tip were selected for quantum mechanical treatment at the DFT level, using the generalised gradient approximation to the exchange correlation potential [77] as implemented in the VASP [78] and CASTEP [79] codes.

A hybrid QM/MM relaxation of the full crack system was first performed using the FIRE algorithm [55], leading to a novel tip structure with a slightly blunted tip, formed from the sharp tip by two bond rotations (Fig. 3.3 on the bottom). The black rectangle shows the region shown in subsequent panels. Crack tip structures obtained by QM/MM geometry optimisation with sharp crack tip (on the left) and lower energy blunt crack tip (on the right), related to the sharp tip by rotation of bonds X/X and Y/Y. Dark blue atoms are treated at the QM level.

As with the previously reported $5-7$ crack tip reconstruction on the (111) cleavage plane [51], I find that the local chemical cost of the bond rotations is compensated by a reduction in elastic energy. Integrating forces along a pathway linking the two configurations confirms that the blunted tip system is lower in energy by 0.12 eV per unit length along the crack front, suggesting it is the preferred equilibrium crack tip structure. Therefore this configuration has been selected as the starting point for dynamical simulations.

Using LOTF molecular dynamics simulations at a temperature of 300 K, I first confirmed that at $G = 2.7$ J/m^2 the crack neither advances nor closes up, remaining pinned by the lattice trapping barrier [17]. I then placed an oxygen molecule 4 Å behind the first unbroken Si-Si bond at the crack tip (see Fig. 3.4), and continued the molecular dynamics simulation. The chemisorption energy of an O_2 molecule on a silicon surface is known to be of the order of 5 eV [80] with an activation barrier of about $0.2-0.3$ eV per molecule on an unstressed surface [81]. In my simulations, I observe immediate spontaneous dissociation of the oxygen molecule (see Fig. 3.4), indicating that dissociation becomes barrierless under these conditions.

The oxygen atoms are adsorbed to form Si-O-Si bridges behind the crack tip, and the crack advances via cleavage of the Si-Si bond labeled (1) in Fig. 3.4. The simulation was continued by adding a second O_2 molecule, which undergoes a similar pattern of dissociative chemisorption, Si-O-Si bridge formation and crack advance. Further molecules added to the MD trajectory confirmed the general stress corrosion phenomenon outlined in Fig. 3.4, via a barrierless dissociation of oxygen molecules and preferred attack to the Si sites of the stressed crack tip.

To check the sensitivity of our results to initial conditions, several molecule-tip distances were tried. The dissociation barrier as a function of the molecule distance to

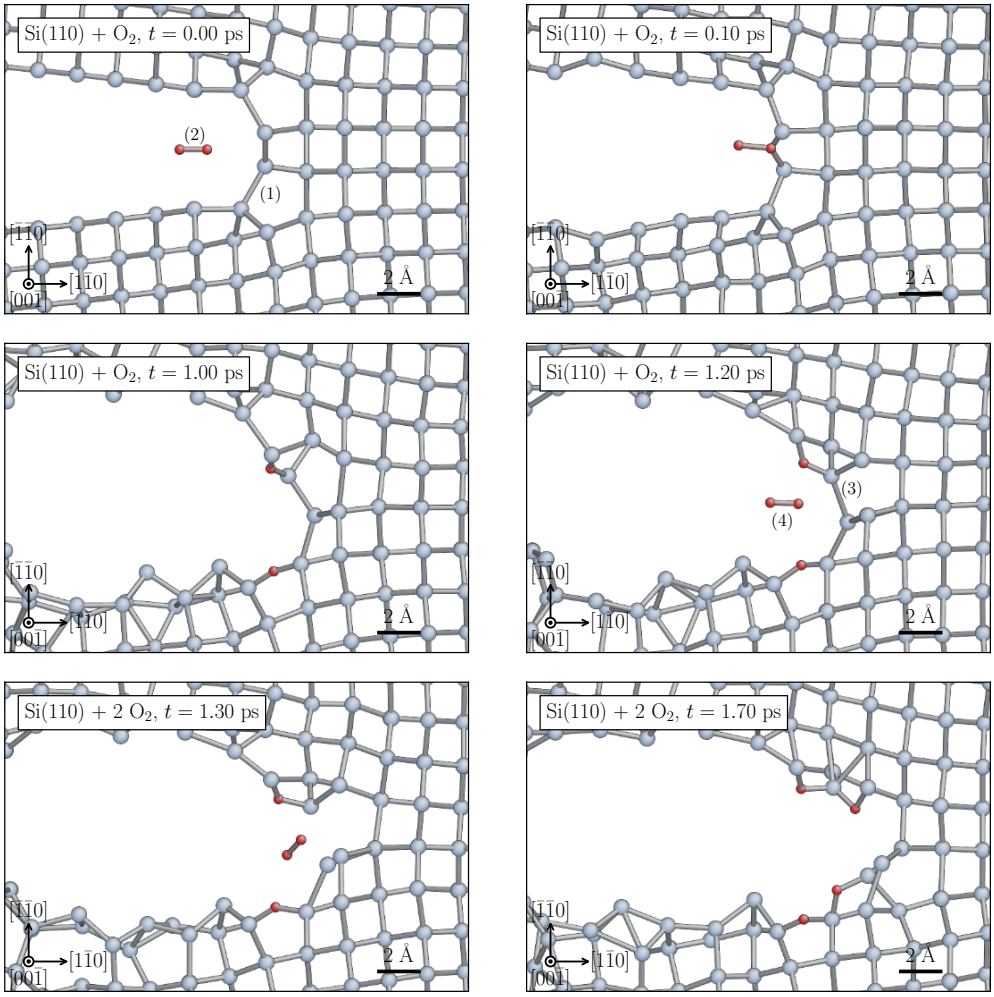

Figure 3.4: Snapshot from QM/MM dynamics showing dissociative chemisorption of two O_2 molecules, and resulting crack advance (see text). Bonds shown are based on time-averaged atomic positions. [76]

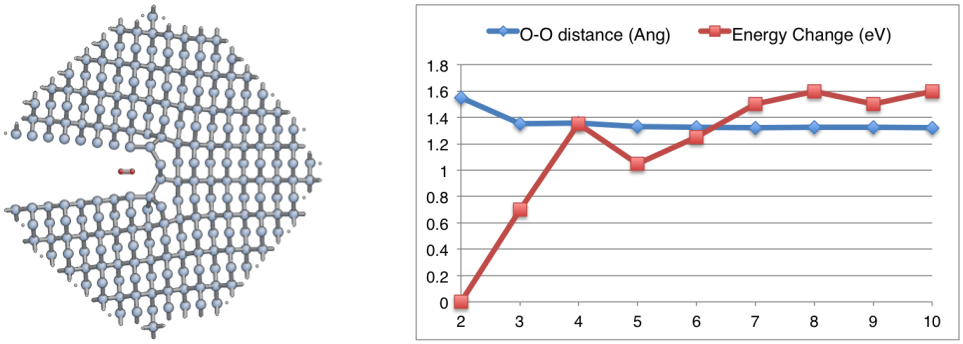

(a) (b)

Figure 3.5: Sensitivity of the O_2 dissociation process. (a) 218 Si atoms cluster with embedded crack on the (110) cleavage plane; (b) dissociation energy (red line, measured in eV on the Y axis) and relaxed O-O distance (blue line, measured in Å on the Y axis) as a function of the molecule distance to the crack tip (measured in Å on the X axis).

the crack tip has been calculated in a cluster containing 218 Si atoms, 1 O_2 molecule and 74 terminating H atoms (see Fig. 3.5). The oxygen molecule was placed into the crack tip at a number of distances d from the tip comprised in the [2 Å, 10 Å] interval and computed the DFT energies of the cluster.

For simplicity only the single degree of freedom corresponding to the O-O bond length was allowed to relax in these tests. These results, illustrated in Fig 3.5b, predict a total energy $E(d) \leq E(10\ \text{Å})$ for the entire interval considered for this system, consistent with the immediate dissociation seen in our dynamics. The small 0.3 eV barrier at a molecule-crack tip distance of 4 Å is probably attributable to -or at the very least enhanced by- the enforced constraints not allowing Si atom motions or molecular rotations, since it did not prevent direct dissociation in the dynamical simulations started from $d = 5$ Å.

3.3.2 Silicon (111)

The second crack system considered was the (111) cleavage plane, in the $[11\bar{2}]$ direction. This cleavage plane offers the least resistance to crack propagation; however, the crack propagates along the $[11\bar{2}]$ direction leaving behind the well known 5-7 Pandey-like reconstruction [82]. This particular reconstruction leaves silicon sites at the newly formed surface with higher chemical reactivity respect to the (110) silicon cleavage plane investigated in Sec. 3.3.1.

For this reason, the crack surface behind the tip was saturated with hydrogen to

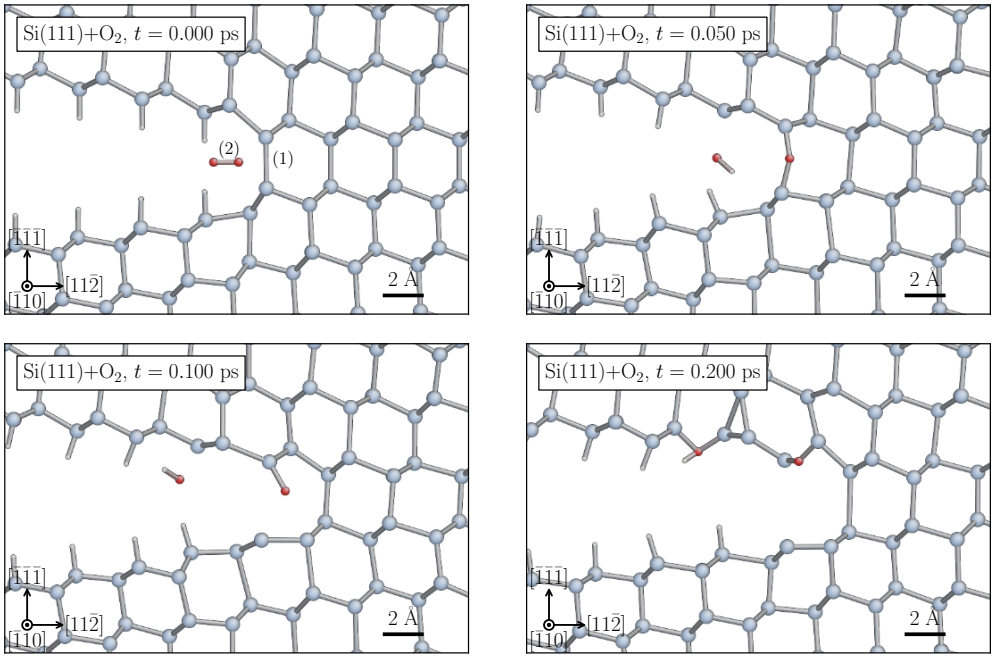

Figure 3.6: Stress corrosion cracking in the Si(111)[11$\bar{2}$] fracture system. As in Fig. 3.4, panels show only the near tip region, treated with QM accuracy. [76] See text for description.

reduce the number of possible O_2 reaction sites. The purpose of the hydrogen saturation is to prevent O_2 molecules added to the simulation from adsorbing on either of the two fracture surfaces before reaching the crack tip. Moreover, in the experimental system (see Sec. 3.4), the Si surfaces would actually be fully passivated for both the (111) and (110) cases, rendering them chemically passive.

The model system is similar to the one chosen for the (110) cleavage plane (see Fig. 3.3), containing 90,730 atoms with dimensions $1200 \times 400 \times 3.84$ Å^3. After a full relaxation of the hydrogen-saturated system, a series of LOTF MD simulation at 300 K have been performed by applying a series of subcritical tensile loads in the range $G = 2.7 - 2.2$ J/m^2. Again, the crack does not advances nor closes up, similarly to the (110) cleavage system analysed above.

At this point of the MD trajectory, an oxygen molecule has been positioned at 1.5 Å of distance from the stressed bond at the crack tip and the first row of hydrogens saturating the back surfaces. The initial position of the O_2 molecule was, in this case, strongly constrained by the topology of the initial system. Any attempt to place the

molecule more distant from the tip yielded a systematic interaction of O_2 with the saturating hydrogen atoms, cancelling any possibilities to detect the chemical attack at the crack tip.

Figure 3.6 shows a series of four snapshots of a LOTF MD simulation in the Si (111) cleavage system. At $t = 0$ (upper left panel), the oxygen molecule (red) is placed at 1.5 Å of distance from the first unbroken SI-Si bond (labelled 1). The O_2 molecule dissociates, and after 50 fs (upper right panel) an oxygen atom forms an OH^- radical, while the other bridges the stressed bond (1), subsequently chemisorbing (at t = 100 fs in panel down left) and leading to crack advance via cleavage of the Si-Si bond labeled (1) at the crack tip. After 0.2 ps (down right panel), both oxygen atoms are incorporated in stable Si-O-Si bridges.

The extreme case of $G = 2.2$ J/m^2 offered several technical difficulties while adding a second molecule to the system: systematic interactions with hydrogen atoms were often observed, mainly due to the severe space constraint offered by the initial conditions discussed above. Loads below the Griffith value for this cleavage plane ($G_c < 2.72$ J/m^2 according to DFT calculation of unreconstructed surface energies) were tested up to two oxygen molecules, yielding the same reactions shown in Fig. 3.6. In summary, I again observe immediate dissociative chemisorption of oxygen molecules at the crack tip followed by Si-Si bond cleavage, leading to crack advance at subcritical energy release rates as low as $G = 2.2$ J/m^2.

3.3.3 Analysis of bond breaking and stress concentration

The bond breaking mechanism triggered by the oxygen dissociation and adsorption at the silicon crack tip can be further investigated by tracking the crack tip position. A typical parameter used for this task is the change in the coordination of atoms consequent to a single bond breaking event. However, chemical reactions occurring at the crack tip may involve several changes in the coordination of the atoms in a few tens of fs, ruling out the possibility to use this simple topological parameter.

Alternatively, the crack advancement can be analysed by considering the long-range elastic effect of the oxygen reaction taking place at the crack tip. The trajectory of the crack tip is then obtained by tracking the position of the atomistic stress field fitted to the Irwin near field solution for a sharp crack (see description in Sec. 2.6.2).

The results of this analysis are reported in Fig. 3.7, relatively to the bond breaking mechanism in the Si(111), (b), and Si(110), (c), cleavage planes during the stress corrosion reaction. The crack advance (green line) is measured by the advancing stress

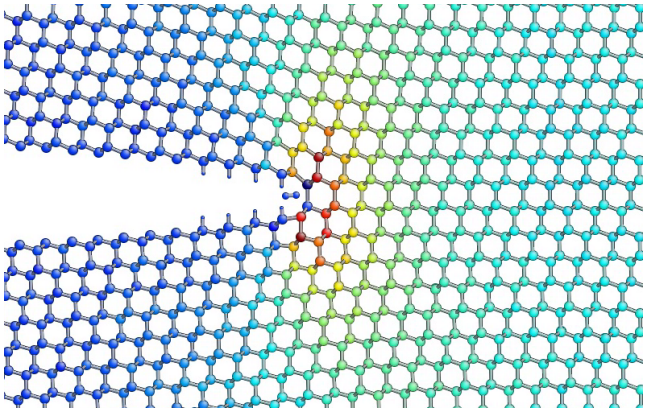

(a)

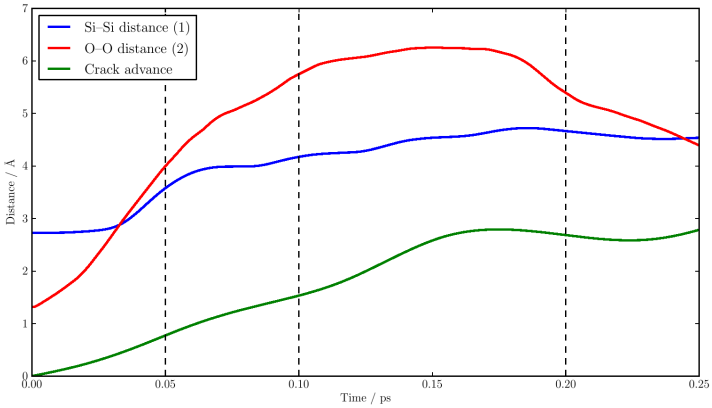

(b)

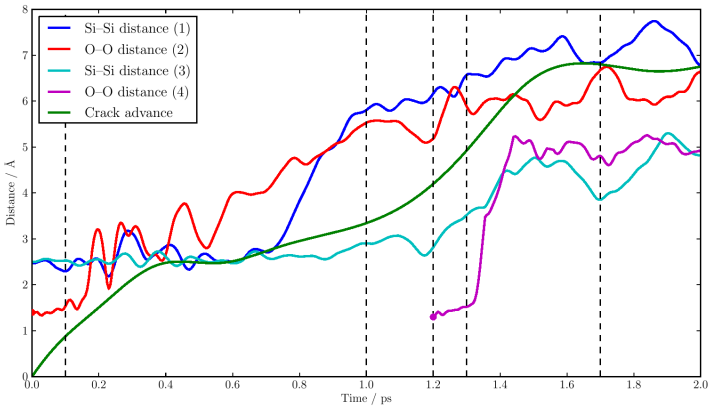

(c)

Figure 3.7: Analysis of bond breaking and crack tip advance. Red and magenta lines: O-O distances, increasing during dissociation. Blue and cyan lines: Si-Si bonds cleaved during crack advance. Green lines: horizontal crack advance, measured by fitting atom-resolved stress field to the Irwin near-field solution. (a) Near tip region of Si(111) + O_2 system with atoms coloured by the average atomistic stress field; (b) Analysis for Si(111) + O_2 system (vertical dashed lines refer to Fig. 3.6); (c) Analysis for Si(110) + O_2 system (vertical dashed lines refer to Fig. 3.4). [76]

field towards the crack propagation direction and compared with concurrent rupture of Si-Si bonds (blue and cyan lines), O-O bonds (red and magenta). Vertical dashed lines correspond to the labeled snapshots illustrated in Figs. 3.6 and 3.4.

In the simplest case of the single oxygen reaction for the Si(111) cleavage plane (Fig. 3.7b) , I see that following the dissociation and chemisorption of an O_2 molecule (O-O distance increasing, red line) the crack advances by a ∼3 Å unit step in the $[11\bar{2}]$ crack propagation direction (green line). The Si-Si bond at the crack tip (blue line) ruptures concurrently with the advance of the stress field. This advance is irreversible due to the bond termination (corking) effect of the adsorbed oxygen.

The advance of the stress field may occur at the same time of Si-Si bond rupture, as shown in Fig. 3.7b for the Si(111) cleavage plane, or before, as we see in Fig. 3.7c for Si(110). The interplay between individual bond breaking events and the long-range elastic behaviour is more complex in the (110) system (Fig. 3.7 down), as the slight blunting of the tip allows a number of distinct reaction pathways.

The first O_2 molecule illustrated in Fig. 3.4 dissociates immediately, eventually leading to the formation of two Si-O-Si bridges. By the time these bridges have fully formed, they are already effectively unloaded, as the centre of the crack tip stress field (green line in Fig. 3.7c) advances very soon after the dissociation of the molecule, leading later to the breaking of the Si-Si bond labeled (1) in Fig. 3.4, in what could be interpreted as a localised toughening response. The adsorption of the second O_2 molecule (labeled 4 in Fig. 3.4) leads, however, to perfectly brittle crack advance, with dissociation and absorption preceding the immediate rupture of Si-Si bond (3).

3.4 Experiment

In an attempt to measure with better precision the cleavage energy in silicon, researchers from University of Haifa[1] introduced an innovative method yielding the lowest value of fracture energy ever seen before. In particular, the experiment was thought to evaluate the cleavage energy in the $(110)[1\bar{1}0]$ and $(111)[11\bar{2}]$ cleavage systems of silicon at room temperature. This communication motivated our computational study on stress corrosion outlined in the previous section.

Considering the large scatter of past results outlined in Sec. 3.2, the experiment aimed to rationalise this situation of uncertainty. Researchers performed high-resolution fracture experiments at room condition to evaluate the cleavage energy of the $(111)[11\bar{2}]$

[1]Anna Gleizer and Dov Sherman, Department of Materials Science and Engineering, Technion, Haifa-32000, Israel

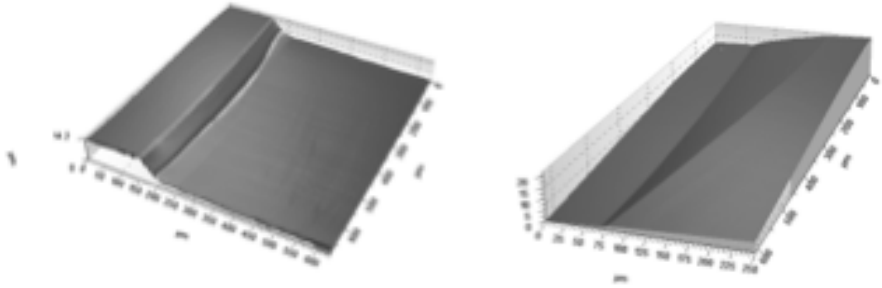

Figure 3.8: Confocal microscopy images showing examples of misalignment steps due to offset (left), or tilted (right) pre-cracks. [76]

and $(110)[1\bar{1}0]$ crack systems of silicon, with round brackets denoting the cleavage plane and square brackets the crack propagation direction. Notched rectangular ($25 \times 42\ \mathrm{mm}^2$) specimens were used, with atomically sharp pre-cracks generated by heating to $\sim$ 180° C, then quenching in a shallow water reservoir. The specimens were then cleaved under tension using the coefficient of thermal expansion mismatch method (CTEM), gluing the silicon specimen to an aluminium loading frame.

The energy release rate at cleavage initiation Γ_0 for each specimen was calculated with the ABAQUS finite element analysis (FEA) code, from the specimen geometry and measurements of the crack length. This loading method leads to non-zero shear stresses for imperfectly aligned specimens. The cleavage energy was first evaluated at room temperature (24°C) and humidity of 55%; some experiments were carried out at humidity of 20%.

Systematically higher values of the cleavage energy were obtained when the pre-crack was either not flat, misaligned, tilted, non-uniform or when the initial notch was blunt. This is in contrast to many materials properties such as strength, yield point, and elastic constants, where averaging is the rule. Therefore, the empirical experience in fracture energy measurements leads to assume that averaging is not correct, as leading to overestimates of Γ_0.

Instead, the best estimate for the cleavage energy of a brittle crystal was considered to be the minimum of all experimental results carried out under the same conditions. This was also the result with the closest to perfect correspondence between the water-quenched pre-crack and the propagating crack.

Another problem taken into consideration during the experiment was the general tendency of the cracks, in the cleavage system $(111)[11\bar{2}]$, to continue propagating on the original plane when the water quenched pre-crack was not well aligned with respect

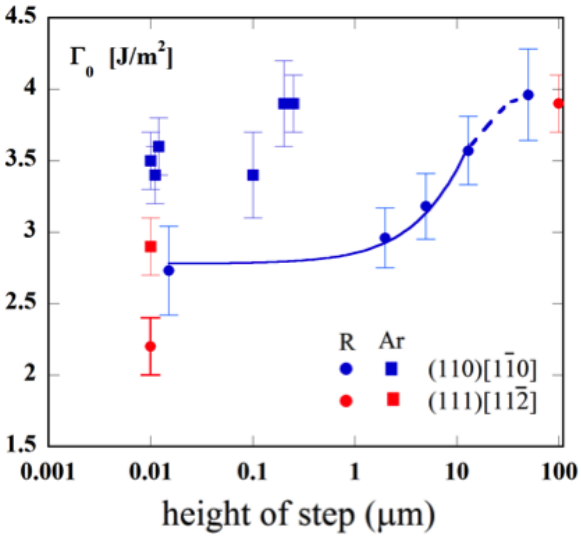

Figure 3.9: The cleavage energy Γ_0 versus the misalignment step height for (110)[1$\bar{1}$0] (blue marks) and (111)[11$\bar{2}$] (red marks) silicon crack systems under room conditions. [76]

to the loading axes. This leads to an additional energy consumption at initiation. Therefore, cleavage systems (111)[11$\bar{2}$] were only analysed provided a very well aligned cracks and very smooth fracture surfaces were attained.

The cleavage energy at initiation for a pre-crack misaligned by 100 μm is 3.9 ± 0.2 J/m^2 (Fig. 3.9 and becomes even higher for larger misalignment. On the contrary, for very well aligned pre-cracks the cleavage energy was systematically lower, yielding $\Gamma_0 = 2.2 \pm 0.2$ J/m^2 (Fig. 3.9, red full circle). The latter value is the lowest value ever obtained for this crack system, and lies below the range of experimental and calculated surface energies.

In the (110)[1$\bar{1}$0] crack system, misaligned or tilted cracks again gave rise to increased values of the cleavage energy. However, in this system, a smooth transition in the cleavage energy as a function of the extent of misalignment was observed. This transition could be directly measured from the height of the steps visible in confocal optical and atomic force microscope images of the fracture surfaces. Plotting the cleavage energy as a function of this step height (Fig. 3.9, blue dots), a surprisingly low result for the minimally misaligned pre-crack of 10 nm was again found. The cleavage energy at initiation for this crack system is again the lowest ever obtained: $\Gamma_0 = 2.7 \pm 0.3$ J/m^2.

To better understand why these lowest values of cleavage energy at initiation were

obtained, the same measurements were performed in a reduced oxygen environment. Hence the experiments were conducted at atmospheric pressure in an inert gas (argon) environment. The assembly was placed in a vacuum chamber, generating an initial vacuum of 10^{-5} tor. In this vacuum conditions, the chamber was filled with 99.994% argon, and again the pressure was reduced to 10^{-5} tor. The procedure was repeated five times.

In argon environment, the cleavage energy at initiation for the $(111)[11\bar{2}]$ and $(110)[1\bar{1}0]$ systems increased to $\Gamma_0 = 2.9 \pm 0.2$ and 3.5 ± 0.2 J/m^2, respectively, as shown in Fig. 3.9 (red and blue full squares). These larger values are in excellent agreement with DFT calculations of 2γ, 2.88 and 3.46 J/m^2, respectively [72].

The clear difference between the two set of measurements, air and argon environment respectively, suggested an important indication. In air environment, the lowest values ever obtained for the fracture energy in the silicon cleavage systems (111) and (110) were obtained. On the contrary, performing the same measurements in argon environment, experimental measures and computational predictions of silicon fracture energy were confirmed. Here was the need to take into account the possibility of subcritical crack initiation induced by chemical agents present in air.

3.5 Discussion and analysis

The experiment summarised in Sec. 3.4 and the computational model of stress corrosion proposed in Sec. 3.3 clear up some long-standing discrepancies both amongst experimental results and between experiments and DFT calculations for the cracking of silicon. The experimental protocol looks at the misalignment between a "pre-crack" and the ensuing crack in order to obtain the lowest yet values of the fracture energy. These values are much less than those calculated with DFT. By redoing the experiments in an inert argon environment a good agreement with DFT is found, leading the experimentalists to suspect that stress corrosion cracking is occurring.

Since experiments at two values of the relative humidity yield similar results, I focused on atmospheric oxygen as the probable culprit, and therefore carried out a QM/MM DFT simulation (Sec 3.3) in order to confirm the possibility. In a number of simulations in both the (110) and (111) systems, I see that the dissociation of a single O_2 molecule provides sufficient heat to oxidise at most one Si-Si bond at the crack tip. That is, at least one oxygen molecule is required for each crack advance step, and in some cases two or three molecules are needed to oxygenate the newly exposed fracture surface before further crack advance can take place.

However, a water-filled crack tip could in principle form at any environmental humidity level, contrary to our assumption above, perhaps introducing capillarity effects. Most importantly, this would shield the tip from the arrival of O_2 molecules from the air reservoir, so that in these conditions the reaction of H_2O molecules with the stresses Si-Si tip bonds would become a likely candidate stress corrosion step.

The existing literature evidence (see Ref. [83, 84]) suggests that at the $K \geq 0.5\ \mathrm{MPa}\sqrt{\mathrm{m}}$ stress intensity factor conditions of the experiment (Sec. 3.4), stress corrosion cracking would propagate distinctively faster than the maximum speed allowed by the need of refilling the water feedstock from the environmental humidity, to make up for the water consumed by the corrosion reaction and the water which remains trapped in the two thin films wetting the crack surfaces by the trailing Laplace meniscus. In these conditions, the typically 0.1 μm water droplet filling the crack would quickly be depleted and could never trail the crack tip for the 50 μm long initiation region observed in the experiment (Sec. 3.4). Even assuming a water-filled cavity extending back from the crack tip by as much as 1 μm, and wetting water films as thin as 1 nm, it is easy to show that for the crack tip aspect-ratio appropriate to the stress concentration of the experiment (a parabolic profile with crack tip opening displacement 15 nm, 1 μm behind the tip, containing 10^{-11} Kg of water per crack front metre) the depletion length could not exceed 5 μm. Thus, any possibly pre-existent water droplet would be swiftly removed, so that the crack propagation in the initiation region would in all cases be due to corrosion by the more abundant/reactive gas-phase species present, namely O_2 molecules in our case.

The purpose of the hydrogen saturation is to prevent O_2 molecules added to the simulation from adsorbing on either of the two fracture surfaces before reaching the crack tip. In the experimental system, the Si surfaces would actually be fully passivated for both the (111) and (110) cases, rendering them chemically passive. Previous experimental and simulation works suggest that a native oxide film forms on silicon surfaces upon exposure to oxygen. The oxidation process is enhanced in presence of water and tensile strain. [85] While the exact passivation mechanism may depend on the precise experimental conditions (the pre-crack notches are produced by a thermal stress technique upon dipping the samples in cold water) I expect oxidation, hydrogenation or hydroxylation to be the most likely mechanisms. In fact there will always be plenty of time for oxidation to occur, since the relatively slow crack advance rate via stress corrosion is limited by the supply of oxygen molecules to the crack tip, which happens by diffusion past any previously exposed fracture surfaces.

The full details of the complex native oxide surface do not, however, play a sig-

nificant role on the dynamics of unbroken Si-Si bonds at the crack tip, which are independent of any passivation further back. In fact, passivation will not significantly affect the stress concentration effect ahead of the crack, while the relatively short Si-O bonds will not cause obstruction to further O_2 supply, as confirmed with our (110) simulations including multiple O_2 molecules. I therefore added the simplest available chemical passivation option to our simulations, and did so only where this was necessary to allow molecules to reach the crack tip region.

For the (110) system, the open crack tip structure of Fig. 3.3 implies a low chance of early adsorption of O_2 molecules, so that passivation is not necessary. On the other hand, for the (111) system, the sharper crack tip of Fig. 3.6 results in a narrower access region for the incoming O_2 molecules, so that some surface passivation was necessary. I consider the (110) and (111) sets of simulations to be equally relevant to the experimental setup described in Sec. 3.4 as the most balanced way to treat the O_2 reaction with the unbroken Si-Si bond at the crack tip.

In summary, I believe that the heat locally released by the exothermic dissociative chemisorption process is efficiently dissipated into the crystal matrix, and never observed to cause breaking of Si-Si bonds not directly bonding with O atoms, yielding multiple advance steps. I note that such a physical effect would be favoured by the periodic boundary conditions I use along the crack front, which correspond to an infinite row of molecules simultaneously approaching the crack tip. I conclude that slow fracture can be initiated at subcritical loads, with the crack advancing by stress corrosion. Since the oxygen dissociation is barrierless, we are in a transport-limited stress corrosion regime where the speed of the crack is wholly determined by the rate of supply of oxygen molecules to the crack tip [86].

3.6 Summary

I find that oxygen molecules play the role of a corrosive agent capable of initiating fracture at subcritical loads on the Si(111) and Si(110) cleavage planes, contrary to the common wisdom in Si. LOTF atomistic simulations (Sec. 3.3) show that cracks in a dry environment do not propagate at energy release rates below the Griffith critical value given by twice the surface energy density, in accordance with experimental measurements reported by collaborators in Sec. 3.4. The presence of the oxygen-rich environment leads to sub-critical crack growth, revealed for the first time by the experiments in vanishing misalignment conditions and confirmed by our LOTF simulations, where the dissociative chemisorption of O_2 molecules, followed by cleavage of individual

stressed Si-Si bonds at the crack tip has been observed.

The additional effect of water on the stress corrosion mechanism was not taken into consideration by assuming the crack tip gas filled; even assuming a water-filled cavity extending back from the crack tip via capillary effects, this water droplet filling the crack would quickly be depleted and could never trail the crack tip for the 50 Å initiation region observed in the experiment. I note that the speed of the subsequent crack growth will be limited by the time taken for oxygen to diffuse to the crack tip [86], so here I have focused only on crack initiation, leaving a full discussion of the influence of the complex rheology of confined fluids on fracture propagation for a future work.

Chapter 4

Crossover from activated to catastrophic fracture in silicon

4.1 Introduction

Silicon has been the primary model for brittle fracture investigations for many decades. It is an extremely brittle material, cleaving to leave atomically smooth fracture surfaces. [3] Its extensive role in technological applications explains why silicon remains one of the most studied materials to this day. Strikingly, however, many features of brittle fracture have not yet been fully understood at the atomic scale. For example, cracks in silicon typically require a fracture energy higher than that expected from simple energetic considerations in order to propagate. [87] Moreover, discrepancies also remain between continuum elasticity theory predictions and experiments for the limiting velocity of cracks under a given applied load. [4, 13]

A molecular dynamics investigation of brittle fracture in silicon has been conducted with a twofold aim: studying the role played by the temperature on the crack dynamics by testing a new interatomic potential. Such study requires to span a broad range of crack velocities as a function of the energy release rate, going from the catastrophic behaviour of a super fast crack to a low speed fracture propagation where activated processes become important.

In general, classical interatomic potentials do not describe brittle fracture accurately. [46] They tend to dramatically overestimate the lattice trapping barriers, leading to fracture energies far in excess of those required to create new surfaces, which is then dissipated via tip blunting and other plastic deformation more typical of the failure of ductile materials. [26] However, the details of stress concentration near a crack tip

in silicon are well described by many classical potentials, with the stress field beyond about 10 Å ahead of a crack tip in good agreement with both higher level quantum mechanical theory and with linear elastic fracture mechanics (LEFM). [42]

This suggests the use of informationally efficient non uniform precision multi-scale techniques (see Sec. 2.5), where the process zone near the crack tip is treated at a higher level of theory than the rest of the system. Such techniques have been applied successfully to explain, for example, dynamical instabilities in the fracture of silicon [51, 88] as well as crack-defect interactions [49] and the emission of dislocations during the transition from brittle to ductile fracture. [89]

In this work, I am interested in accessing longer timescales to probe the dynamical effects of temperature on fracture dynamics. For this purpose a new interatomic potential (described in Sec. 4.2.2), based on quantum mechanical data, has been used to describe the near tip region, leaving the task of describing the long range elastic field to a less expensive and well tested potential for silicon. Results reported in Sec. 4.3 represent the first application of this classical hybrid model to fracture in silicon.

4.2 Theoretical background

4.2.1 Crack speed in brittle materials

The goal of this work is to predict the crack speed behaviour in brittle materials as a function of loading and temperature. Why is the crack speed such an important feature in fracture dynamics? Knowledge of the crack velocity as a function of the energy release rate G provides key information about the crack dynamics and the extent of lattice trapping.

The starting point for most attempts to understand the process of brittle fracture is the well known Griffith criterion [8], based on an energy balance between the energy cost of creating new fracture surfaces and the elastic potential energy relieved by opening a crack (see Sec. 2.2.2.2). The minimal energy required for crack advance is twice the surface energy density γ, namely the energy necessary to open two new surfaces, leading to the Griffith critical loading $G_c = 2\gamma$. However, the elastic energy of a running crack is always higher than the theoretical limit expressed by the Griffith criterion, attributed to the limitations of applying continuum elastic theory when describing systems with discrete bond breaking processes at the atomic level.

The discreteness of the atomic lattice introduces a periodic barrier to crack advance, via the concept of lattice trapping introduced by Thomson and Rana [17] using

analytical models, and subsequently further developed in several computational studies (see Ref. [90] for a review). This barrier is biased by the applied load, reducing as the load increases, with fracture becoming barrierless for energy release rates exceeding a threshold value G_+. A multiscale simulation using tight-binding to describe the process zone around a crack tip in silicon found the lattice trapping barrier falls to zero by about 10% above G_c [46].

Another important feature on the energetics of brittle fracture is the relation between the velocity of the crack and the strain energy release rate G. For a semi-infinite crack in an infinite half plane, LEFM [4] predicts the universal equation of motion reported in Eq. 2.40. $\Gamma(v)$ can be considered constant and equal to the Griffith critical loading G_c. Moreover, for better comparison with other studies, it is useful rewriting Eq. 2.40 rescaling the velocity v to the relevant sound speed c_R and the loading G to the critical one G_c:

$$\frac{v}{c_R} = \left(1 - \frac{G_c}{G}\right) \tag{4.1}$$

where the fracture energy $\Gamma(v)$ has been considered constant and equal to the Griffith critical loading G_c. This equation presents inconsistencies with experiments at both high and low speeds.

The upper limit for a travelling crack should be the Rayleigh wave speed; however, experimentally, this limiting speed is usually a substantial fraction below c_R (between 20% and 80% of c_R). [13] This is attributed to instabilities which make fracture unstable above a critical speed. [15] At intermediate speeds the discrepancy between theory and experiment can sometimes be resolved including other energy dissipation mechanisms such as phonon emission in the fracture energy $\Gamma(v)$. [91] According to Eq. 4.1, the minimal crack speed should be zero for $G = 2\gamma$, but also in this case there is not yet clear experimental evidence for the behaviour of the crack velocity at the onset of fracture. Some experiments observe cracks travelling at a substantial fraction of c_R immediately after initiation, supporting theoretical lattice models and molecular dynamics simulations which suggest a 'velocity gap', or forbidden band of velocities below about 200 K. [16, 19, 92] On the other hand, an experimental study using three point bending reports crack propagation at velocities close to zero with temperatures as low as 77 K, showing no evidence for a velocity gap. [93]

The velocity v of a running crack should increase with increasing energy flow to the crack tip, as I mentioned in Sec. 2.3. Following LEFM predictions, all speeds $0 < v < c_R$ are predicted to be accessible by a running crack. The rescaled Freund equation of motion (Eq. 4.1) is reported in Fig. 4.1, showing the normalised crack speed

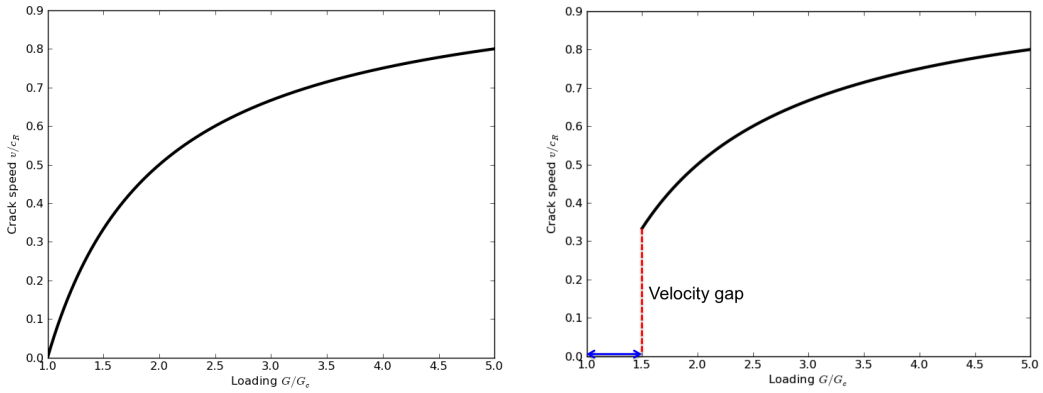

(a) (b)

Figure 4.1: Normalised crack speed (respect to c_R) as a function of the normalised energy release rate (respect to G_c). (a) The Freund equation of motion (see Eq. 4.1); (b) The Freund equation of motion in the case of velocity gap (red dotted line). The extent of lattice trapping is indicated by the blue double arrow.

v/c_R as a function of the normalised loading G/G_c.

In Fig. 4.1a, the crack starts to propagate at the Griffith loading G_c and its speed increases tending to the asymptotic value of c_R [1], as predicted by Eq. 4.1. A schematic plot of the same equation is reported in Fig. 4.1b, considering though the existence of a finite lattice trapping (blue double arrow in the axis of loading) and velocity gap (red double arrow in the axis of velocity). The crack initiates at $G^+ > G_c$ ($G^+/G_c = 1.5$ on the x axis) with nil velocity, and accelerates tending to the limit of c_R.

Lattice trapping and velocity gap represent dynamical instabilities of brittle fracture that, to date, have not been yet fully understood. The challenge of clarifying their origin was the driven force which motivated this computational work. An hybrid approach mixing two MM interatomic potentials has been chosen to accomplish this task. In the next section, the main ingredient used to efficiently model the interatomic interaction at the crack tip will be described.

4.2.2 Methods

Gaussian approximation Potentials (GAP) [94] are a new class of classical interatomic potentials based on DFT calculations. The version used in this work has been embedded, in a hybrid fashion, with SW potential [25] to accurately model the brittle fracture in silicon. GAP is an interatomic potential which does not present an analytical form,

[1] In this work, I refer to $c_R = 4.3$ km/s, calculated by using elastic constants predicted by our hybrid model.

and is based directly on quantum mechanical data. Its implementation concerns the task of modelling the Born-Oppenheimer potential energy surface (PES) of a set of atoms, but without recourse to simulating the electrons explicitly.

A description of the atomic environment is required. To this aim, GAP uses a vector which looks at nonlinear interactions, the bispectrum [95], invariant under rotations, translations and permutations of atoms in the neighbourhood.

The total potential energy is regarded as a sum of atomic energy functions:

$$E = \sum_{i}^{atoms} \epsilon(\{\mathbf{r}_{ij}\}), \tag{4.2}$$

where $\mathbf{r}_{ij} = \mathbf{r}_i - \mathbf{r}_j$ is the relative position between atoms i and j. Imposing the condition $|\mathbf{r}_{ij}| < r_{cut}$, the set of atoms over which the index j runs is restricted to some fixed neighbourhood of atom i, defined by a cutoff radius r_{cut}.

The first step is forming a local atomic density from the neighbours of atom i:

$$\rho_i(\mathbf{r}) = \delta(\mathbf{r}) + \sum_{j} \delta(\mathbf{r} - \mathbf{r}_{ij}) f_{cut}(|\mathbf{r}_{ij}|), \tag{4.3}$$

where f_{cut} is a cutoff function reflecting the spatial scale of the interactions.

The second step consists of projecting the atomic density onto the surface of a four-dimensional unit sphere, which constitutes a natural complete basis for the interior of the 3D sphere. The projection of the atomic density on the surface of the 4D sphere can therefore be expanded in 4D spherical harmonics $U^j_{m'm}$ using coefficients

$$c^j_{m'm} = \left\langle U^j_{m'm} | \rho \right\rangle . \tag{4.4}$$

In practice, the bispectrum $B_{j_1 j_2 j}$ built from these coefficients (see Bartok PhD thesis for a detailed discussion [96]) is truncated, including only terms up to J_{max}, corresponding to a limit in the spatial resolution with which the atomic neighbourhood is described.

The PES is determined by interpolating the atomic energy in the truncated bispectrum space using a non parametric method known as Gaussian process (GP) regression

$$\epsilon(\mathbf{b}) = \sum_{n} \alpha_n G(\mathbf{b}, \mathbf{b}_n), \tag{4.5}$$

where G is a typical Gaussian function depending on the bispectrum components b, and n ranges over the reference configurations.

Then the covariance of the reference configurations is defined as

$$C_{nn'} = \delta^2 G(\mathbf{b}, \mathbf{b}') + \sigma^2 \mathbf{I}, \tag{4.6}$$

where δ and σ are two further hyper-parameters and $\mathbf{I}$ is the identity matrix. The interpolation coefficients are then given by

$$\{\alpha_n\} = \mathbf{C}^{-1}\mathbf{y}, \tag{4.7}$$

where $\mathbf{y} = \{y_n\}$ is the set of reference values (quantum mechanical energies).

Finally, the data directly accessible are not values of atomic energies but forces and stress tensors; furthermore these data can be heavily correlated. This problem is solved by applying a sparsification procedure, in which a predetermined number of sparse configurations are chosen randomly from the set of all configurations and the data values $\mathbf{y}$ are replaced by linear combinations of all data values. The reference configurations are generated from random MD simulations at the DFT level.

In summary, GAP may be regarded as an interpolation of the quantum mechanical potential energy surface. The teaching set used for generating the GAP model used in this work contained atomic environments for 1586 bulk atoms and 1342 (111) surface (both Pandey and unreconstructed forms) atoms, and was sparsified to select the 400 most relevant configurations.

The GAP calculation is embedded within a buffer region (cyan and red atoms) and abruptly mixed with SW potential which describes the long range elastic field. The abrupt mixing method is far more simple than the LOTF method, and surprisingly yields an excellent convergence of the force error in silicon bulk. [38] Considering that the goal of this investigation requires to take into account a much larger time scale than the case of complicated chemical reaction at the crack tip (as shown in Chapter 3), I opted for the more computationally efficient option of abrupt force mixing.

As illustrated in Fig. 4.2, our hybrid GAP+SW technique restores the brittle character of fracture, correcting the anomalous ductile behaviour seen in simulations carried out with the SW potential alone. Furthermore, simulations at 300 K conducted with the GAP+SW scheme reproduced the Pandey-like crack tip reconstruction with 5- and 7-membered rings, as reported in a previous multi-scale study where the near tip region was treated at the DFT level. [51] Whilst the observed fracture behaviour is qualitatively in excellent agreement with DFT-based studies, the Griffith critical loading of the GAP+SW model is $G_c = 2\gamma = 1.56$ J/m^2. Since this value is significantly lower than the experimental value of 2.48 J/m^2 [71], our work should be considered to describe a

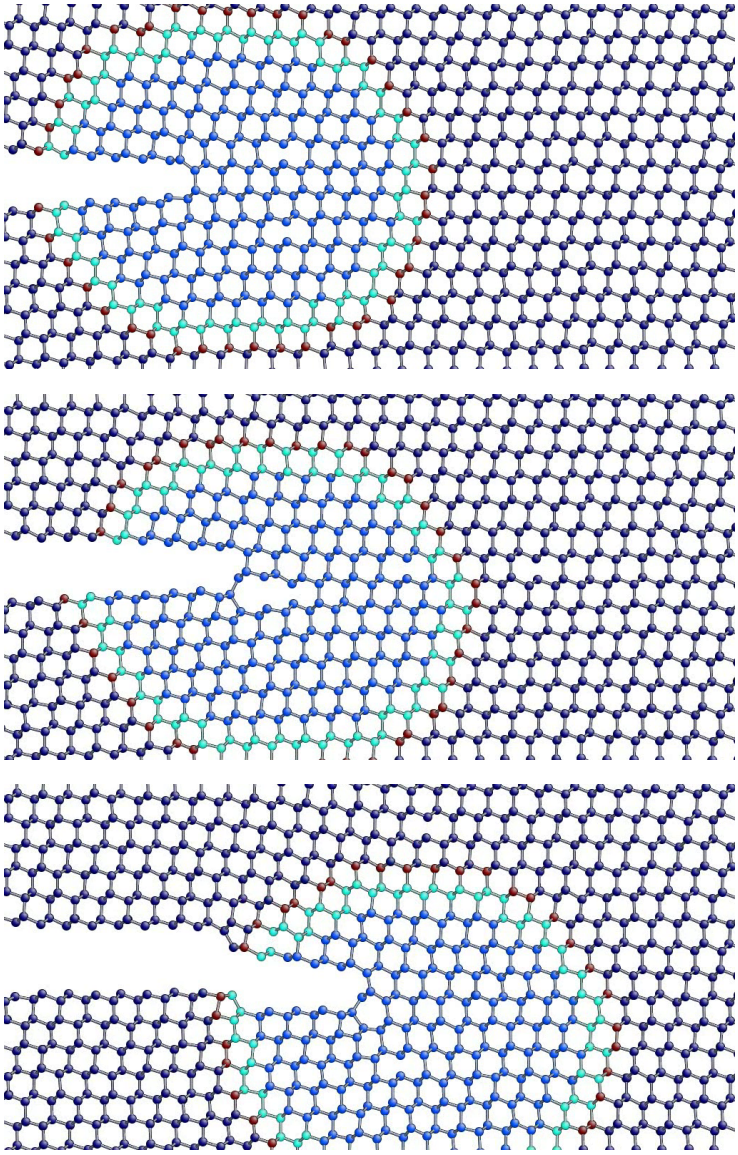

Figure 4.2: Snapshots at intervals of 4 ps from a 300 K simulation of fracture in the Si(111)[1$\bar{1}$0] cleavage system using a QM-derived GAP model for the crack tip region (light blue atoms) and the SW classical interatomic potential to describe the long range elastic field (dark blue atoms). These images are close-ups of the crack tip region in a larger system of size $2000 \times 300 \times 3.68$ Å^3. [97]

model brittle material, rather than silicon *per se*. For consistency reasons, from now on I will refer to the loading G in reduced units ($\Delta = G/G_c$).

4.3 Results

4.3.1 Statistics of bond breaking events

The velocity of the crack tip is related to the frequency of bond breaking events. The crack speed can be then defined by looking at the statistical ensemble of the time elapsed between two successive bond breaking events. By associating each bond breaking event with a change in the coordination number of a pair of atoms, we can record the time of every event as the crack propagates during an MD simulation. Therefore the quantity that fully embodies the physics of the problem is the interval of time Δt necessary for the occurrence of a single bond breaking event.

The average velocity of the crack can be calculated straightforwardly as the ratio between the average advancement when one bond breaks (Δx, known from the crystal structure) and the average time of the distribution ($\langle \Delta t \rangle$):

$$\langle v \rangle = \frac{\Delta x}{\langle \Delta t \rangle} \pm \frac{\sigma_v}{\sqrt{N}}, \tag{4.8}$$

where $\sigma_v = \frac{\langle v \rangle}{\langle t \rangle} \sigma_{\Delta t}$ is the standard deviation of the average speed and N is the number of bond breaking events observed in the simulation. A convenient visual representation of this distribution of the events is then a histogram, with mean $\langle \Delta t \rangle$ and standard deviation $\sigma_{\Delta t}$.

A series of constant temperature loading simulations were performed on a $2000 \times 300 \times 3.8$ Å^3, containing 111,000 atoms and periodic in the crack-front (z) direction. All calculations of crack velocity were made using equation 4.8.

An example of the statistical distribution of bond breaking times is shown in Fig. 4.3, revealing interesting features of the fracture dynamics. Histograms (Fig. 4.3a) display two different distributions relative to cracks travelling at different temperatures and loadings. The solid lines fitting the distributions are calculated by a simple theoretical model thought to interpret the different skewness of the histograms. In fact, although the slower mean velocity for the crack with lower loading is as expected, the different shape of the two distributions is more interesting.

We may model this situation by considering that the slow crack at 300 K may feel a residual time dependent energy barrier which blurs the tail of the distribution

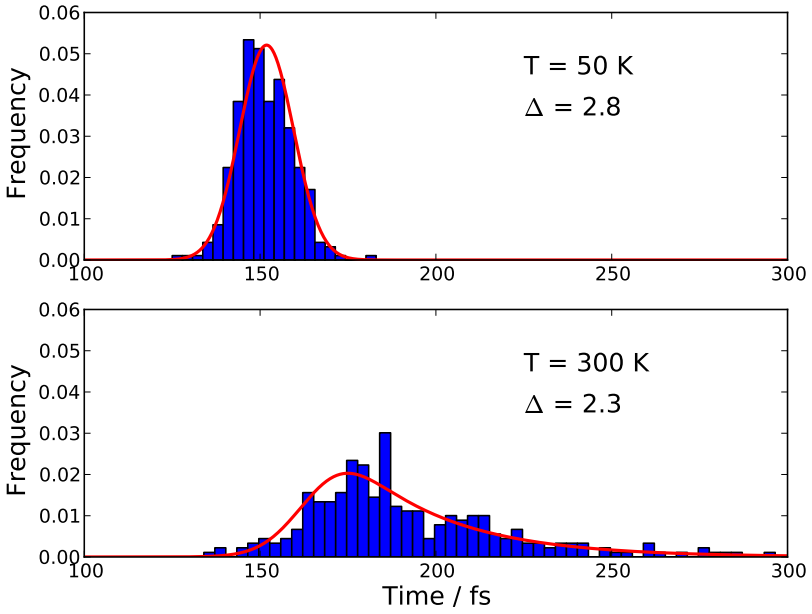

(a)

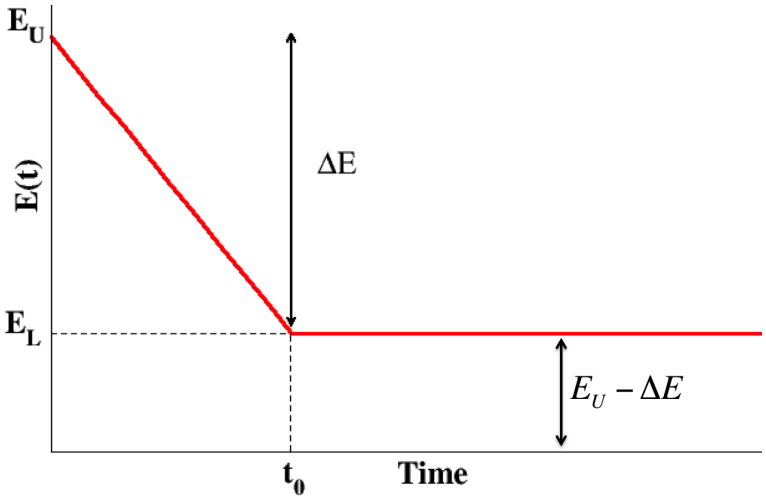

(b)

Figure 4.3: Statistics of bond breaking events fitted by time-dependent energy barrier model. Distribution of time intervals between bond breaking event at 50 K and 300 K are shown by the upper and lower histograms respectively (a). The red curves fitting the histograms have been calculated by applying a simple statistical model where a time-dependent energy barrier for breaking the next bond falls from its initial value E_u to the static value $E_u - \Delta E$ over a time t_0 (b).

(a schematic representation of the energy barrier is shown in Fig. 4.3b). Within this model, the probability that one bond breaks per unit time after a time t is given by the linear differential equation

$$\frac{dP}{dt} = [1 - P(t)]\,\nu \exp\left(-\frac{E(t)}{k_B T}\right), \tag{4.9}$$

which is the product of $[1 - P(t)]$, the probability of the bond not having broken yet and an Arrenhius term formed from an attempt rate ν and the likelihood of crossing a time-dependent energy barrier $E(t)$. We propose that this energy barrier $E(t)$ falls from a relatively high transient value E_u immediately after the previous bond breaks to its equilibrium value E_L over a finite time t_0, corresponding to the elastic relaxation time required for the stress field to adjust so that it is fully concentrated on the new crack tip bond:

$$E(t) = \begin{cases} E_u - \Delta E\, t/t_0 & t \leq t_0, \\ E_u - \Delta E & t > t_0, \end{cases} \tag{4.10}$$

Note that it is the final barrier $E_u - \Delta E$ which should be compared with static calculations of the lattice trapping barrier.

The parameters of the model are the initial and final barrier heights E_u and $E_u - \Delta E$, the stress re-concentration time t_0; the temperature T, the attempt rate ν. We have solved the differential equation (Eq. 4.9) numerically, with the physically motivated parameters given in Table 4.1. To represent stochastic effects, we used an ensemble of stress re-concentration times, normally distributed around a mean value t_0 with standard deviation σ_0. The results of fitting this model to our MD data are illustrated in Fig. 4.3.

This implies that for a range of loadings sufficiently above G_c, the propagation of the fracture is regulated by a precise frequency, namely a tight distribution centred on the average value (e.g. the 50 K - $G/G_c = 2.8$ case of Fig. 4.3). On the other hand, there will be a range of loads for which the crack tip loses regularity in breaking successive bonds, when the crack tip feels the presence of a residual energy barrier. In this case, the interplay between the temperature and energy barriers matches well with the features seen in the "blurred" distribution (300 K - $G/G_c = 2.3$ case).

4.3.2 Crossover of crack velocities

Knowledge of the crack velocity as a function of the energy release rate G provides key information about the crack dynamics and the extent of lattice trapping. Using

MD simulation parameters

Parameter	Description	Catastrophic	Activated
T	Temperature	50 K	300 K
G/G_c	Energy release rate	2.8	2.3

Model parameters

Parameter	Description	Catastrophic	Activated
$E_u - \Delta E$	Residual barrier after stress concentration	0.0 eV	0.9 eV
t_0	Characteristic time for barrier to fall by ΔE	156 fs	165 fs
E_u	Unstrained barrier height	1.0 eV	
σ_0	Gaussian noise in t_0	7.5 fs	
ν	Attempt rate - fastest phonon mode	14 THz	

Comparison of MD and model results

Value	Description	Catastrophic	Activated
$\langle \Delta t \rangle_{\text{MD}}$	Mean bond-breaking time interval - MD	152 fs	194 fs
$\langle \Delta t \rangle_{\text{model}}$	Mean bond-breaking time interval - model	151 fs	191 fs
$\sigma_{\Delta t}^{\text{MD}}$	Standard deviation - MD	7.6 fs	35 fs
$\sigma_{\Delta t}^{\text{model}}$	Standard deviation - model	7.7 fs	30 fs
$\langle v \rangle_{\text{MD}}$	Mean crack velocity - MD	2200 ms^{-1}	1700 ms^{-1}
$\langle v \rangle_{\text{model}}$	Mean crack velocity - model	2250 ms^{-1}	1700 ms^{-1}
σ_v^{MD}	Standard deviation in crack velocity - MD	110 ms^{-1}	260 ms^{-1}
σ_v^{model}	Standard deviation in crack velocity - model	110 ms^{-1}	270 ms^{-1}

Table 4.1: Parameters used in the MD simulations and bond breaking frequency model illustrated in Eq. 4.9, and a comparison of the bond breaking time statistics and corresponding crack velocities measured in MD simulations and described by the model.

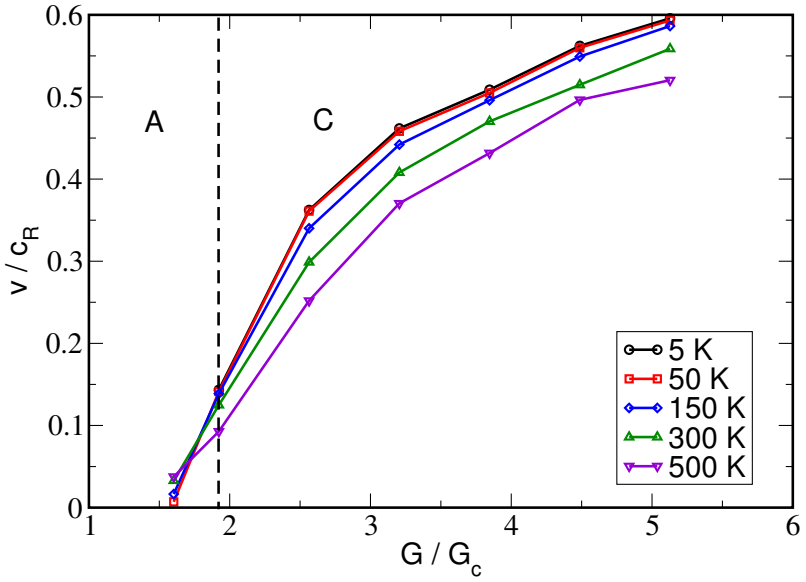

Figure 4.4: Crack speed as a function of loading for five different temperatures. The vertical dotted line separates the activated (A) from the catastrophic (C) region. The velocities for the lowest normalised energy release rate, $G/G_c = 1.6$, were computed by slowing down a running crack (Fig.4.5). [97]

the statistics of bond breaking events described above, a mapping of the velocity of the crack has been made at constant energy release rate and temperature, spanning a range of normalised loadings $1.6 < G/G_c < 5$ and a range of temperatures $5 - 500$ K (see Fig. 4.4). The general trend suggested by this result is that lower temperatures favour higher velocities. This behaviour can be clearly seen in the right hand side of Fig. 4.4.

The lowest loading for which a significant number of bond breaking events for all temperatures are detected is $G/G_c = 1.9$. This provides an estimate for the energy release rate G^+ for our model material, the energy at which the lattice trapping barrier first falls to zero, allowing propagation of cracks at any temperature. The region of loadings $G > G^+$ characterises the catastrophic branch of velocities. For lower energies $G < G_+$, cracks must be thermally activated to overcome the lattice trapping barrier.

Even with the approximate QM description of bond breaking near the crack tip, the timescale limitations of MD make it impractical to measure the velocity of thermally activated cracks starting from an arrested crack. This is particularly important in view of the low speed fracture instability present in this fracture system, which presents an increased barrier to crack advance whenever the crack falls into the 'trap' of the

5–7 reconstructed crack tip (Fig. 4.2). However, low velocity states may be accessed by starting with a running crack and reducing the flow of energy to the crack tip, controlled by the applied strain and the clamped boundaries.

To do this, a silicon slab with dimensions $3000 \times 300 \times 3.89$ Å^3 has been prepared, containing three loading regions (see Fig. 4.5a): Region I ($0 < x < 700$ Å), with the high loading of $G_I/G_c = 3.2$, favouring crack propagation with steady state velocity; Region II (700 Å$< x < 1700$ Å), with smoothly decreasing loading $G_I < G_{II} < G_{III}$, leading to a gentle reduction of the crack velocity; Region III ($x > 1700$ Å), with the low loading of $G_{III}/G_c = 1.6$, allowing us to study low crack speeds where the lattice trapping barrier plays a significant role. Periodic boundary conditions have been applied along the narrow crack front direction, as before. The behaviour of cracks passing through these three regions is reported in Fig. 4.5b.

The main result highlighted in this plot is the transition of the crack velocity from a catastrophic regime in regions I and II to an activated regime in region III. In the cases of 5 K, the crack arrests before entering region III. Above 50 K, a slow crack propagation is detected, with the crack velocity increasing with increasing temperature. This is the thermally activated regime: for a given lattice trapping barrier, the rate of barrier crossing increases with increasing temperature.

Following well established theories of kinetic crack propagation, [3] the lattice trapping barrier is expected to be related to the bond breaking rate r via an Arrhenius-like exponential relation:

$$r = \nu_0 \exp\left(-\frac{\Delta E}{k_B T}\right). \tag{4.11}$$

By plotting the logarithm of Eq. 4.11 as a function of $1/T$ (Fig. 4.5c), a straight line is obtained, with the gradient proportional to the lattice trapping barrier.

Following the above procedure, the lattice trapping barrier is $\Delta E = 0.02$ eV, per unit cell along the crack front, at an energy release rate of $G/G_c = 1.6$. This barrier is reduced as the energy flow to the crack tip increases, and falls to zero above $G_+/G_c \sim 1.9$, i.e. at the onset of the catastrophic fracture regime. Whilst this barrier is not high in absolute value, it leads to a clearly defined dependence of the crack velocity on the temperature, with higher temperatures leading to faster crack propagation.

4.3.3 Test on thermal expansion

Moving now to the catastrophic branch (C) of Fig. 4.4, the key question to be addressed is why the behaviour observed for the activated branch is now inverted, that is, why cracks with the same energy release rate travel faster at low temperatures than at

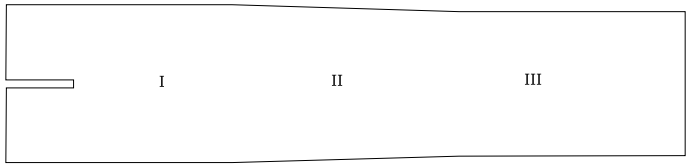

(a)

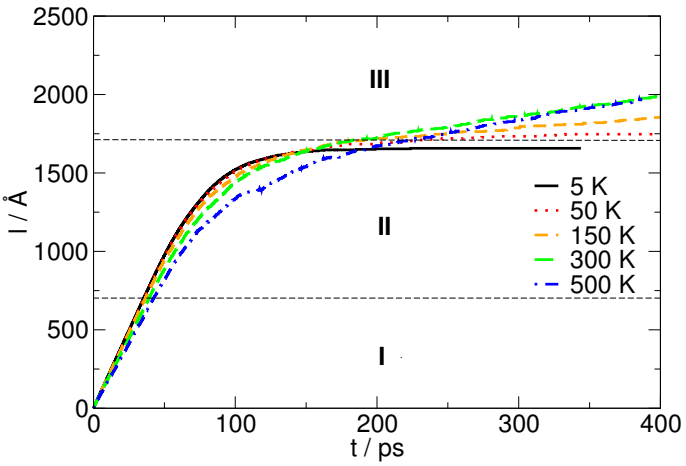

(b)

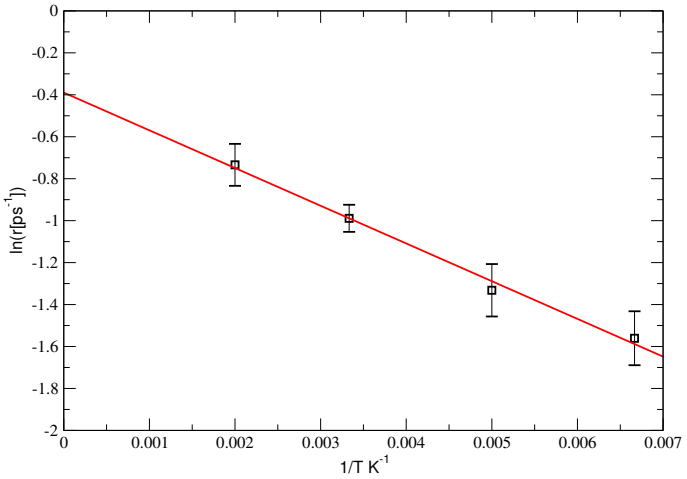

(c)

Figure 4.5: Transition from catastrophic to activated branch of crack velocities. (a) Slab loading scheme used to study the crack speed in 3 different loading regions: region I, catastrophic ($G_I/G_c = 3.2$); region II, spatial decrease of loading; region III, activated ($G_{III}/G_c = 1.6$). (b) Crack length as a function of time for several temperatures; the y axis is divided into three regions, corresponding to the decreasing loads illustrated in panel (a). (c) Arrhenius plot of the bond breaking rate in region III as a function of $1/T$; the slope of the line of best fit is proportional to the lattice trapping barrier for thermally activated fracture. [97]

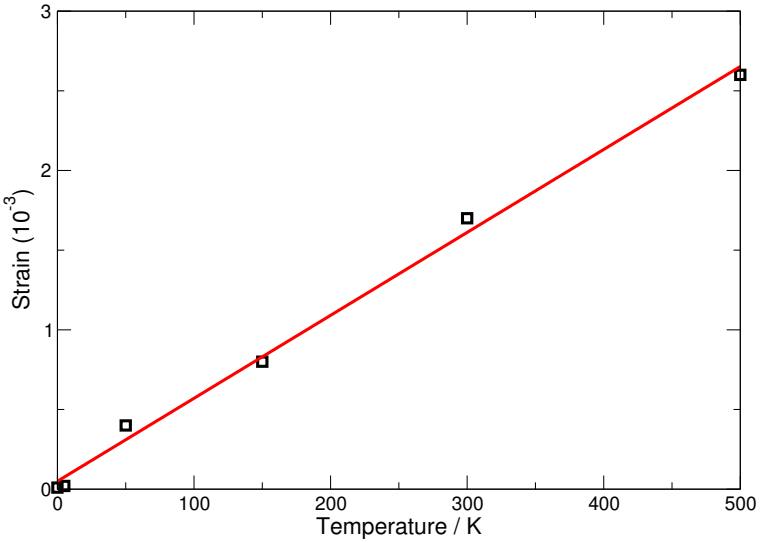

Figure 4.6: Strain as a function of temperature: the slope of the straight line interpolating the calculated point is a measure of the thermal expansion coefficient.

high temperatures. At first sight, it could be an effect of thermal expansion: higher temperatures cause an expansion of the lattice which reduces the effective energy release rate at a given strain. To check if this is the case, we calculated the thermal expansion coefficient for our model material by finding the strain corresponding to zero stress in a $50 \times 300 \times 3.84$ Å^3 silicon slab during MD simulations at a range of temperatures.

In this particular test, the SW potential has been used to model the interaction between all atoms, performing a fully classical MD simulation. This choice is justified by the fact that in the hybrid simulations, elastic energy relieved by an advancing crack originates in the strained classical region ahead of the tip. The stress as a function of the strain has a linear behaviour in a range of small strain ($\pm 5\%$), with fluctuations increasing with the increasing temperature. A running average has been applied to our data sets in order to mitigate the noise of these fluctuations, allowing a better evaluation of strain for which the stress is nil. For different temperatures the value of the strain for which the stress goes to zero is slightly shifted in the direction of increasing temperatures (see Fig. 4.6).

This is nothing but the effect of thermal expansion: the coefficient of thermal expansion describes how the size of an object changes with temperature variations. Specifically, it measures the fractional change in size per degree change in temperature at a constant pressure. For solids one might only be concerned with a change along a

length L:

$$\alpha_L = \frac{1}{L}\frac{dL}{dT}. \tag{4.12}$$

The change in the linear dimension can be estimated to be:

$$\frac{\delta L}{L} = \alpha_L dT. \tag{4.13}$$

The strain points at zero stress as a function of the temperature are fitted by a straight line, which slope gives an estimate of the thermal expansion coefficient: $\alpha_L(Si)_{SW} = 5 \cdot 10^{-6}/K$. The result presented here agrees reasonably well with typical values reported in literature: $\alpha_L(Si)_{SW} = 3.9 \cdot 10^{-6}/K$ [98]; $\alpha_L(Si)_{exp} = 3.2 \cdot 10^{-6}/K$ (within the range $300 - 500\ K$) [99]; $\alpha_L(Si)_{exp} = 2.6 \times 10^{-6}/K$ [100]. Inserting changes in the applied strain of this order into Eq. 2.41 makes it clear that the effect of thermal expansion on the strain energy release rate is too small to explain the significant reductions in crack speed seen at higher temperatures in Fig. 4.4.

4.3.4 Autocorrelation

Temperature may introduce an order parameter in the crack dynamics, an order manifested as a regularity in breaking successive bonds. In the activated branch, namely in the region of loadings G just above the critical value G_c, higher temperatures favour over jumping the lattice trapping barrier, leading to a slow fracture propagation (see Sec. 4.3.2). On the contrary, moving to the catastrophic branch (C) of Fig. 4.4, the behaviour observed for the activated branch is now inverted. The key question to be addressed is: why cracks with the same energy release rate travel faster at low temperatures than at high temperatures?

An answer to this question may be found thinking at the elementary mechanism of crack advancement, namely a succession of bond breaking events in a periodic crystalline structure. The crucial quantity embodying the physics of the problem is the time taken to break two successive bonds. To this end, we consider the autocorrelation of the bond breaking interval statistics. This describes the similarity between successive events as a function of the time separation between them.

Let τ_i be the interval between two bond breaking events, namely the time the crack spend at a particular lattice site. Supposing that the mean value μ and the standard deviation σ of this physical quantity over many hundreds of events can be considered to be time independent, we can express the autocorrelation of our discrete bond breaking

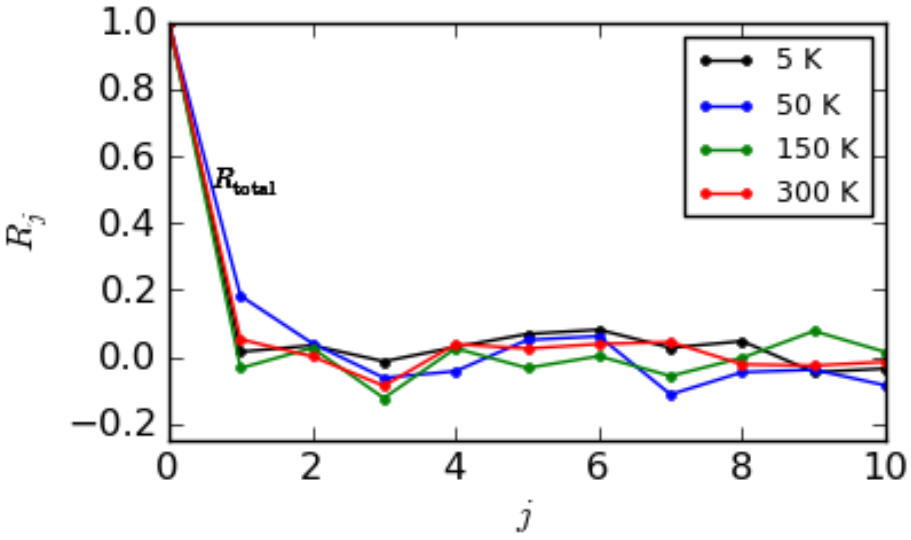

Figure 4.7: Autocorrelation of bond breaking events for four temperatures at constant energy release rate $G/G_c = 3.2$.

events series as:

$$R_j = \frac{1}{N-j} \sum_{i}^{N-j} \frac{(\tau_i - \mu) \cdot (\tau_{i+j} - \mu)}{\sigma^2}, \tag{4.14}$$

with the index j running from zero to $N-1$, N being the total number of bond breaking events, R_j describing how much the time τ_i is correlated to the time τ_{i+j}, averaged over $N-j$ events. In other words, we seek to know how much the jth bond breaking event is correlated to the ith.

The autocorrelation functions for hybrid MD simulations conducted at a constant energy release rate of $G/G_c = 3.2$ for four representative temperatures are shown in Fig. 4.8. The bond breaking time interval data have been cleaned of the first 20 bond breaking events at crack initiation, since the crack velocity was significantly different from the mean velocity. The total autocorrelation function (R_{total} in Fig. 4.8) suggests that there is essentially no significant correlation between bond breaking events. For 10 consecutive events, the autocorrelation profile oscillates around zero for all temperatures, suggesting that bond breaking time intervals do not depend from a specific temperature.

Another way to approach the autocorrelation problem is to split the total autocorrelation function defined in Eq. 4.14 in specific components. To this extent, we define the normalised bond breaking time and the total autocorrelation function by the following

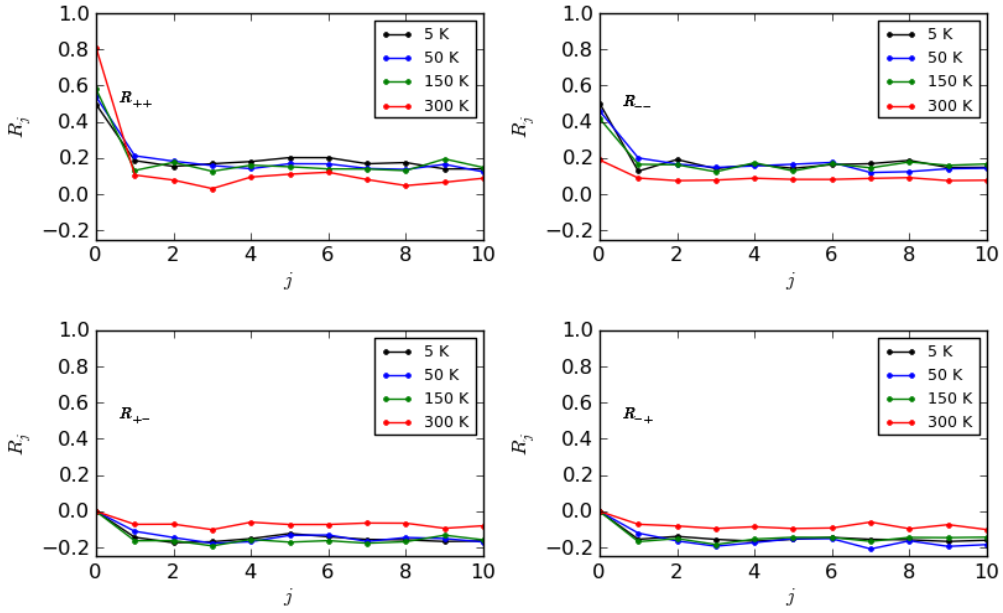

Figure 4.8: Autocorrelation contributions of bond breaking events for four temperatures at constant energy release rate $G/G_c = 3.2$. See Table 4.2 for a description of each contribution.

Table 4.2: Description of autocorrelation contributions

R^{++}	R^{--}	R^{+-}	R^{-+}
$\tilde{\tau}_i > 0$ and $\tilde{\tau}_{i+j} > 0$	$\tilde{\tau}_i < 0$ and $\tilde{\tau}_{i+j} < 0$	$\tilde{\tau}_i > 0$ and $\tilde{\tau}_{i+j} < 0$	$\tilde{\tau}_i < 0$ and $\tilde{\tau}_{i+j} > 0$

equations:

$$\tilde{\tau} = \frac{\tau - \mu}{\sigma}, \tag{4.15}$$

$$R_j^{\text{tot}} = \frac{1}{N-j} \sum_{i=0}^{N-j} \tilde{\tau}_i \cdot \tilde{\tau}_{i+j}, \tag{4.16}$$

where contributions to the autocorrelation are resolved by sign of $\tilde{\tau}$ (positive is 'late' with respect to mean, negative 'early').

Separating the contributions of the autocorrelation as reported in Table 4.2, we observe the existence of a weak positive (for R_{++} and R_{--}) or weak negative (for R_{+-} and R_{-+}) correlation for temperatures lower than 300 K. This could enhance the ordering of the crack dynamics at low temperatures or, viewed from the opposite

perspective, too much thermal energy may prevent cracks from propagating cleanly. Seen from this perspective, a weak autocorrelation is present for temperatures lower than 150 K, whilst room temperature cracks conserve the same behaviour reported in the total autocorrelation function.

4.4 Discussion and analysis

The velocity of the crack shows interesting temperature-dependent features unobserved so far in experiments. Within the limits of the hybrid model GAP-SW, the result of the transition from the activated to the catastrophic branches of the crack velocities contains a physical insight which goes beyond a necessary, and hopefully feasible, experimental demonstration. From a theoretical point of view, the argument of the autocorrelation of bond-breaking events could explain why cold cracks travel faster in the catastrophic regime. However, as it has been shown in the previous section, the weak contributions arising from Fig. 4.8 lead us to assume a more conservative approach.

A minimal theoretical model thought to interpret the crossover of crack speeds in function of loading and temperature has been proposed by collaborators [97]. This model describes the situation of two atoms interacting via a Lennard-Jones (LJ) potential in two distinct cases. In the first one (Fig. 4.9 left), the atom bonds are characterised by the same stiffness, simulating the situation of a matrix of atoms where the stress is uniformly distributed. In the second one (Fig. 4.9 right), the central bond is weaker than the other bonds, presuming the existence of a stress concentration at at the centre and uniform stress distribution in the rest of the atoms matrix. This last case approaches more closely the effect of stress concentration at the crack tip, whilst the first one focuses essentially on the dynamics of a single bond rupture.

The bond is considered broken when the mutual atom distance is three times their equilibrium distance. The total energy of the system is described by the equation:

$$E = U_{LJ} + K, \tag{4.17}$$

where U_{LJ} represents the static contribute of the Lennard-Jones potential whilst K is the kinetic contribute depending on the mutual oscillations of the atoms. In Fig. 4.9 the work necessary to break the bond (W) is plotted against the velocity of separation v, with W measuring the energy variation ΔE at the time the bond breaks. The velocity of separation v, proportional to the applied load, is kept constant for each single calculation of W.

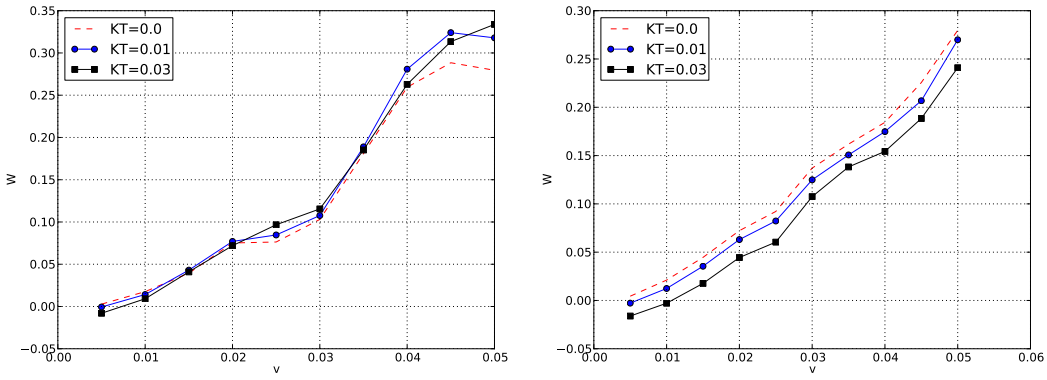

(a) (b)

Figure 4.9: Work spent to break an atomic bond in function of the velocity of the atoms separation rescaled by the speed of sound for three different temperatures. (a) 1D model of atomic bond; (b) 1D model of a triple bond. [97]

In the single bond model (Fig. 4.9a), at low loading (low values of v), higher temperatures yield lower values of W, namely finding less resistance to break the bond than lower temperatures. On the other hand, at high loading (high values of v), the bond breaking mechanism seems favoured for lower temperatures: in this region of fracture energies, colder system find less resistance to rupture (namely the work W to break a bond is lower for lower temperatures). This simple model, based on the Lennard-Jones potential, gives an interesting interpretation of the crossover of crack speeds from the activated to the catastrophic branch highlighted by our MD simulations (see Sec. 4.3.2).

On the contrary, Fig. 4.9b offers a different interpretation of the bond breaking mechanism. By assuming that the central bond is weaker than the other bonds, the theoretical model based on LJ potential shows that higher temperatures encounter less resistance to bond rupture in the whole range of loadings (velocity of separation v) considered.

Finally, we conclude this analysis bearing in mind one of the questions that motivated us to undertake this work: Does a velocity gap exist? According to the autocorrelation of bond breaking times reported in Fig. 4.8, there is no significant evidence of a forbidden band of velocities in the crack dynamics. However, the crossover of crack speeds observed in our simulations suggests that crack travelling at temperatures lower than 150 K may be susceptible to rarely over jump the lattice trapping barrier, becoming therefore more prone to initiates at a finite velocity for a certain G^+. This intuition is in agreement with the minimal one-dimensional theoretical model (Fig. 4.9a), based

on LJ potential, thought to clarify the bond breaking mechanism in function of loading and temperature.

On this basis, I still believe that results of my MD simulations, using the hybrid GAP-SW model, offer yet another opportunity to clarify the importance of temperature in determining crack behaviour. Moreover, they confirm the conventional wisdom on silicon fracture using a new classical potential with stronger reproducibility than many others in the field.

4.5 Summary

Hybrid simulations of brittle fracture in silicon have demonstrated an important interplay between temperature and loading in determining the dynamics of the crack. Using a statistical approach to measuring the velocity of the crack, I have studied how the dynamics of bond breaking are seriously affected by these two variables. In particular, I have identified two branches in the crack velocity related to two regions of loading: activated and catastrophic. The activated branch is characterised by a lattice trapping barrier of about 0.02 eV at $G/G_c = 1.6$, decreasing to zero with increasing the loading, and therefore favouring crack initiation for higher temperatures. In the catastrophic branch, cold cracks appear to be faster. I show that the autocorrelation of bond breaking events for temperatures below about 150 K can not be the cause of this interesting and unexpected phenomenon.

A simple theoretical model in the simplest one-dimensional (Fig. 4.9a) case confirms the existence of a crossover of crack velocities in function of loading and temperature. However, by adding additional degrees of freedom (see discussion in Sec. 4.4 referred to Fig. 4.9b), the crossover disappears, showing that higher temperatures are always favoured in the bond breaking mechanism.

As a future work, a three-dimensional MD simulation (namely by removing periodic boundary conditions along the crack front direction z) could clarify this enigma. From the experimental point of view it would be extremely interesting to test these predictions in an experimental setting.

Chapter 5

Brittle fracture in glassy systems

5.1 Introduction

Glass is a boundary by definition: it is an hybrid state of matter, in between solid and liquid phases; it divides exteriors from interiors for its excellent transparency; it preserves goods from the environment for its insulating properties. Glass is also a prototype of brittleness: empirical evidence shows that a weak impact with hard materials may determine irreversible damage to its structure, resulting often in very sharp cracks. The pioneering work of fracture mechanics (see Sec. 2.2) has been strongly inspired by glass, in an attempt to understanding the origin of brittleness. Mainly composed by amorphous silicon dioxide (a-SiO_2) in its most familiar form, glass owes its brittleness to the extreme homogeneity of its structure along with the strength of its covalent bonds. [56]

Understanding fracture in silicates has a huge technological and scientific relevance, including mining, where a huge amount of energy is required to fragment rocks into fine powder, medicine (biomedical implants, glassy pharmaceutical containers) and civil engineering, where new materials made by glass are increasingly used in structural and energetic applications. Research carried out for this thesis has been funded by ADGLASS[1] project, a European consortium[2] devoted to improving the efficiency, functionality and reliability of glass products for pharmaceutical and thin layer optical photovoltaic applications.

After the investigation of stress-corrosion mechanisms (Ch. 3) and catastrophic frac-

[1] Adhesion and cohesion at interfaces in high performance glassy systems - www.adglass.eu

[2] Participants: Fraunhofer IWM, Friburg; Fraunhofer IFAM, Bremen; King's College London; Cambridge University; ICTP, Trieste; Technion IIT, Haifa; Schott AG, Germany; Aerial, France. Funded by the *Seventh Framework Programe*, European Union Commission.

ture propagation (Ch. 4) in silicon, we now aim to test our hybrid atomistic modelling method (Sec. 2.5) in amorphous silica compounds. The procedures followed to realise a model of seed crack in amorphous silica realisations are presented in Sec. 5.3, involving their generation from cristalline structures and the fracture simulations of crack-free samples. We have then focused on testing our hybrid technique, with particular attention paid to the computational cost, and to the variation of the quantum zone during the molecular dynamics.

5.2 Theoretical background

5.2.1 Amorphous Silica

Amorphous silica a-SiO_2 is a disordered structure of the chemical compound silicon dioxide SiO_2, which is most commonly found in nature as sand or quartz. It is the main constituent of the most familiar type of glass (soda-lime glass) and plays an essential role in both science and industry, and in our daily life. Since the pioneering work of Griffith in fracture mechanics (see Sec. 2.2.2.2), glass has been a useful material for the process of understanding brittleness. Silicate glasses are isotropic materials because of their amorphous structure, and are characterised by a strong degree of homogeneity, giving excellent transparency.

The disordered network of amorphous SiO_2 consists of tetrahedral units of SiO_4 bridged by oxygen atoms, undergoing a glass transition at $T_G = 1482$ K [101]. According to Ojovan [101], the glass formation can be treated as a percolation transition in the system of network defects, with a change in the geometry of the defects from fractal in the liquid state to Euclidean in the glassy state. These defects are thought as elementary excitations resulting from broken bonds and are called configurons [102]; the symmetry breaking at the glass transition is then described as a change of Hausdorff dimension of these configurons.

In the computational field, a big issue in studying such a structure is the size of the system. For some systems it is reasonable to use a small system size: in crystals a small cell is infinitely reproduced across the space; moreover also in liquids (ergodic systems) a small system size is sufficient to achieve good statistical averaging. In contrast, an amorphous system, which is in principle non ergodic, can have many possible network configurations that have nearly equal free energy. Therefore a large size of the sample has to be selected for our MD simulation in order to have a good representation of the structure.

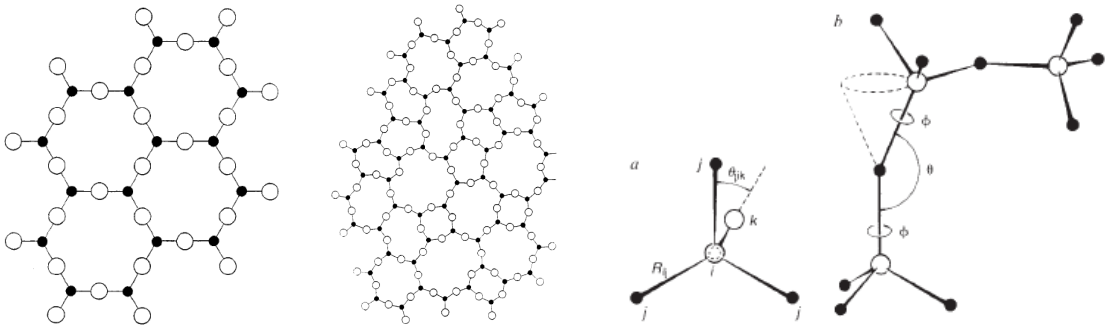

(a) (b) (c)

Figure 5.1: Structure of silicon dioxide. Planar view of crystalline (a) and amorphous (b) structures of silicon dioxide. [103] (c) Illustration of short range order (left, upper a) and medium range order (right, upper b) in amorphous SiO_2. [104]

An interesting way to attack this problem is reported in Ref. [105], where an ensemble of ten samples containing 72 ions (24 SiO_2 units) has been used in order to reproduce the characteristics of the glass. These simulated samples have been tested by analysing the molecular features of the silica network, which are characterised by a short and medium range order. The short range occurs at the level of tetrahedra and can be characterised by radial distribution functions and bond-angles distributions. The medium range is represented by the possible connections via oxygen atoms of these tetrahedral units into more extended structures and rings: although there is no long range periodicity typical of other crystals, there is a preference of the network to form rings of 6-tetrahedra. [104]

5.2.2 Methods

Studying a material at the atomistic level involves the development of accurate potentials which must capture the physics of the problem. A typical dilemma in the field of simulation is the choice between an ab initio approach and an empirical approach. According to the specific problem we are looking at, a reasonable compromise is to use both approaches: quantum mechanics focusing on a few atoms where electronic effects can not be neglected, whit a classical force field describing the interatomic interactions of the majority of atoms, representing the electronic effects in a phenomenological way (see Sec. 2.5.1). Thus, the choice of an appropriate force field becomes a crucial element.

Silica is a prototype of ionic systems with a great importance in technological applications. Ionic system are usually represented by a pair potential in the Born-Mayer

form [106]:

$$U_{ij} = \frac{q_i q_j}{r_{ij}} + B_{ij} e^{-\alpha_{ij} r_{ij}} - \frac{C_{ij}}{r_{ij}^6} \tag{5.1}$$

where U_{ij} is the interaction energy between ions i and j, $r_{ij} = |\mathbf{r}_i - \mathbf{r}_j|$ is the distance between ions i and j, q_i is the charge of ion i which plays the role of a parameter and B_{ij}, α_{ij} and C_{ij} are constants parameters. Following the simple Born-Mayer form, the pair potential of van Beest, Kramer and van Santen (BKS) [107] has been undoubtedly the most utilised in the past. This potential, parametrised to reproduce the behaviour of small hydrogenated silica clusters, treats silica as an ensemble of rigid ions that are not sensitive to their environment.

Tangney and Scandolo presented in 2002 a classical interatomic force field for liquid SiO_2 (TS) [108], with the main aim of accounting for the large polarisability of the oxygen ion. They used a potential of Morse-Stretch form to describe the pairwise interactions between ions

$$U_{ij} = \frac{q_i q_j}{r_{ij}} + D_{ij}[e^{\gamma_{ij}[1-(r_{ij}/r_{ij}^0)]} - 2e^{(\gamma_{ij}/2)[1-(r_{ij}/r_{ij}^0)]}], \tag{5.2}$$

where the interaction between an atom of type i and an atom of type j is defined by the parameters q_i, q_j, D_{ij}, γ_{ij}, r_{ij}^0 and the distance between them r_{ij}. The advantage of this form compared to the simpler Born-Mayer is the transferability between different phases. The effects of dipole polarisation of the oxygen ions has been taken into consideration by assigning to the oxygen ion a single parameter α corresponding to the dipole polarisability. The computation of the inductive effects of dipole moments then involves using the Ewald summation scheme. Ewald summation replaces the summation of long range interaction energies in real space with an equivalent summation in Fourier space.

A recent reformulation of the TS interatomic force field for Silica [109] removes the requirement of performing an Ewald summation. This summation heavily affects the computational cost, scaling as N^2 for typical bi-dimensional systems used in fracture simulations. Considering the screening effect of electrons between nuclei, this reformulation assumes it is possible to truncate electrostatic interactions for specific systems and specific physical properties. The original TS potential is made short-range applying a Yukawa screening function to Eq. 5.2 of the form

$$Y = e^{-\beta r_{ij}} f_c(r_{ij}), \tag{5.3}$$

where $f_c(r_{ij})$ is a cutoff function which takes the potential smoothly to zero at some distance r_{cut}. A full re-parametrisation of the potential has then been made using DFT-LDA to calculate forces, energies and stresses on a representative database of atomic configurations. This screened version of TS potential scales linearly with the number of atoms, allowing a consistent speed up for systems containing more than 6000 atoms.

5.3 Results

5.3.1 Crackless simulations

A crackless simulation represents the procedure of pulling apart a material which does not contain any initial fracture. The aim of conducting this method on amorphous silica cells was to reproduce a "more realistic" fracture surface which could be used as a seed crack in standard fracture simulations. In fact, a standard simulation requires the presence of a preexistent seed crack in the structure (see Sec. 2.6.2).

For crystalline materials this can be simply obtained by cutting all the atomic bonds along a crystal plane. On the contrary, amorphous structures do not offer this possibility. Instead of "manually" inserting a crack seed, we opted for an unbiased procedure to generate a more realistic fracture template.

Firstly, we obtained an initial cell of amorphous Silica by slightly distorting an alpha-quartz cell to make it cubic, before setting the density to the experimental value of 2.2 g/cm^3. The system was initially thermalised at 5000 K for 50 ps and then cooled to room temperature at an annealing rate of 0.01 K/fs. Using a time step of 0.1 fs for the high temperature regime guarantees energy conservation within 10^{-6} k_BT/ps. Finally the configuration at 300 K was structurally optimised, by relaxing lattice vectors and atomic positions.

At room temperature and below almost all silicon atoms within the amorphous structure are four-fold coordinated. We occasionally observe defects, mainly three- and five-fold coordinated atoms, and even less frequently we detect two-membered silicon rings. The elastic properties of the optimised configuration obtained with the TS potential are shown in Table 5.1.

The agreement with experimental data is very satisfactory. Starting from a template cell of 10000 atoms obtained following the above procedure, we aimed to study how different cell sizes can affect the structural order. We then replicated the initial template cell along the three dimensions.

As a secondary study, we reproduced the same quenching procedure used for the

Table 5.1: Equilibrium density and elastic properties of amorphous silica

	δ g/cm^3	B GPa	E GPa	ν	C_{11} GPa	C_{12} GPa	C_{44} GPa
Experiment	2.2	38.0	69.1	0.197	76.5	18.8	28.9
MD simulation	2.3	36.9	69.1	0.174	73.6	21.7	30.1

template, in order to remove the false periodicity introduced by replicating the initial cell. Once these amorphous structures have been relaxed, a molecular dynamics examination of the fracture process was started.

Previous molecular dynamics studies report that when dynamic loads are applied to brittle materials, the system fails under the rapid propagation of cracks. If a dominant crack is not present a spalling of the material takes place due to the nucleation, growth and coalescence of multiple flaws (cracks, voids). In a recent study by Muralidharan et al (2007) [110], using the BKS potential, the authors were able to reproduce this mechanism, calculating the stress strain behaviour for several strain rates. Moreover, they where able to reproduce further features of the fracture process, like the scaling of void size with sample size.

Thirdly, we began a series of crackless simulations by rigidly displacing the top and bottom surfaces of our amorphous silica samples. To break the slab, our samples were subjected to constant strain rates of 0.02/ps, 0.01/ps and 0.005/ps at constant temperature of 300 K, with the strain applied uniformly throughout the sample.

In Fig. 5.2 the uniaxial stress component σ_{yy} as a function of the applied strain is shown for three different strain rates. The failure of the system is clearly identified by a maximum in the stress, related to a critical strain independent from the strain rate; however, the critical stress increases for higher strain rates, confirming the hypothesis that lower strain rates favour a more equilibrated system.

The graphic highlights the presence of two main regions separated by a dotted line: an elastic region (I) for $0 < \epsilon < \epsilon_c$ and a void-coalescence region for $\epsilon > \epsilon_c$. Region I is characterised by a linear behaviour of the stress in function of the strain. Initially, by rigidly displacing the upper and lower boundaries of the structure, atomic bonds strain accordingly. However, the failure of the system is mainly attributable to the presence of nanoscale voids. These voids, characteristic of amorphous silica structures, also grow elastically; for high critical values of strain, some voids grow more rapidly than others until their coalescence become irreversible, leading to the separation of the material and

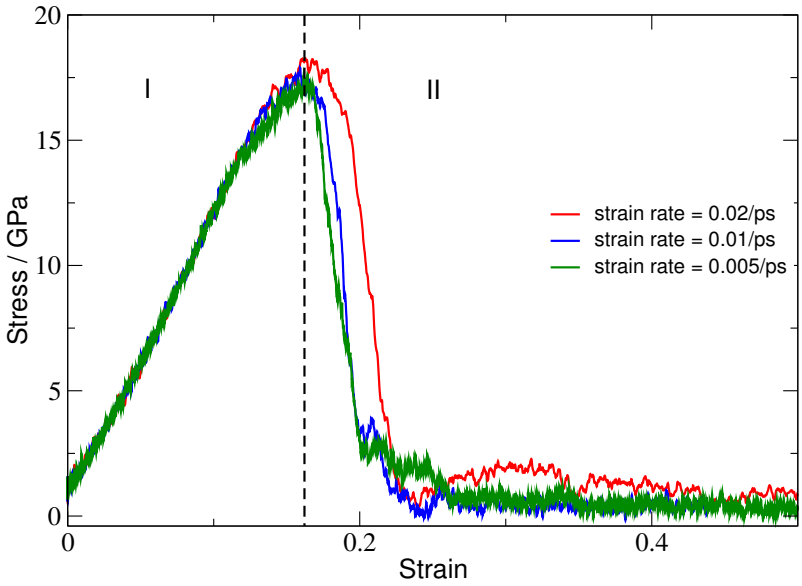

Figure 5.2: Uniaxial stress-strain curves for TS-modified glass. The dotted line separates the elastic region (I) from the void coalescence region (II).

the formation of the fracture surfaces (region II). In the coalescence phase the stress drops dramatically to zero, accounting for the release of elastic energy associated with the creation of the fracture within the whole structure.

By following this crackless procedure for several sample sizes, we finally chose as a "seed crack template" a well formed fracture, farther from the boundaries and with smooth fracture surfaces. The surface morphologies obtained by straining the slab until failure were then used as a template to create the initial seed for our future fracture simulations. However, we had to develop a stable strategy to transfer the surface topology within the un-deformed sample. The best results have been obtained by using two-dimensional alpha-shape functions [111]. The method applies an algorithm, which takes into account the topologic structure of the system and allows us to detect the shape of a set of points in a plane, the points in our system corresponding to the atomic positions. In our particular model, the alpha-shape method defines straight lines delimiting the open surfaces. These shapes are then used to detect the equivalent surfaces inside the original un-broken slab. Since the method is developed for points located in a plane, we considered the slab as being cut into slices along the z direction. By applying the alpha-shape for each slice within the xz plane and eventually summing up the shapes of all the slices, we arrive at a map of the whole surface.

5.3.2 Catastrophic fracture propagation

Several initial seed cracks have been prepared at different strain energy release rates G. In our classical simulations, for $G \leq 3$ J/m^2, the seed crack closed up during the thermalisation process at 300 K, indicating that this is the lower extent of the lattice trapping range. Starting from an equilibrated configuration, we then performed classical molecular dynamics simulations, increasing the applied loading at a rate of 10^{-4} J/m^2/fs for five different temperatures.

The first feature emerging from the analysis of these MD trajectories (see selected snapshots in Fig. 5.3) is that the crack advances for loadings $G^+ > 10$ J/m^2, where G^+ measures the fracture toughness of our system. The stress applied is locally released by the many voids spread within the amorphous silica structure. The void size increases with increasing loading, and eventually their coalescence becomes the main process of fracture formation.

For all the temperatures tested in the $5 - 500$ K range, the formation of several 2-membered (2M) rings have been detected (see Fig. 5.4). This local structure, widely described in the literature [105, 110], naturally forms during the molecular dynamics even for high loading ($G > 12$ J/m^2). These 2M rings have been experimentally shown to provide sites for reactions with water and other impurities [112], and are therefore important for stress corrosion cracking.

After investigating the fracture mechanisms in amorphous silica with a fully classical approach, we tackled the problem with a more refined methodology: the QM/MM LOTF technique (see Sec. 2.5). For describing the region far away from the inner quantum zone, we used the TS potential, since it turned out to be a very reliable and stable force field. This classical potential was then combined with an ab initio description for a few atoms located around the crack tip, whose energies and forces were calculated at QM precision with the CP2K code.

Long-range electrostatic forces play a key role in ionic materials such as silica, so the electrostatic environment generated by the far away MM atoms must be included in the QM calculation. The hybrid region was initialised at the exact crack tip, and the selection of the quantum active region was carried out following topological criteria. Namely, we chose all the Si atoms contained within a given radius. All the O atoms connected with the selected Si atoms were then also included in the active quantum zone.

Once the quantum zone was selected, a buffer region surrounding the inner core was grown following a bond hopping approach, in order to give converged forces on the

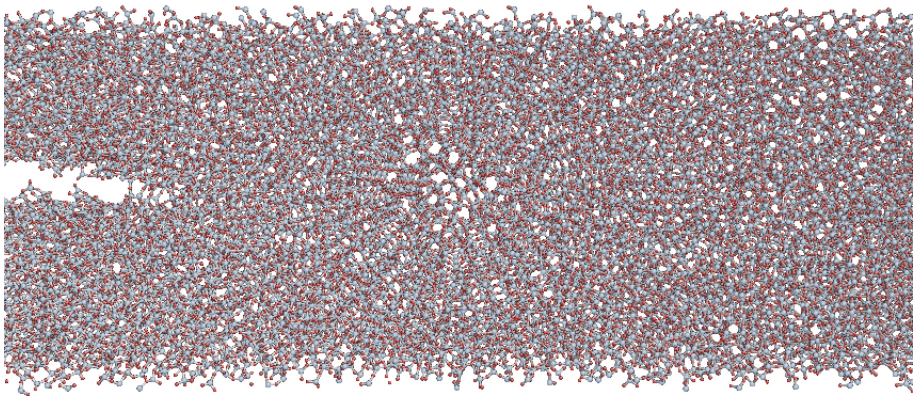

(a) $t = 0$ ps; $G = 5.6$ J/m^2

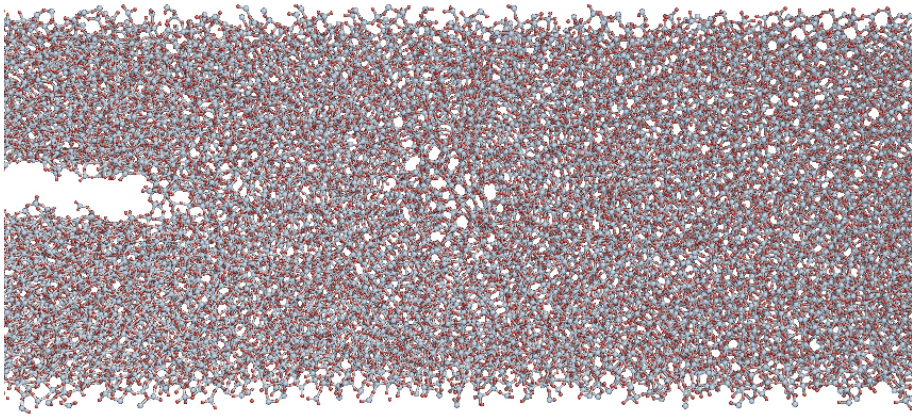

(b) $t = 50$ ps; $G = 10.57$ J/m^2

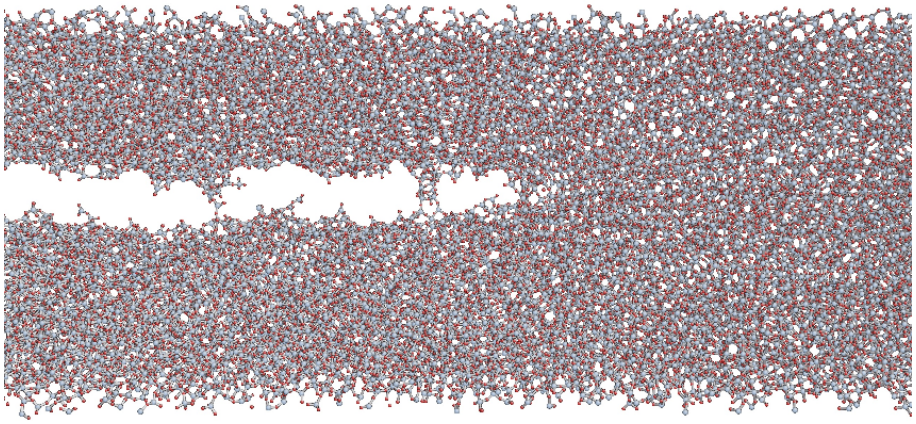

(c) $t = 70$ ps; $G = 12.57$ J/m^2

Figure 5.3: Classical MD snapshots of catastrophic fracture in amorphous silica at room temperature.

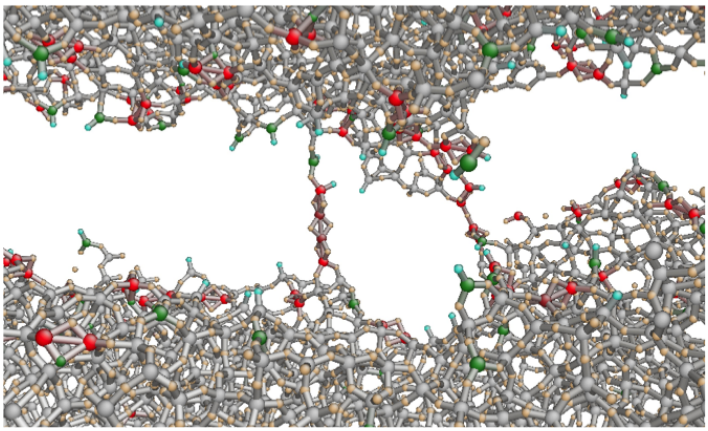

Figure 5.4: Formation of two-membered ring chains between the silica surfaces opened by the crack. Colouring denotes atomic coordination, with red Si atoms being over-coordinated and green Si atoms being under-coordinated.

central atoms. Again, this implied making sure that all Si atoms were terminated with their oxygens, in order to allow the cluster to be chemically passivated.

When the overall QM cluster (which contains the effective quantum atoms and the buffer atoms) is chosen, we need to terminate it in a suitable way. Different mechanisms have been proposed in the literature. In particular, we considered in our simulations:

1. Hydrogen termination: all the O atoms are terminated with an H atom, in order to create a O-H bond.

2. Oxygen termination: all the Si atoms are terminated with their oxygens, and all the O atoms are terminated with an extra electron to passivate them. This requires the core charge on the oxygen ions to be increased to ensure overall neutrality. This approach is a generalisation of the one proposed in Ref. [113].

Several convergence tests have been performed in order to select the termination mechanism that is best for our particular system, and to identify the calculation parameters to be used. Indeed, particular attention has to be paid to the following key parameters, whose values have to be carefully chosen to obtain convergent and reliable results:

- The convergence threshold for the SCF loop, which was set equal to 10^{-6} Ha[1];
- The electronic smearing temperature, set to $T = 5000$ K;

[1]The Hartree (Ha) is an atomic unit of energy - 1 Ha $\sim$ 27.2 eV

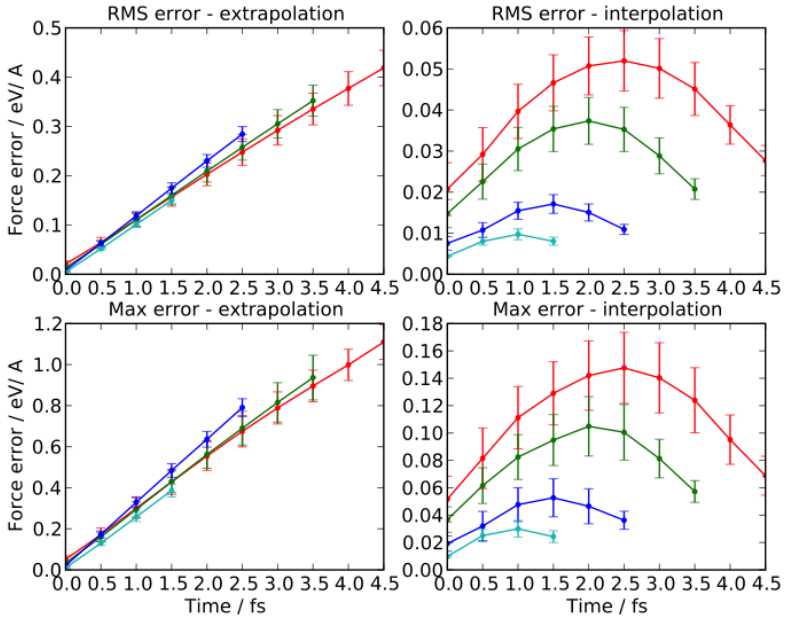

Figure 5.5: Force errors during LOTF predictor-corrector dynamics for different numbers of extrapolation steps. Red, green, blue and cyan lines correspond to 10, 8, 6 and 4 extrapolation steps, respectively.

- The number of unoccupied molecular orbitals which was increased with respect to the default value of CP2K (this value increases with the size of the system).

Further key parameters are the number and length of the springs used by the LOTF adjustable potential to fit the QM forces, and the number of extrapolation steps (see Sec. 2.5.3). The larger the number of extrapolation steps, the faster the calculation will be since a lower frequency of QM calculations is required. Tests have been performed on a minimal hybrid region of a single tetrahedral SiO_2 unit. In Fig. 5.5 we reproduce the force errors during LOTF predictor corrector dynamics for differing numbers of extrapolation steps.

We have further investigated the error associated with the number of springs used for the adjustable potential. This parameter is measured in terms of the maximum number of bond hops between pairs of atoms for them to be joined by an adjustable spring potential term. Increasing this value increases the number of the parameterised spring terms used by the LOTF scheme to fit the QM forces, and therefore increases the accuracy of the fit, but, as with any fitting procedure using too many degrees of freedom implies the risk of over-fitting with consequent loss of transferability. The minimum

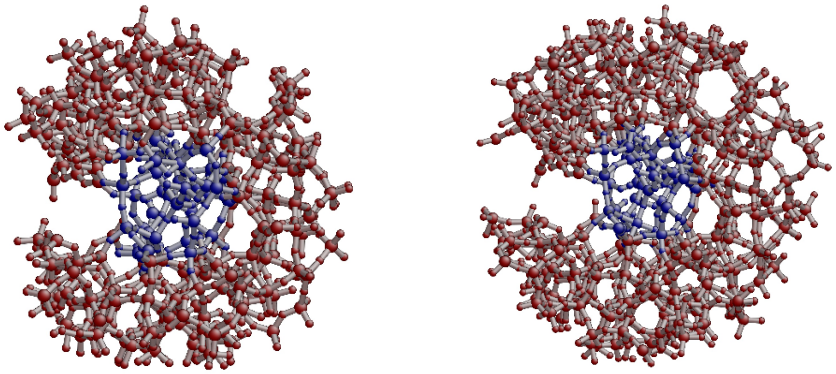

(a) (b)

Figure 5.6: Quantum silica clusters selected for LOTF simulation: (a) 152 QM atoms; (b) 250 QM atoms

number of possible hops for a reasonably accurate fit is five, which significantly improves the performance with respect to using just three hops (the default for dense covalent materials such as Si), with a very satisfactory maximum force error of 0.05 eV/Å during the interpolation.

5.4 Discussion and analysis

A main issue in LOTF calculations is the high computational cost arising from the very large size of the clusters under consideration, resulting from the large buffer radius (8 – 10 Å) needed to give converged forces, and the $O(N^3)$ scaling of the key QM algorithms. For this reason great efforts have been made to carefully choose quantum regions as small as possible to minimise the computational demand. We found the CP2K package to be highly memory intensive; this was the main computational bottleneck of our calculations.

The smallest QM region we were able to build in our amorphous silica structure contained 152 atoms. This size is just sufficient to represent a crack front traversing an amorphous SiO_2 bond network, whilst still enforcing periodic boundary conditions. Two main LOTF simulations have been performed using this active region, with two different sizes of the buffer region discussed above.

The computational cost of a single QM calculation on the larger buffer (Fig. 5.6b) is around 460 CPU hours, while the same operation for buffer (Fig. 5.6a) requires 140 CPU hours. Using the LOTF method with 8 extrapolation steps gives an overall cost

of 57.5 and 17.5 CPU hours per time step, respectively. Using the smaller buffer size, the first bond breaking event occurs after 0.1 ps of LOTF molecular dynamics.

We note that following the entire dynamics of a crack in amorphous silica using quantum calculations can only be achieved on very large-scale HPC platforms. On the contrary, the LOTF scheme could be used to check the forces on specific snapshots generated through classical MD simulations of fracture processes carried out by reliable QM-derived force fields (this option would not be available for purely covalent systems where suitable classical potentials do not exist). Moreover, our hybrid scheme appears ideal to investigate targeted properties of structures like the 2-membered rings chains outlined in Sec. 5.3.2, or modelling chemical reactions at the crack tip with Na+ ions or H_2O on the same fashion outlined in Chapter 3.

5.5 Summary

A preliminary molecular dynamics investigation on the fracture problem in amorphous silica structures has been presented. A technique to reproduce amorphous silica structures has been tested using a classical approach; calculations of stress strain curves have shown a fair agreement with previous literature studies. To this extent, interesting features like the formation of 2M ring chains have been detected.

The main difficulty has been experienced in efficiently applying a hybrid technique, as it has been done successfully in silicon. In fact, it has been shown that the computational cost necessary to achieve significant results of catastrophic fracture propagation comparable with experiments was beyond our current computational capacity. Higher computational resources are necessary to attack the fracture problem in amorphous silica, where larger system sizes are necessary because of the intrinsic lack of long range order typical of crystalline forms. Future challenges opened by this work will be outlined in Chapter 6.

Chapter 6

Future work

6.1 Fracture in glassy interfaces

Efficiency and durability of multi-layered materials depend on the properties of interfaces between different glassy phases. In Chapter 5 we only started a journey towards the challenge of studying fracture mechanisms in glassy interfaces. One of the main issue that we encountered behind modelling such a system is definitely the size, which is a consequence of the amorphous nature of glass. The absence of a long range order, commonly found in crystals, requires sampling amorphous structures in large three-dimensional samples.

6.1.1 Titanium dioxide

Titanium dioxide is encountered in nature in three main crystalline forms known as rutile, anatase and brookite. Rutile is the most stable phase at all temperatures, while the metastable phases anatase and brookite turn out in rutile upon heating.

In particular, titania anatase is an excellent photocatalyst material for environmental purification. Its scientific and industrial applications are numerous, ranging from white pigments, sunscreen and UV absorber, as a photocatalyst under ultraviolet light and in glass coatings with self cleaning and anti fogging properties. It also presents a super-hydrophilic phenomenon which led industries to superpose thin films of titania on amorphous silica, making a new high-tech self cleaning glass.

The photocatalytic property, discovered by Fujishima in 1967, is particularly important in energetic applications: under UV light TiO_2 (especially titania anatase) undergoes electrochemical photolysis if connected to an electrochemical cell containing water. [114] The super-hydrophilicity of TiO_2 coated glass was then discovered in 1995

again by Fujishima. [115] When TiO_2 is irradiated by UV light, water molecules adhere perfectly to the surface by reducing to zero its contact angle.

The photocatalytic and super-hydrophilic properties combined together make titanium dioxide the main ingredient to build self cleaning devices. In recent years thin films of titania have been extensively used as coating for glass; interfacing amorphous silica structures with titania generates a new product with self-cleaning properties. Moreover, the photocatalytic effect, active when the material is exposed to light, is responsible for chemical reactions which eventually oxidise any biological films present on the surface of the exposed glass. Despite their very recent discovery, self cleaning glasses are nowadays in mass production by several glass companies, with application to solar panels and architectural covering of buildings.

6.1.2 Preliminary results on titania anatase

We present preliminary molecular dynamics simulations of fracture propagation in titania (anatase) structures. To model the interatomic interaction between atoms we chose a modified version [109] of the Tangney-Scandolo (TS) potential [116], parameterised using density functional theory on rutile structures.

The TS pair potential has the Morse-stretch form:

$$U_{ij} = \frac{q_i q_j}{r_{ij}} + D_{ij}[e^{\gamma_{ij}[1-(r_{ij}/r^0_{ij})]} - 2e^{(\gamma_{ij}/2)[1-(r_{ij}/r^0_{ij})]}] \tag{6.1}$$

where U_{ij} is the energy of interactions between ions i and j and $r_{ij} = |r_i - r_j|$ is the distance between them. The charge of ion i is q_i, while parameters specific to the pair of species are D_{ij}, γ_{ij} and r^0_{ij}. The exponential part of the potential is truncated at a radius of 18.0 $a.u$. Regarding the dipole polarisation of ions, the induction of dipole moments includes the local electrostatic field and the short range repulsive forces between ions.

The preliminary results presented here constitute the first application of the titania TS potential to fracture simulation. Prior to running any fracture simulations, a seed crack on the (001) cleavage plane with the crack front along the [010] direction was built and relaxed in the anatase structure. Trying to build a single ended crack creates the technical difficulty of chemically terminating the yz surfaces perpendicular to the x crack propagation direction, without which polarisation instabilities could occur during the simulations. This problem was avoided by considering a double-ended crack with periodic boundary conditions along the x and z directions.

Figure 6.1 reports the time evolution of full classical MD simulations on a double ended crack in titania anatase. To initiate the fracture, a tensile loading was applied

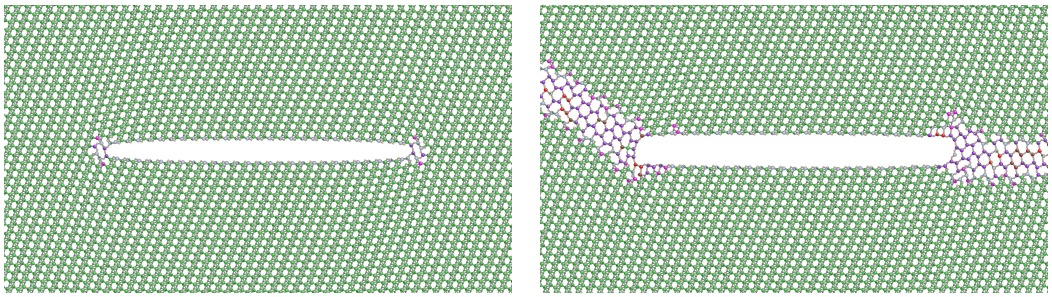

(a) $t = 0$ *ps*; $G = 4$ J/m^2. (b) $t = 20$ *ps*; $G = 9.7$ J/m^2.

Figure 6.1: Series of two snapshots from 20 *ps* of molecular dynamics on TiO_2 anatase crack. Increasing smoothly the loading the crack tip plastically deforms (b).

to the top and bottom surfaces with a constant rate of 5×10^{-4} J/m^2 fs (on the same fashion illustrated in Sec. 2.6.2 for a edge crack). Whenever a bond breaking was detected, the loading was kept constant, allowing the system to release the concentration of stress at the tip. If no bond breaking was detected within 500 fs, the loading was increased at the same rate.

The feature highlighted by this test is that the crack tip does not release elastic energy by breaking bonds along a cleavage plane, but instead by lengthening bonds and deforming their alignment relative to the surrounding region. Whilst the model does not reproduce brittle fracture behaviour in this cleavage plane, the deformed region develops following a straight path similar to that typically observed upon crack propagation in brittle materials. This result should be further investigated (e.g., by decreasing the loading rate), since there is no evidence of this kind of behaviour in anatase structures in the literature. The use of the full LOTF scheme for crystalline anatase can be taken into consideration only if the methods outlined above prove unable to accurately describe the brittle behaviour of titanium dioxide.

6.1.3 Testing SiO_2/TiO_2

Interest in advancing research on self-cleaning glass at the atomic scale is mainly due to the complicated mechanical adhesion of titania thin films on glass. In fact, the interface of two materials that do not adhere perfectly creates a potential threat to its durability. Defects and voids at the interface represent potential seed cracks that, under loading, might unexpectedly fail.

A preliminary investigation of the a-SiO_2/TiO_2 interface has been started by collaborators of the ADGLASS consortium. [117] To this purpose, a model of a sharp

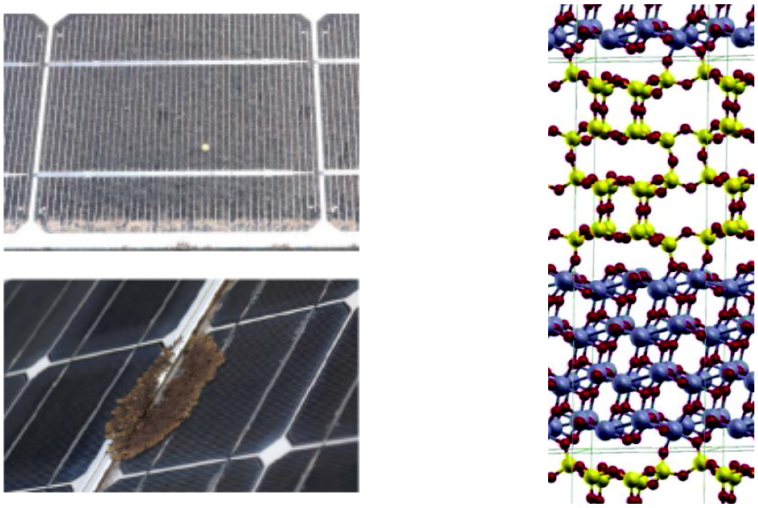

(a) (b)

Figure 6.2: Self-cleaning property application to photovoltaic cells. (a) Typical problem of photovoltaic cells (picture above): long-time exposure to outdoor environments leads to the formation of opaque film and growth of moss (picture below) [118]. (b) Proposed atomistic model of self-cleaning glass a $-$ SiO_2 $-$ TiO_2 interface; atoms are coloured by species: yellow for silicon, grey for titanium, red for oxygen. [117]

interface between TiO_2(101) anatase and a-SiO_2 has been constructed and reported in Fig. 6.2b. Notice that, away from the interface layer, the perfect atomistic structure of the two compounds is preserved. The geometrical structure of the interface has been investigated with full QM precision level by ab-initio DFT calculations, finding a strong connection between the bonding topology and the electron density of states.

A current issue under investigation is preparing a crack model of the interface system. In fact, the bonding topology at the interface is hardly reproducible by classical interatomic potentials. For this reason, the LOTF approach represents a promising strategy to study the complicated interface at a more reasonable computational cost compared to other hybrid techniques. Performing multi-scale simulations of fracture at the interface of SiO_2/TiO_2 is one of the milestones of the "Fracture Team" at Kings College London.

6.2 Stress corrosion cracking

Fracture of silicates is relevant in many other sectors of human life, spanning from mining, where a huge amount of energy is required to fragment rocks into fine powder,

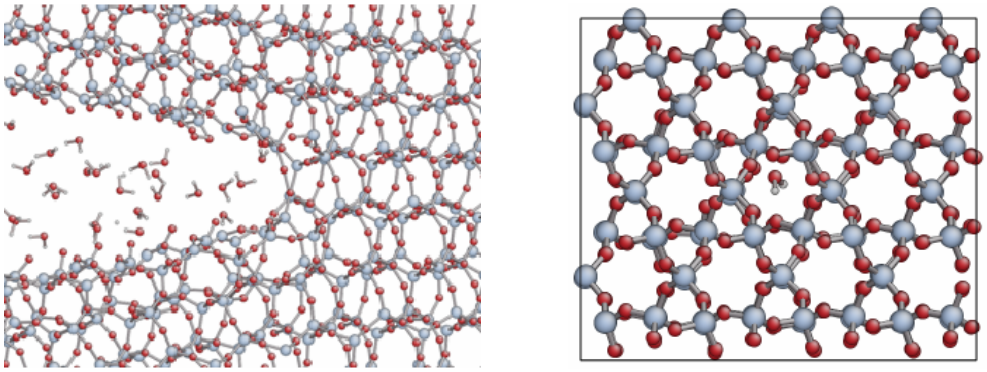

(a) (b)

Figure 6.3: Stress corrosion cracking in silica. (a) Subcritical stress corrosion cracking induced by water in silica and silicon; (b) Role of deep water penetration in silica fracture. [119]

to medicine, where biomedical implants introduced into the human body are often made of silica, titania and zirconia for their high compatibility. A vein of future research is to perform QM-accurate simulations to clarify the role played by the oxygen and water in initiating stress corrosion cracking (SCC) in silica and silicon. [119]

This task can be decomposed into three major goals:

1. SCC in wet silicon;
2. SCC in wet silica;
3. Role of deep water in penetration.

Firstly, motivated by the analysis of SCC of silicon via oxygen dissociation presented in Chapter 3, we aim to complete the picture of a realistic experimental setting by clarifying the role of water towards an enhancement, or a passivation, of the observed subcritical crack growth in silicon. Ideally, since humidity and air are both present at room conditions, the simultaneous attack of water and oxygen at the crack tip must be taken into consideration.

Secondly, after determining the crack initiation conditions, a hybrid simulation of SCC in silica via water could be carried out. This will offer the possibility to quantitatively compare experimental measures of reaction barriers of the hydrolysis process with simulation predictions.

In addition to the above, SCC may be enhanced by the diffusion of water ahead of a crack within the strained silica matrix. [83]. This is particularly important in amorphous silica, where small pre-existing voids can act as seed sites for cavity formation.

Chapter 7

Conclusions

In this thesis, I focused on two archetypical systems of brittle fracture: silicon and amorphous silica. The fracture problem has been analysed in a wide range of velocities, from those typical of subcritical crack growth induced by stress corrosion mechanisms to those associated with the catastrophic brittle fracture behaviour. By means of hybrid quantum mechanical and classical molecular dynamics simulations, I could reach the following main conclusions:

- stress corrosion cracking in silicon takes place via oxygen dissociation and consequent adsorption at the crack tip;
- cracks in silicon undergo a transition from catastrophic-mode to activated-mode crack speeds as a function of temperature and loading;
- catastrophic fracture in amorphous silica occurs via nucleation, growth and coalescence of flaws intrinsically present in its structure.

My hybrid simulations reveal that oxygen plays the role of a corrosive agent in silicon fracture, consistent with recent experimental measurements of fracture initiation energy. Chemical reactions occurring in proximity of the crack tip induce immediate dissociation of the first oxygen molecule, followed by the attack of single oxygen atoms to the silicon sites at the tip. This computational prediction is in excellent agreement with recent experimental observations of subcritical crack growth in air: an important consequence is the possibility to control the fracture process via the oxygen supply at the crack tip. Interestingly the combined attack by oxygen and water would be a natural extension of my research, which would have to involve lower loads and speeds (see Fig. 3.1a), where humidity must be taken into account. Moreover, modelling analogous processes in silicon dioxide would be extremely useful and relevant in both

the amorphous and crystalline forms, e.g., in view of the strategic importance for energy saving of fine-tuning the environmental parameters during rock crushing and grinding in mineral ores processing.

In my crack velocity investigation I observe a catastrophic-to-activated transition of crack propagation in silicon at energy release rates of around 3 J/m^2, remarkably with "cold" cracks travelling faster than "hot" ones at higher loadings. This computational prediction, achieved via a hybrid approach involving two classical force fields yields insight potentially useful for a better understanding of the dynamics of the crack as a function of temperature. An interesting, but so far prohibitively cpu-intensive computational test of these theoretical finding could be achieved by carrying out new simulations free of the constraint of periodic boundary conditions along the crack front direction.

Extended crack front sections could be investigated in this work in a series of (non hybrid) classical molecular dynamics simulations which allowed me to reproduce typical fracture features of crack propagation in amorphous silica e.g., the formation of two-membered ring chains, confirming the results of previous studies. As a result, fracture in amorphous silica appears to originate by the nucleation, growth and coalescence of nano-voids intrinsic to its structure.

In conclusion, I applied hybrid quantum mechanical and classical molecular dynamics simulations to two prototypical brittle model materials: silicon and amorphous silica. Among all the results of this research, perhaps the most significant one is that for the first time we have computational evidence, at the quantum accuracy level, of the occurrence of stress corrosion cracking promoted by oxygen dissociation and adsorption at the silicon crack tip; this result is in excellent agreement with novel experimental observations carried out in a collaborating experimental group in parallel with the present study.

References

[1] F. Erdogan. Fracture Mechanics. *International Journal of Solids and Structures*, 37(171), 2000. 17

[2] E. R. Parker. *Brittle behavoiur of engineering structures*. Wiley, New York, 1957. 18

[3] B. Lawn. *Fracture of Brittle Solids*. Cambridge University Press, 1993. 18, 31, 33, 34, 70, 85, 97

[4] L. B. Freund. *Dynamic Fracture Mechanics*. Cambridge University Press, 1990. 18, 34, 35, 85, 87

[5] S. Giordano, A. Mattoni, and L. Colombo. Brittle Fracture: From Elasticity Theory to Atomistic Simulations. *Reviews in Computational Chemistry*, 27(1), 2010. 19, 25, 28, 30, 32, 33

[6] L. Colombo and S. Giordano. *Introduzione alla teoria dell'elasticitá - Meccanica dei solidi continui in regime elastico*. Springer, 2007. 21, 22, 24, 25

[7] C. E. Inglis. Stresses in a plate due to the presence of cracks and sharp corners. *Trans. Inst. Nav. Arch.*, 1913. 27

[8] A.A. Griffith. The phenomena of rupture and flow in solids. *Philos. Trans. R. Soc. London A*, 221(163), 1921. 28, 29, 31, 86

[9] G. R. Irwin. *Fracture Dynamics - Fracturing of Metals*. American Society for Metals, Cleveland, 1948. 31

[10] N. F. Mott. Brittle fracture in mild steel plates. *Engineering*, 165(16), 1998. 34

[11] M. Marder. New dynamical equation for cracks. *Phys. Rev. Lett.*, 66(2484), 1991. 35

[12] A. Kobayashi, N. Ohtani, and T. Sato. Phenomenological aspects of viscoelastic crack propagation. *Journal of Applied Polymer Science*, 18(1625), 1974. 35, 37

[13] J. Fineberg, S. P. Gross, M. Marder, and H. L. Swinney. Instability in dynamic fracture. *Phys. Rev. Lett.*, 67(457), 1991. 35, 37, 85, 87

[14] J. Fineberg, S. P. Gross, M. Marder, and H. L. Swinney. Instability in the propagation of fast cracks. *Phys. Rev. B*, 45(5146), 1992. 35

[15] J. Fineberg and M. Marder. Instability in dynamic fracture. *Phys. Rep.*, 313(1), 1999. 35, 36, 87

[16] J. A. Hauch, D. Holland, M. P. Marder, and H. L. Swinney. Dynamic fracture in single crystal silicon. *Phys. Rev. Lett.*, 82(3283), 1999. 35, 60, 61, 62, 87

[17] R. Thomson, C. Hsieh, and V. Rana. Lattice Trapping of Fracture Cracks. *Journal of Applied Physics*, 42(3154), 1971. ISSN 0021-8979. 37, 72, 86

[18] L. I. Slepyan. Dynamics of a crack in a lattice. *Sov. Phys. Dokl*, 26(538), 1981. 37

[19] M. Marder and Xiangming Liu. Instability in lattice fracture. *Phys. Rev. Lett.*, 71(2417), 1993. 37, 87

[20] D. Frenkel and B. Smit. *Understanding Molecular Simulation*. Academic Press, 2002. 40

[21] L. Verlet. Computer "Experiments" on Classical Fluids. I. Thermodynamical Properties of Lennard-Jones Molecules. *Phys. Rev.*, 159(98), 1967. 40

[22] W.C. Swope, H.C. Andersen, P.H. Berens, and K.R. Wilson. A computer simulation method for the calculation of equilibrium constants for the formation of physical clusters of molecules: Application to small water clusters. *J. Chem. Phys.*, 76(637), 1982. 40

[23] H.C. Andersen. Molecular dynamics simulation at constant pressure and/or temperature. *J. Chem. Phys.*, 72(2384), 1980. 40

[24] S. A. Adelman and J. D. Doll. Generalized Langevin equation approach for atom/solid-surface scattering: General formulation for classical scattering of harmonic solids. *J. Chem. Phys.*, 64(2375), 1976. 40, 58

[25] F. H. Stillinger and T. A. Weber. Computer simulation of local order in condensed phases of silicon. *Phys. Rev. B*, 31(5262), 1985. 42, 44, 88

[26] D. Holland and M. Marder. Cracks and Atoms. *Advanced Materials*, 11(793), 1999. 43, 85

[27] A. Mattoni, M. Ippolito, and L. Colombo. Atomistic modeling of brittleness in covalent materials. *Phys. Rev. B*, 76(224103), 2007. 44

[28] M. Born and R. Oppenheimer. Zur quantentheorie der molekeln. *Ann. Phys.*, 389(457), 1927. 44

[29] R. Car and M. Parrinello. Unified Approach for Molecular Dynamics and Density-Functional Theory. *Phys. Rev. Lett.*, 55(2471), 1985. 45

[30] P. Hohenberg and W. Kohn. Inhomogeneous electron gas. *Phys. Rev.*, 136(B864), 1964. 46

[31] W. Kohn and L. J. Sham. Self-Consistent Equations Including Exchange and Correlation Effects. *Phys. Rev.*, 140(A1133), 1965. 46

[32] N. Troullier and José Luriaas Martins. Efficient pseudopotentials for plane-wave calculations. *Phys. Rev. B*, 43(1993), 1991. 47

[33] D. Vanderbilt. Soft self-consistent pseudopotentials in a generalized eigenvalue formalism. *Phys. Rev. B*, 41(7892), 1990. 47

[34] R. P. Feynman. Forces in molecules. *Phys. Rev.*, 56(340), 1939. 48

[35] A. Warshel and M. Levitt. Theoretical studies of enzymic reactions: Dielectric, electrostatic and steric stabilization of the carbonium ion in the reaction of lysozyme. *Journal of Molecular Biology*, 103(227), 1976. 50

[36] J. C. H. Spence, Y. M. Huang, and O. Sankey. Lattice trapping and surface reconstruction for silicon cleavage on (111). Ab-initio quantum molecular dynamics calculations. *Acta Metallurgica et Materialia*, 41(2815), 1993. 50

[37] S. Ogata, F. Shimojo, R. K. Kalia, A. Nakano, and P. Vashishta. Environmental effects of H_2O on fracture initiation in silicon: A hybrid electronic-density-functional/molecular-dynamics study. *Journal of Applied Physics*, 95 (5316), 2004. 50, 69

[38] R. Bernstein, J. R. Kermode, and G. Csányi. Hybrid atomistic simulation methods for material systems. *Rep. Prog. Phys.*, 72(026591), 2009. 50, 57, 59, 90

[39] A. De Vita and R. Car. A novel scheme for accurate MD simulations of large systems. *Mater. Res. Soc. Symp. Proc.*, 491(473), 1998. 50

[40] G. Csányi, T. Albaret, M. C. Payne, and A. De Vita. "Learn on the Fly": A Hybrid Classical and Quantum-Mechanical Molecular Dynamics Simulation. *Phys. Rev. Lett.*, 93(175503), 2004. 50

[41] G. Csányi, S. Winfield, J. R. Kermode, A. Comisso, A. De Vita, N. Bernstein, and M. Payne. LIBATOMS/QUIP - A molecular dynamics software for multi-scale modelling, 2013. URL http://www.libatoms.org. 50

[42] J. R. Kermode. *Multiscale Hybrid Simulation of Brittle Fracture*. PhD thesis, Pembroke College, University of Cambridge, 2008. 50, 52, 58, 64, 86

[43] G. Moras, R. Choudhury, J. R. Kermode, G. Csányi, M. C. Payne, and A. De Vita. Hybrid Quantum/Classical Modeling of Material Systems: the "Learn On The Fly" Molecular Dynamics Scheme. *Trends in Computational Nanomechanics*, 9 (1), 2010. 50, 65

[44] J. R. Kermode. quippy - Python interface to the LIBATOMS/QUIP molecular dynamics framework, 2013. URL http://www.jrkermode.co.uk/quippy. 50

[45] N. Bernstein. Linear scaling nonorthogonal tight-binding molecular dynamics for nonperiodic systems. *EPL (Europhysics Letters)*, 55(52), 2001. 52, 53

[46] N. Bernstein and D. W. Hess. Lattice Trapping Barriers to Brittle Fracture. *Phys. Rev. Lett.*, 91(025501), 2003. 52, 85, 87

[47] J.R. Kermode, G. Peralta, Z. Li, and A. De Vita. Multiscale modelling of materials chemomechanics: brittle fracture of oxides and semiconductors. *Proc. Mat. Sc.*, 271(1681), 2014. 59

[48] G. Moras, L. C. Ciacchi, C. Elsässer, P. Gumbsch, and A. De Vita. Atomically Smooth Stress-Corrosion Cleavage of a Hydrogen-Implanted Crystal. *Phys. Rev. Lett.*, 105(075502), 2010. 59, 69

[49] J. R. Kermode, L. Ben-Bashat, F. Atrash, J.J. Cilliers, D. Sherman, and A. De Vita. Macroscopic scattering of cracks initiated at single impurity atoms. *Nat. Commun.*, 4(2441), 2013. 59, 86

[50] R. Choudhury, C. Gattinoni, and A. Makov, G.and De Vita. Molecular dynamics studies of the dissociated screw dislocation in silicon. *J Phys Condens Matter.*, 22(074210), 2010. 59

[51] J. R. Kermode, T. Albaret, D. Sherman, N. Bernstein, P. Gumbsch, M. C. Payne, G. Csányi, and A. De Vita. Low-speed fracture instabilities in a brittle crystal. *Nature*, 455(1224), 2008. 59, 63, 71, 72, 86, 90

[52] D. Fernandez-Torre, T. Albaret, and A. De Vita. Role of surface reconstructions in (111) silicon fracture. *Phys. Rev. Lett.*, 105(185502), 2010. 59

[53] J. A. Hauch and M. P. Marder. Energy balance in dynamic fracture, investigated by a potential drop technique. *Int. Journ. Frac.*, 90(133), 1998. 62

[54] B. Stalder, P. Béguelin, and H. H. Kausch. A simple velocity gauge for measuring crack growth. *Int. Journ. Frac.*, 22(47), 1983. 62

[55] E. Bitzek, P. Koskinen, F. Gahler, M. Moseler, and P. Gumbsch. Structural relaxation made simple. *Phys. Rev. Lett.*, 97(170201), 2006. 64, 72

[56] M. Ciccotti. Stress-corrosion mechanisms in silicate glasses. *J. Phys. D: Appl. Phys.*, 42(214006), 2009. 67, 106

[57] E. Orowan. The fatigue of glass under stress. *Nature*, 50(407), 1967. 67

[58] S. M. Wiederhorn. Influence of water vapor on crack propagation in soda-lime glass. *Journal of the American Ceramic Society*, 50(407), 1967. 67

[59] S Wiederhorn and L. H. Bolz. Stress Corrosion and Static Fatigue of Glass. *Journal of the American Ceramic Society*, 53(543), 1970. 67

[60] T. A. Michalske and S. W. Freiman. A molecular interpretation of stress corrosion in silica. *Nature*, 295(511), 1982. 68

[61] R. F. Cook. Strength and sharp contact fracture of silicon. *Journal of Materials Science*, 41(841), 2006. 69

[62] J. A. Connally and S. B. Brown. Slow Crack Growth in Single-Crystal Silicon. *Science*, 256(1537), 1992. 69

[63] J. Zhang, C.-Z Wang, and K.-M. Ho. Finding the low-energy structures of Si[001] symmetric tilted grain boundaries with a genetic algorithm. *Phys. Rev. B*, 80 (174102), 2009. 69

[64] R. J. Jaccodine. Surface Energy of Germanium and Silicon. *Journal of The Electrochemical Society*, 110(524), 1963. 69

[65] S. Bhaduri and F. Y. Wang. Fracture surface energy determination in 1 1 0 planes in silicon by the double torsion method. *Journal of Materials Science*, 21(2489), 1986. 69

[66] G. Michot. *Crystal Properties and Preparation*, volume 17. Trans Tech, Switzerland, 1988. 69

[67] F. Ebrahimi and L. Kalwani. Fracture anisotropy in silicon single crystal. *Materials Science and Engineering: A*, 268(116), 1999. 69

[68] C. Chen and M. Leipold. Fracture toughness of silicon. *Am. Ceram. Soc. Bull.*, 59(469), 1980. 69

[69] C. Messmer and J. C. Bilello. The surface energy of Si, GaAs, and GaP. *Journ. Appl. Phys.*, 52(4263), 1981. 69

[70] D. J. Eaglesham, A. E. White, L. C. Feldman, N. Moriya, and D. C. Jacobson. Equilibrium shape of si. *Phys. Rev. Lett.*, 70(1643), 1993. 69

[71] J. J. Gilman. Direct measurements of the surface energies of crystals. *J. Appl. Phys.*, 31(2208), 1960. 69, 90

[72] R. Pérez and P. Gumbsch. Directional Anisotropy in the Cleavage Fracture of Silicon. *Phys. Rev. Lett.*, 84(5347), 2000. 70, 71, 81

[73] A. A. Stekolnikov, J. Furthmüller, and F. Bechstedt. Absolute surface energies of group-iv semiconductors: Dependence on orientation and reconstruction. *Phys. Rev. B*, 65(115318), 2002. 70

[74] G-H Lu, M. Huang, M. Cuma, and F. Liu. Relative stability of si surfaces: A first-principles study. *Surface Science*, 588(61), 2005. 70

[75] J. G. Swadener, M. I. Baskes, and M. Nastasi. Molecular Dynamics Simulation of Brittle Fracture in Silicon. *Phys. Rev. Lett.*, 89(085503), 2002. 71

[76] A. Gleizer, G. Peralta, J. R. Kermode, A. De Vita, and D. Sherman. Dissociative chemisorption of O_2 inducing stress corrosion cracking in silicon crystals. Submitted to Phys. Rev. Lett., 2013. 71, 73, 75, 77, 79, 80

[77] J. P. Perdew, K. Burke, and M. Ernzerhof. Generalized gradient approximation made simple. *Phys. Rev. Lett.*, 77(3865), 1996. 72

[78] G. Kresse and D. Joubert. From ultrasoft pseudopotentials to the projector augmented-wave method. *Phys. Rev. B*, 59(1758), 1999. 72

[79] S. J. Clark, M. D. Segall, C. J. Pickard, P. J. Hasnip, M. J. Probert, K. Refson, and M. C. Payne. First principles methods using castep. *Zeitschrift fur Kristallographie*, 220(567), 2005. 72

[80] K. Kato and T. Uda. Chemisorption of a single oxygen molecule on the Si(100) surface: Initial oxidation mechanisms. *Phys. Rev. B*, 62(15978), 2000. 72

[81] U. Höfer, P. Morgen, W. Wurth, and E. Umbach. Initial stages of oxygen adsorption on Si(111). II. The molecular precursor. *Phys. Rev. B*, 40(1130), 1989. 72

[82] K. C. Pandey. New π-bonded chain model for si(111)-(21) surface. *Phys. Rev. Lett.*, 47(1913), 1981. 74

[83] S. M. Wiederhorn, T. Fett, J. P. Guin, and M. Ciccotti. Griffith cracks at the nanoscale. *International Journal of Applied Glass Science*, 4(76), 2013. 82, 123

[84] A. Grimaldi, M. George, G. Pallares, C. Marlière, and M. Ciccotti. The crack tip: A nanolab for studying confined liquids. *Phys. Rev. Lett.*, 100(165505), 2008. 82

[85] L. Colombi Ciacchi, D. J. Cole, M. C. Payne, and P. Gumbsch. Stress-driven oxidation chemistry of wet silicon surfaces. *Journ. Phys. Chem. C*, 112(12077), 2008. 82

[86] B. R. Lawn. Diffusion-controlled subcritical crack growth. *Materials Science and Engineering*, 13(277), 1974. 83, 84

[87] D. Holland and M. Marder. Ideal Brittle Fracture of Silicon Studied with Molecular Dynamics. *Phys. Rev. Lett.*, 80(746), 1998. 85

[88] M. J. Buehler, A. C. T. van Duin, and W. A. Goddard. Multiparadigm Modeling of Dynamical Crack Propagation in Silicon Using a Reactive Force Field. *Phys. Rev. Lett.*, 96(095505), 2006. 86

[89] D. Sen, C. Thaulow, S. V. Schieffer, A. Cohen, and M. J. Buehler. Atomistic Study of Crack-Tip Cleavage to Dislocation Emission Transition in Silicon Single Crystals. *Phys. Rev. Lett.*, 104(235502), 2010. 86

[90] M. Marder. Effects of atoms on brittle fracture. *International Journal of Fracture*, 130(517), 2004. 87

[91] F. Atrash, A. Hashibon, P. Gumbsch, and D. Sherman. Phonon emission induced dynamic fracture phenomena. *Phys. Rev. Lett.*, 106(085502), 2011. 87

[92] M. Marder and S. Gross. Origin of crack tip instabilities. *J. Mech. Phys. Solids*, 43(1), 1995. 87

[93] I. Beery, U. Lev, and D. Sherman. On the lower limiting velocity of a dynamic crack in brittle solids. *Journal of Applied Physics*, 93(2429), 2003. 87

[94] A. P. Bartók, M. C. Payne, R. Kondor, and G. Csányi. Gaussian Approximation Potentials: The Accuracy of Quantum Mechanics, without the Electrons. *Phys. Rev. Lett.*, 104(136403), 2010. 88

[95] S. A. Dianat and R. M. Rao. Fast algorithms for phase and magnitude reconstruction from bispectra. *Opt. Eng.*, 29(504), 1990. 89

[96] A. Bartók-Pártay. *Gaussian Approximation Potential: an interatomic potential derived from first principles Quantum Mechanics*. PhD thesis, Pembroke College, University of Cambridge, 2009. 89

[97] G. Peralta, J. R. Kermode, S. Cereda, Z. Li, A. P. Bartok, G. Csányi, and A. De Vita. Inversion in crack speed versus temperature during crossover from activated to catastrophic fracture. In preparation, Department of Physics, Kings College London, 2013. 91, 96, 98, 103, 104

[98] S. Ryu, C. R. Weinberger, M. I. Baskes, and W. Cai. Improved modified embedded-atom method potentials for gold and silicon. *Modelling Simul. Mater. Sci. Eng.*, 17(75008), 2009. 100

[99] M. Okaji. Absolute Thermal Expansion Measurements of Single-Crystal Silicon in the Range 300-1300 K with an Interferometric Dilatometer. *International Journal of Thermophysics*, 9(1101), 1988. 100

[100] Yasumasa Okada and Yozo Tokumaru. Precise determination of lattice parameter and thermal expansion coefficient of silicon between 300 and 1500 k. *Journal of Applied Physics*, 56(314-320), 1984. 100

[101] M. I. Ojovan. Glass formation in amorphous SiO_2 as a percolation phase transition in a system of network defects. *Journal of Experimental and Theoretical Physics Letters*, 79(632), 2004. 107

[102] M. I. Ojovan. Configurons: Thermodynamic Parameters and Symmetry Changes at Glass Transition. *Entropy*, 10(334), 2008. 107

[103] W. H. Zachariasen. The atomic arrangement in glass. *J. Am. Chem. Soc.*, 54 (3841), 1932. 108

[104] S. R. Elliott. Medium-range structural order in covalent amorphous solids. *Nature*, 354(445), 1991. 108

[105] R. M. Van Ginhoven, H. Jónsson, and L. R. Corrales. Silica glass structure generation for *ab initio* calculations using small samples of amorphous silica. *Phys. Rev. B*, 71(024208), 2005. 108, 113

[106] N. H. March and M. P. Tosi. *Coulomb Liquids*. Academic, New York, 1984. 109

[107] B. W. H. van Beest, G. J. Kramer, and R. A. van Santen. Force fields for silicas and aluminophosphates based on *ab initio* calculations. *Phys. Rev. Lett.*, 64 (1955–1958), 1990. 109

[108] P. Tangney and S. Scandolo. An ab initio parametrized interatomic force field for silica. *J. Chem. Phys.*, 117(8898), 2002. 109

[109] J. R. Kermode, S. Cereda, P. Tangney, and A. De Vita. A first principles based polarizable O(N) interatomic force field for bulk silica. *J. Chem. Phys.*, 133 (094102), 2010. 109, 120

[110] K. Muralidharan, K.-D. Oh, P. A. Deymier, K. Runge, and J. H. Simmons. Molecular dynamics simulations of atomic-level brittle fracture mechanism in amorphous silica. *J. Mater. Sci.*, 42(4159), 2007. 111, 113

[111] H. Edelsbrunner, D. G. Kirkpatrick, and R. Seidel. On the shape of a set of points in the plane. *IEEE transaction of information theory*, 29(551), 1983. 112

[112] D. Ceresoli, M. Bernasconi, S. Iarlori, M. Parrinello, and E. Tosatti. Two-Membered Silicon Rings on the Dehydroxylated Surface of Silica. *Phys. Rev. Lett.*, 84(3887), 2000. 113

[113] F. Zipoli, T. Laino, A. Laio, M. Bernasconi, and M. Parrinello. A QUICKSTEP-based quantum mechanics/molecular mechanics approach for silica. *J. Chem. Phys.*, 124(154707), 2006. 115

[114] A. Fujishima and K. Honda. Electrochemical photolysis of water at a semiconductor electrode. *Nature*, 238(37), 1972. 119

[115] R. Wang, K. Hashimoto, A. Fujishima, M. Chikuni, E. Kojima, A. Kitamura, and M. S. T. Watanabe. Light-induced amphiphilic surfaces. *Nature*, 388(431), 1997. 120

[116] X. J. Han, L. Bergqvist, P. H. Dederichs, H. Müller-Krumbhaar, J. K. Christie, S. Scandolo, and P. Tangney. Polarizable interatomic force field for TiO_2 parametrized using density functional theory. *Phys. Rev. B*, 81(134108), 2010. 120

[117] N. Seriani, C. Pinilla, S. Cereda, A. De Vita, and S. Scandolo. Titania-Silica Interfaces. *The Journal of Physical Chemistry C*, 116(11062), 2012. 121, 122

[118] ADGLASS Consortium. Adhesion and Cohesion at Interfaces in High Performance Glassy Systems. Grant Agreement for collaborative project EU-FP7-NMP 229205, 2009. 122

[119] J. R. Kermode, O. E. von Lilienfeld, and De Vita. SiO_2 Fracture: Chemomechanics with a Machine Learning Hybrid QM/MM Scheme. Research proposal. King's College London and University of Basel, 2014. 123